

THESIS TITLE

Pruthvi Mehta

2022

Contents

1	Introduction	v
1.1	Introduction	v
1.1.1	Neutrino Physics	v
1.1.2	History of Neutrino Physics	v
1.1.3	The Solar Neutrino Problem	vi
1.1.4	Neutrino Oscillation Theory	x
1.1.5	Neutrino-nucleus interactions in Super-Kamiokande Gd	xiii
1.1.6	Supernova Relic Neutrinos	xviii
2	The Tokai-to-Kamioka experiment	xxxii
2.1	The Tokai-to-Kamioka experiment	xxxii
2.1.1	Neutrino beam production	xxxii
2.1.2	Near detectors	xxxiv
3	The Super Kamiokande Detector	xlii
3.1	The Super-Kamiokande detector	xlii
3.1.1	Background and detector design	xlii
3.1.2	Data aquisition system	xlvi
3.2	Event Reconstruction	xlvii
3.2.1	Vertex Reconstruction	xlvii
3.2.2	Direction Reconstruction	1
3.2.3	Energy reconstruction	1
4	Super-Kamiokande Detector Calibration	liii
4.1	Inner detector calibration	liii

4.1.1	PMT High-voltage setting calibration	liii
4.1.2	Relative gain calibration	liv
4.1.3	Absolute gain calibration	lv
4.1.4	Relative quantum efficiency measurement	lvii
4.1.5	Timing information calibration	lix
4.1.6	Measurement of light reflection on the black sheet and the PMTs . .	lxii
5	The UK Light Injection System	lxix
5.1	The UK Light Injection System Electronics	lxix
5.1.1	UKLI System Optics	lxx
5.1.2	UKLI work towards Hyper-Kamiokande	xcviii
6	Super-Kamiokande Gadolinium Upgrade	cii
6.1	Physics motivation behind Super-Kamiokande Gadolinium Upgrade	cii
6.2	The EGADS project	civ
6.3	Gadolinium loading into Super-Kamiokande	cvii
7	Measurement of Neutral Current Quasielastic Interactions with Super-Kamiokande Gadolinium Upgrade	c xvii
7.1	Event Simulation	c xviii
7.1.1	Neutrino flux	c xviii
7.1.2	Primary interaction	c xix
7.1.3	Detector response and interactions in the detector medium	c xx
7.2	Event Reconstruction	c xxvi
7.2.1	Bonsai output reconstruction quantities	c xxvi
7.2.2	Comparison of BONSAI reconstruction output variables between SKDETSIM versions	c xxviii
7.2.3	NCQE event selection	c xxxii
7.2.4	Charged current event (CC) interaction cut	c xxxiii
7.2.5	Prompt event NCQE reduction cut plots	c xxxiv
7.2.6	Background injection	c xxxiv
7.3	NTag algorithm	c xxxviii
7.3.1	True neutron tagging information	c xxxviii
7.3.2	Primary selection criteria	c xlii
7.3.3	Secondary selection criteria	c xlv

8 Systematic and statistical uncertainty calculations	cxlvi
8.1 Systematic uncertainty calculation methodology	cxlvi
8.2 Neutrino beam flux uncertainty	cxlix
8.3 Neutrino cross section uncertainty	cli
8.4 Pion final state interaction (FSI) and secondary interaction (SI) uncertainties	cliii
8.5 Nucleon final state interactions	clv
8.6 Muon and pion capture on Oxygen-16	clvii
8.7 Nucleon SI	clviii
8.7.1 MICAP uncertainty calculation	clix
8.7.2 HETC uncertainty calculation	clix
9 Conclusion	clxi
A Appendix A	clxx

Chapter 1

Introduction

1.1 Introduction

1.1.1 Neutrino Physics

There are a plethora of physics phenomenon in which neutrinos are involved, including beta decay, fusion, and supernovae. As part of the Standard Model, they are described as being Dirac fermions with no electric charge with three flavours: the electron neutrino, the muon neutrino and the tau neutrino, corresponding with their associated leptons: the electron, muon and tauon. Prior to the discovery of neutrino oscillations, it was believed that neutrinos were massless, but they in fact have small but non zero masses ($\leq 1\text{eV}$) [7]. This chapter will discuss a brief history of neutrino physics including the discovery of neutrino oscillations, the manner in which neutrinos interact with nuclei in the Super-Kamiokande detector, and the motivation behind an NCQE neutron tagging analysis.

1.1.2 History of Neutrino Physics

To correct a violation of energy and momentum conservation discovered in beta-decay, Wolfgang Pauli put forward the idea of a neutrino as a solution [13]. He originally named this particle the “neutron”, prior to Chadwick’s discovery of the actual neutron two years later. Enrico Fermi then proposed to call it the neutrino, Italian for “little neutral one”. In 1934, Enrico Fermi’s theory of beta decay stated that a neutron could decay to a proton, electron and an antineutrino and in 1956 [29], Clyde Cowan and Frederick Reines directly confirmed the existence of neutrinos [16], by detecting the electron antineutrino

originating from inverse beta decay produced from nuclear reactor or fission products. In inverse beta decay an electron antineutrino interacts with a proton to produce a neutron and positrons.

These positrons pair-annihilate with electrons and produce two 0.5 MeV gamma rays and scintillator material was placed in a tank of water, which was used to detect the gamma photons, and the scintillator light produced flashes of visible light which were detected by photomultiplier tubes. Cadmium chloride was used to detect the coincident neutron, which after exciting and de-exciting, emits a gamma ray within 5 microseconds after the pair-annihilation gammas are detected. In 1962, Lederman, Schwartz and Steinberger detected the muon neutrino [17]. To discover the muon neutrino, the AGS (Alternating Gradient Synchrotron) at Brookhaven was used - the AGS's beam of protons was used to produce a shower of pions after slamming into a beryllium target. These pions would travel toward a 5,000-ton steel wall (constructed from old battleship plates!) and they would decay into muons and neutrinos, but only neutrinos would be able to pass through the steel wall into a spark chamber filled with neon. As neutrinos coursed through this chamber, one neutrino would occasionally hit a proton in an aluminium nucleus which would produce muon tracks, instead of the showers produced from electrons, proving that there were muon neutrinos in the neutrinos that passed through the chamber.

In 2000 the DONUT collaboration (Direct Observation of NU Tau) at Fermilab detected the existence of the tau neutrino [18]. A beam of neutrinos (which they expected to contain tau neutrinos) was fired at iron plates with alternating layers of emulsion, and very very small number of these tau neutrinos interacted with an iron nucleus to produce the tau lepton, which decayed leaving a track in the emulsion. These tracks contained a kink, which were a sign of the tau neutrino, and only four such tracks were detected out of a possible six million.

1.1.3 The Solar Neutrino Problem

The Standard Solar Model predicts that most of the solar neutrino flux (about 90%) come from the proton-proton chain reaction, where the solar neutrinos produced have energies below 0.4 MeV. Figure 1.1 shows the processes which make up the pp chain, along with the branching percentages where it produces a neutrino.

Only experiments that use Gallium can detect neutrinos with this energy, whereas ex-

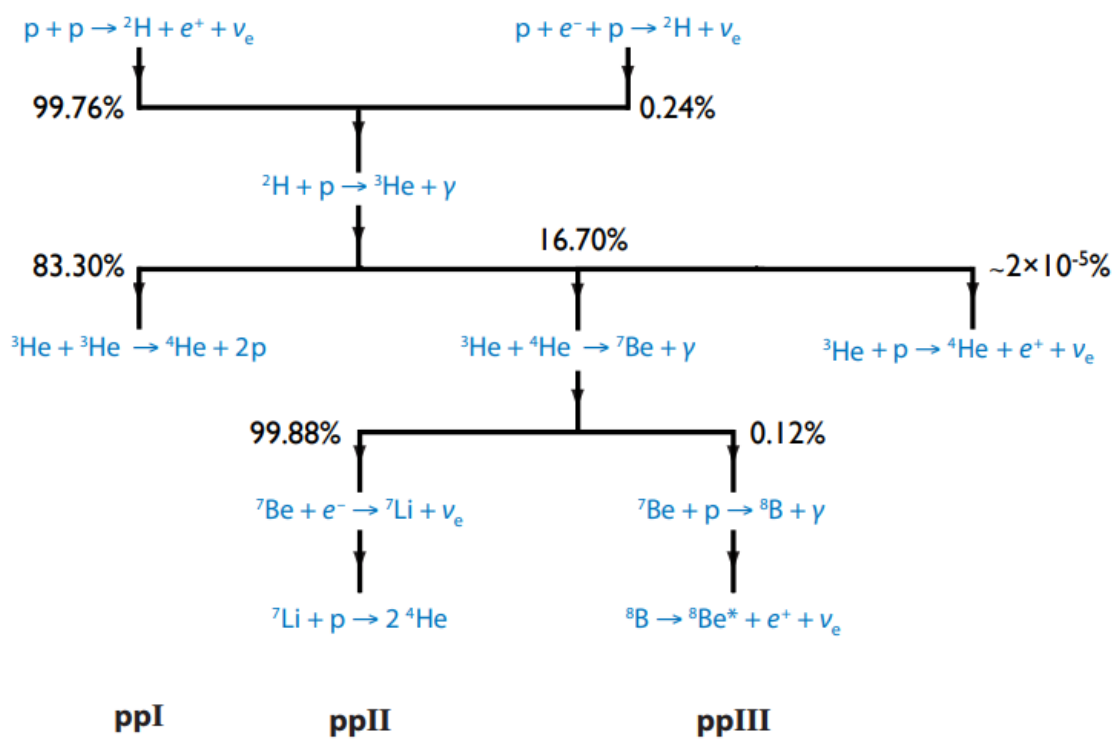


Figure 1.1: Proton-proton chain cycle with branching percentages shown

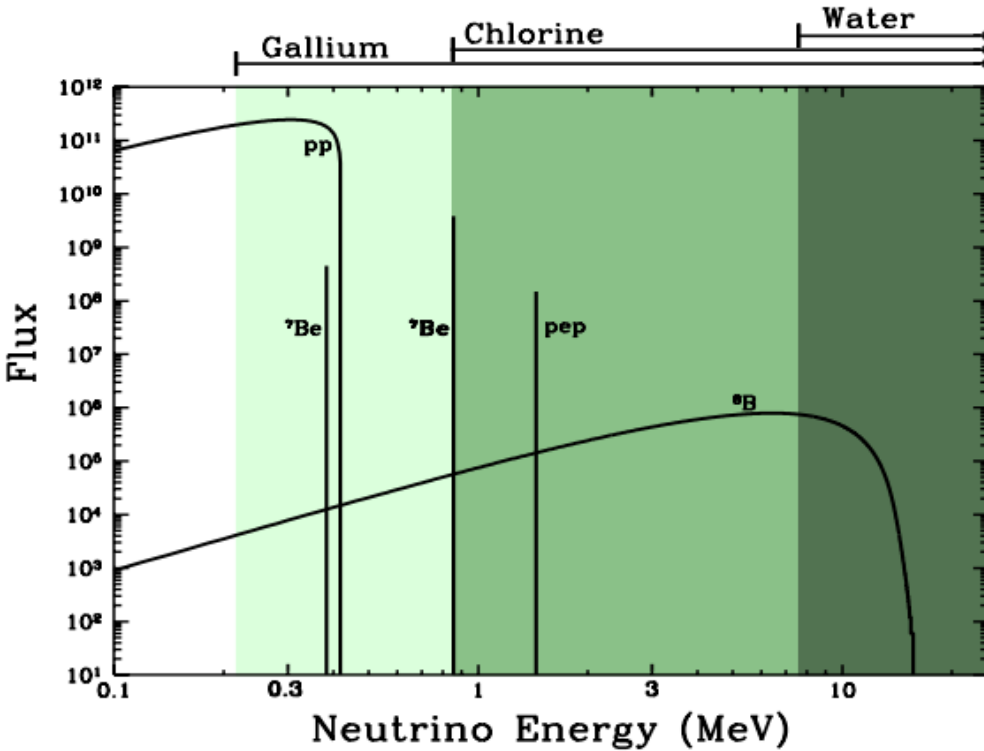


Figure 1.2: Solar neutrino fluxes predicted by Bachall's Standard Solar Model, and which experiments are able to detect them. [9]

periments whose detector medium is Chlorine can observe neutrinos from ${}^7\text{Be}$ (production equation of which is shown in Figure 1.1). Experiments whose detector medium is water (such as Super-Kamiokande and SNO) can only see the ${}^8\text{B}$ neutrinos, as shown in Figure 1.2.

In the 1960s, the Homestake experiment made the first measurement of solar electron neutrino flux [15]. The experiment used a perchloroethylene-based detector, placed 1,478 metres underground in the Homestake Gold Mine in South Dakota. When an electron neutrino interacts with ${}^{37}\text{Cl}$ in the perchloroethylene, the ${}^{37}\text{Cl}$ becomes a radioactive isotope of ${}^{37}\text{Ar}$ which is extracted by bubbling helium through the tank, and then counted in order to determine how many neutrinos had been captured. The theoretical solar neutrino flux calculated by John Bachall was about three times as much as Raymond Davis' results from the experiment: with Bachall's calculations predicting a solar neutrino flux of 8.1 ± 1.2

SNU, whereas the Homestake experimental results showed a flux of 2.56 ± 0.25 SNU. These results were consistent with those from the subsequent Kamiokande, SAGE and GALLEX experiments. Super-Kamiokande's main detection channel for solar neutrinos is the elastic-scattering channel, which has a minimum energy threshold value (recoil electron kinetic energy) of 5 MeV. In this channel, Super-Kamiokande observed a solar neutrino capture rate of 0.45 ± 0.02 SNU, while the solar neutrino model prediction was 1.0 ± 0.2 SNU. Turning our attention to the results of the Gallium experiments, namely SAGE and GALLEX, they also showed a discrepancy regarding the solar model predictions. Due to their sensitivity to the bulk of the proton-proton chain neutrino flux, they have a larger solar neutrino capture flux rate, with SAGE observing 70.8 ± 5.0 SNU, and GALLEX observing 77.5 ± 8.0 SNU, while the model prediction was 129 ± 9.0 SNU, a difference of about 40%. This discrepancy of experimental results compared with the Standard Solar Model prediction became known as the Solar Neutrino Problem.

The way to combat this discrepancy and prove that the cause of the Solar Neutrino Problem was neutrino oscillations was finding a way to detect solar neutrino flux which was not dependent on neutrino flavour. Due to these experiments only detecting solar neutrinos through charged current interactions, they wouldn't be able to detect muon or tau neutrinos. However, with the Sudbury Neutrino Observatory (SNO) experiment this would change, as SNO used heavy water D_2O as its detector medium. Deuteron consists of a proton and a neutron and due to how little energy it takes to break it apart (2.2 MeV), an electron, muon or tau neutrino can very easily break it apart, so that SNO can detect the final state neutron then muon and tau neutrinos would be visible to the detector. The three main channels SNO uses to detect neutrinos is the elastic scattering channel, the charged current channel, and the neutral current channel. Elastic scattering allows SNO to see muon and tau neutrino flux given by $\phi(\nu_e + 0.15(\phi(\nu_\mu) + (\nu_\tau)))$. The most important neutrino interaction channel regarding SNO being able to measure the muon and tau neutrino flux is the neutral current (NC) channel (shown in Equation 1.1), as it allows SNO to measure the total flux.

$$\nu + d \rightarrow n + p + \nu \quad (1.1)$$

Using these two reaction channels, along with the charged current channel (CC), which can only measure electron neutrino flux, SNO was able to measure the individual neutrino flavour fluxes, shown in Equation 1.2.

$$\begin{aligned}\phi_{CC} &= \phi(\nu_e) = 1.76 \pm 0.0110^{-8} \text{ cm}^{-2} \text{ s}^{-1} \\ \phi_{ES} &= \phi(\nu_e) + 0.15(\phi(\nu_\mu) + \phi(\nu_\tau)) = 2.39 \pm 0.2610^{-8} \text{ cm}^{-2} \text{ s}^{-1} \\ \phi_{NC} &= \phi(\nu_e) + \phi(\nu_\mu) + \phi(\nu_\tau) = 5.09 \pm 0.6310^{-8} \text{ cm}^{-2} \text{ s}^{-1}\end{aligned}\tag{1.2}$$

From Equation 1.2, you can see that the flux of muon and tau neutrinos from the Sun is $\phi(\nu_\mu) + \phi(\nu_\tau) - \phi(\nu_e) = 3.33 \pm 0.62$, which is 3 times that of the value for $\phi(\nu_e)$, and as we know that the Sun only produces ν_e , it means that the neutrinos must be changing flavour to mu and tau neutrinos on their journey to Earth, definitely solving the solar neutrino problem.

1.1.4 Neutrino Oscillation Theory

In 1957, Bruno Pontecorvo postulated that neutrinos could transition from neutrinos to antineutrinos and vice versa (similarly to how two kinds of neutral kaons \bar{K}_0 , and K_0 were found to oscillate) [31]. Neutrino flavour oscillation theory was then developed by Maki, Nakagawa and Sakata in 1962. The PMNS matrix (Pontecorvo-Maki-Nakagawa-Sakata matrix) is the neutrino analogue of the Cabibbo-Kobayashi-Masakawa quark mixing matrix [23], and is shown in Equation 1.3 as $(U_{\alpha i}^*)$ which shows the relationship between the mass and flavour eigenstates for a neutrino with a definite flavour of α and a definite mass of m_i .

$$\begin{aligned}|\nu_\alpha\rangle &= \sum_i U_{\alpha i}^* |\nu_i\rangle \\ |\nu_i\rangle &= \sum_\alpha U_{\alpha i} |\nu_\alpha\rangle\end{aligned}\tag{1.3}$$

In Equation 1.3, the terms $U_{\alpha i}^*$ and $U_{\alpha i}$ are the complex conjugate and normal PMNS matrix. Equation 1.4 shows the 3x3 form of the PMNS matrix, where $c_{ij} = \cos\theta_{ij}$ and $s_{ij} = \sin\theta_{ij}$.

$$\begin{aligned}
U &= \begin{pmatrix} 1 & 0 & 0 \\ 0 & c_{23} & s_{23} \\ 0 & -s_{23} & c_{23} \end{pmatrix} \begin{pmatrix} c_{13} & 0 & s_{13}e^{-i\delta_{CP}} \\ 0 & 1 & 0 \\ -s_{13}e^{i\delta_{CP}} & 0 & c_{13} \end{pmatrix} \begin{pmatrix} c_{12} & s_{12} & 0 \\ -s_{12} & c_{12} & 0 \\ 0 & 0 & 1 \end{pmatrix} \quad (1.4) \\
&= \begin{pmatrix} c_{12}s_{13} & s_{12}c_{13} & s_{13}e^{-i\delta_{CP}} \\ -s_{12}c_{23} - c_{12}s_{13}s_{23}e^{i\delta_{CP}} & c_{12}c_{23} - s_{12}s_{13}s_{23}e^{i\delta_{CP}} & c_{13}s_{23} \\ s_{12}s_{23} - c_{12}s_{13}c_{23}e^{i\delta_{CP}} & c_{12}s_{23} - s_{12}s_{13}c_{23}e^{i\delta_{CP}} & c_{13}c_{23} \end{pmatrix}
\end{aligned}$$

In Equation 1.4, if the $\sin \delta_{CP}$ terms are not equal to 0, it means that there will be imaginary terms in the matrix, which will contribute to CP (charge-parity) violation. The angles θ_{12} , θ_{23} and θ_{13} are mixing angles.

Two-flavour neutrino oscillations in vacuum

If a neutrino is produced in the flavour state $|\nu_\alpha\rangle$ in a vacuum, using the PMNS matrix for the relationship between the mass eigenstate and the flavour eigenstate, propagating the neutrino according to the time-dependent Schrodinger equation with no potential would yield a solution to this equation as a plane wave, shown in Equation 1.5.

$$i\frac{\partial}{\partial t} |\nu_i(x, t)\rangle = E |\nu_i(x, t)\rangle = -\frac{1}{2m_i} \frac{\partial^2}{\partial x^2} |\nu_i(x, t)\rangle \quad (1.5)$$

The solution to Equation 1.5 is a plane wave of the form shown in Equation 1.6.

$$|\nu_k(x, t)\rangle = e^{-i(E_k t - p_k x)} |\nu_k(0, 0)\rangle = e^{-i\phi_k} |\nu_k(0, 0)\rangle \quad (1.6)$$

The probability of oscillation to flavour state $|\nu_\beta\rangle$ at time t is given by Equation 1.7.

$$\begin{aligned}
P(\nu_\alpha \rightarrow \nu_\beta) &= |\langle \nu_\beta | \nu_\alpha(t) \rangle|^2 \quad (1.7) \\
&= \sum_{i,j} (U_{\beta i}^*)(U_{\beta i})(U_{\alpha j})(U_{\beta j}^*) e^{-i(E_i - E_j)t}
\end{aligned}$$

For a two-flavour oscillation probability calculation, the matrix which transforms a vector in flavour basis into mass basis is simply a 2x2 rotation matrix (where θ is the mixing angle) so that:

$$\begin{pmatrix} \nu_\alpha \\ \nu_\beta \end{pmatrix} = \begin{pmatrix} \cos \theta & \sin \theta \\ -\sin \theta & \cos \theta \end{pmatrix} \begin{pmatrix} \nu_1 \\ \nu_2 \end{pmatrix}$$

One could calculate the probability of a neutrino of flavour α oscillating into a neutrino of flavour β by using the formula in Equation 1.8. Here L is the distance travelled by the neutrino in kilometres, Δm^2 is the difference between the mass eigenstates, and E is the difference between the energy of the mass eigenstates (where an assumption has been made that the mass eigenstates are the same for both.) The survival probability of a neutrino of flavour α (i.e. the probability of generating ν_α and detecting ν_α) is $P(\nu_\alpha \rightarrow \nu_\alpha) = 1 - P(\nu_\alpha \rightarrow \nu_\beta)$ for two flavour oscillations.

$$P(\nu_\alpha \rightarrow \nu_\beta) = \sin^2(2\theta) \sin^2\left(1.27\Delta m^2 \frac{L}{E_\nu}\right) \quad (1.8)$$

Neutrino oscillation matter effects

The presence of dense matter affects the vacuum neutrino oscillation probability, since neutrinos interact via the weak interaction with matter. This is called the Mikheyev-Smirnov-Wolfenstein (MSW) effect: due to ordinary matter containing only electrons, and muons and tauons, the charge current interactions only affects electron neutrinos and creates an additional potential which affects the vacuum oscillation probability for electron neutrinos, shown in Equation 1.9, where G_F is the Fermi coupling constant, and n_e is the number density of electrons in the matter, where the positive sign applies to neutrinos, and the negative sign applies to anti-neutrinos.

$$V_{CC} = \pm \sqrt{2} G_F n_e \quad (1.9)$$

Replacing Δm^2 with Δm_M^2 and $\sin^2 \theta$ with $\sin^2 \theta_M$ gives the two flavour oscillation probability modified to take into affect the MSW effect (shown in Equation 1.10, where the factor of $A = 2|V_{CC}|E$).

$$\begin{aligned} \sin 2\theta_M &= \frac{\sin 2\theta}{\sqrt{\sin^2 2\theta + (\cos 2\theta - A/\Delta m^2)^2}} \\ \Delta m_M^2 &= \Delta m^2 \sqrt{\sin^2 2\theta + (\cos 2\theta - A/\Delta m^2)^2} \end{aligned} \quad (1.10)$$

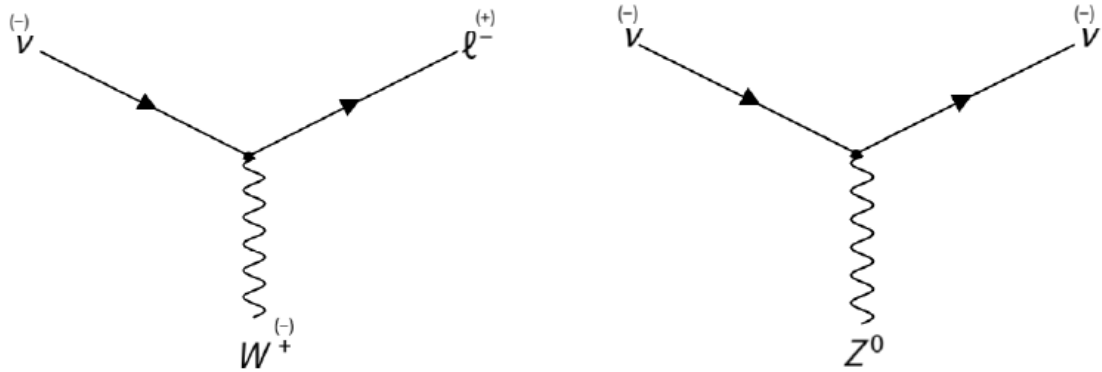


Figure 1.3: Feynman diagrams of charged-current (left) and neutral-current (right) neutrino interactions

1.1.5 Neutrino-nucleus interactions in Super-Kamiokande Gd

Understanding neutrino interaction modes, and understanding neutrino nucleus interaction modes, in particular the neutral current quasielastic reaction is key to understanding this analysis.

There are two main types of neutrino interaction: charged-current (CC) and neutral current (NC). The former occurs when a W^\pm boson is involved in a nuclear exchange, and the latter occurs when a Z^0 is involved (see Figure 1.3).

One such interaction, and often the simplest interaction, is neutrino-electron elastic scattering ($\nu + e^- \rightarrow \nu + e^-$), which occurs when a neutrino scatters off an electron with a virtual vector boson being exchanged. This type of scattering is used in the detection of low energy neutrinos, primarily those from the sun. Figure 1.4 shows the Feynman diagrams for this kind of interaction.

There are multiple types of neutrino-nucleus interactions that occur which can be either charged current or neutral current interactions. These are given in order of momentum transfer (q^2), with the lowest neutrino energies producing quasi-elastic scattering for charged current interactions, and elastic scattering for neutral current interactions, up to deep inelastic scattering where the target nucleus breaks up.

Starting off with the neutrino-nucleus interaction with the lowest q^2 , the Feynman diagrams for NC elastic and CCQE interactions by a muon neutrino interacting with a neutron are shown in Figure 1.5.

The type of interaction that occurs at higher neutrino energies, i.e. with more q^2 avail-

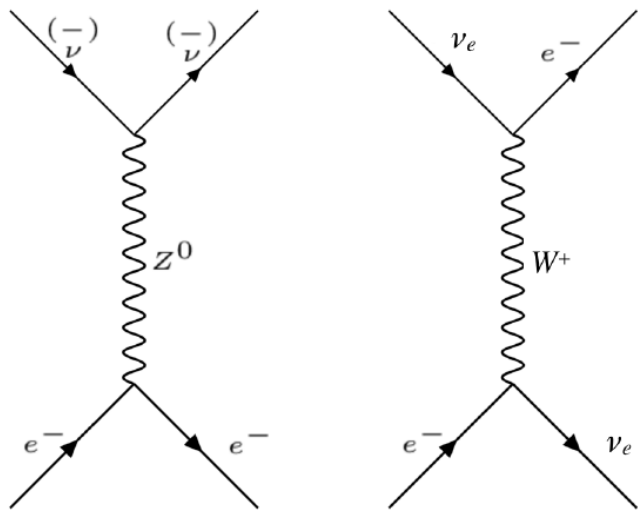


Figure 1.4: Feynman diagrams of neutral-current (left) and charged-current (right) neutrino-electron scattering

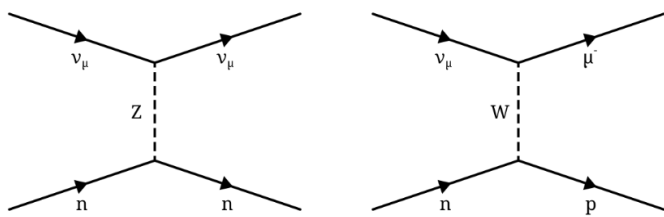


Figure 1.5: Feynman diagram for ν_μ NC elastic scattering (left) and ν_μ CCQE scattering (right)

able is resonance production. Single mesons can also be produced via neutrino-nucleon reactions: these are mostly pions, but some kaons and eta particles can also be produced. Here a neutrino with a high enough energy interacts with and excites a nucleon, producing a resonant baryon which decays to a nucleon and a single pion (shown in Equation 1.11), where N and N' are nucleons.

$$\begin{aligned} \nu_l + N &\rightarrow l + N^* \\ N^* &\rightarrow \pi + N' \end{aligned} \tag{1.11}$$

The resonant baryon produced during the reaction is usually a $\Delta(1232)$ resonance. Single pion final states can also be produced by a neutrino which scatters off an entire nucleus (X), shown in Equation 1.12 for the charged current reactions and Equation 1.13 for neutral current reactions.

$$\nu_l + X \rightarrow l^- + X + \pi^+, \quad \bar{\nu}_l + X \rightarrow l^+ + X + \pi^- \tag{1.12}$$

$$\nu_l + X \rightarrow \nu_l + X + \pi^0, \quad \bar{\nu}_l + X \rightarrow \bar{\nu}_l + X + \pi^0 \tag{1.13}$$

At higher energies (above 1 GeV), neutrino interactions can also produce kaons in the final state, due to the higher energies being able to produce strange quarks.

At even higher energies and greater q^2 , deep inelastic scattering is able to occur. Deep inelastic scattering is a type of neutrino interaction where the neutrino scatters off a quark inside the proton or neutron involved in the exchange, via a W (CC) or Z (NC) boson (Equation 1.14), shown in Figure 1.6.

$$\begin{aligned} \nu_l + N &\rightarrow l^- + X, \quad \bar{\nu}_l + N \rightarrow l^+ + X(\text{CC}) \\ \nu_l + N &\rightarrow \nu_l + X, \quad \bar{\nu}_l + N \rightarrow \bar{\nu}_l + X(\text{NC}) \end{aligned} \tag{1.14}$$

The next two neutrino-nucleus interactions explained here are of particular relevance to the analysis in this thesis: inverse beta decay (IBD) and quasi-elastic scattering.

Inverse beta decay is the reaction by which Cowan and Reines first detected electron antineutrinos: it is important at low energies: from the minimum energy for the reaction



Figure 1.6: Feynman diagram for a charged current deep inelastic scattering interaction with an incoming muon neutrino

to take place ($E_\nu = 1.806$ MeV) to tens of MeV. Diffuse Supernova Neutrino Background and low energy antineutrinos produced from nuclear reactors can be detected via this process. Figure 1.7 shows the Feynman diagram for this reaction. The neutron produced by this reaction is integral to the motivation behind the Gadolinium-doping upgrade to Super-Kamiokande, which will be explained in the next section.

Finally, we get to the type of interaction investigated in this thesis: quasi-elastic scattering. This makes up the majority of the neutrino-nucleus interaction cross-sections at the energy range from 100 MeV to 2 GeV, and therefore vital for the study of neutrinos from long baseline neutrino experiments and also low energy atmospheric neutrinos. Equation 1.15 shows the equations for both the charge current (CCQE) and neutral current (NCQE) version of this interaction where the incoming neutrino scatters off a nucleon.

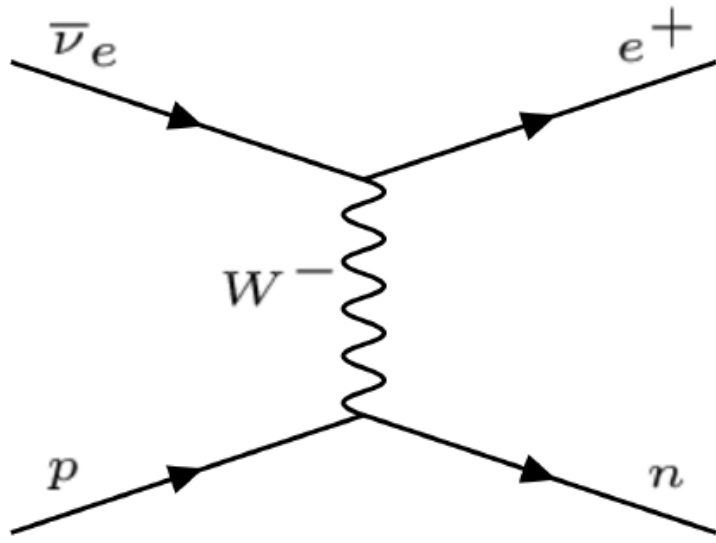


Figure 1.7: Feynman diagram for the inverse beta decay reaction

$$\text{CC} : \nu(k) + n(p) \rightarrow l^-(k') + p(p') \quad (1.15)$$

$$\bar{\nu}(k) + p(p) \rightarrow l^+(k') + n(p')$$

$$\text{NC} : \nu(k) + N(p) \rightarrow \nu(k') + N(p')$$

$$\bar{\nu}(k) + N(p) \rightarrow \bar{\nu}(k') + N(p')$$

As this analysis relates to the various properties of neutrons produced from NCQE interactions in Super-Kamiokande Gd, it is worth looking at the interactions where neutrons are produced inside the detector medium. In Water Cherenkov detectors, the incoming neutrino or anti-neutrino interacts with an ^{16}O nucleus, and at neutrino energies greater than 200 MeV, a nucleon is knocked out, as shown in Equation 1.16.

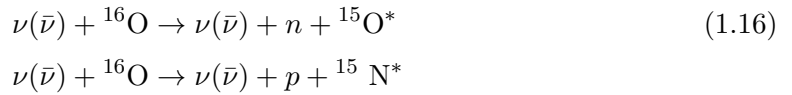




Figure 1.8: Feynman diagram for a quasi elastic scattering interaction off a nucleon

This interaction happens in stages, where there is the initial reaction between the incoming neutrino and the specific nucleon inside the ^{16}O nucleus, hadronic final state interactions (FSI) inside the nucleus itself, and subsequent hadronic secondary interactions (SI) inside the detector medium. These are outlined in the schematic shown in Figure 1.9, with the primary interaction, taken as the CCQE reaction ($\bar{\nu}(k) + p(p) \rightarrow l^+(k') + n(p')$). There are stages to neutrino-nucleus reactions, and for the CCQE reaction shown in Figure 1.9, there are three processes: the initial neutrino-nucleon reaction ($\bar{\nu}(k) + p(p) \rightarrow l^+(k') + n(p')$), the final state interaction (FSI) inside the ^{16}O nucleus ($p + p \rightarrow p + n + \pi^+$), and the secondary (SI) interaction in the detector medium ($n + ^{16}\text{O} \rightarrow n + n + ^{15}\text{O}^*$). All interactions inside the nucleus are referred to as hadronic final state interactions, and when they move through the detector medium and leave the target nucleus they are known as hadronic secondary interactions.

1.1.6 Supernova Relic Neutrinos

A key feature of the analysis presented in this thesis is that it is an investigation into the significant background of the signal for SRN. It is therefore important to state and understand the process behind the production of supernova relic neutrinos in order to get a firm handle on the motivation behind this analysis.

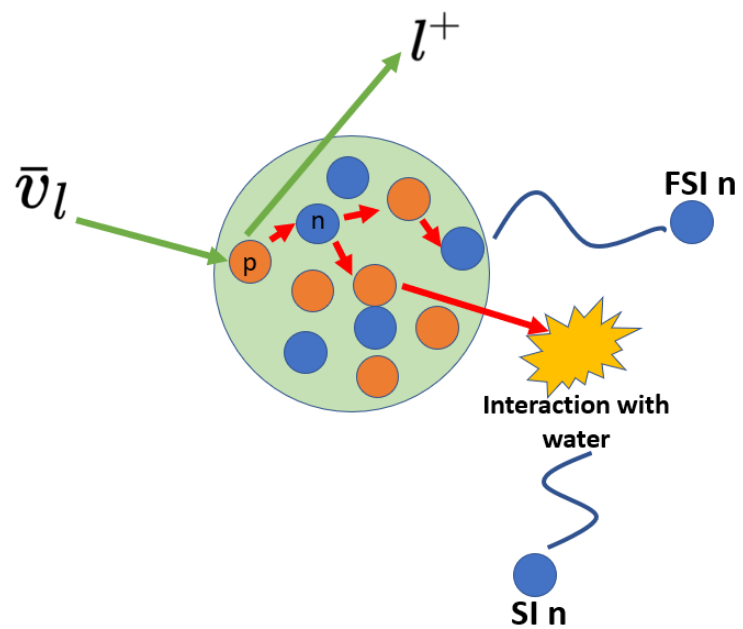


Figure 1.9: Schematic of neutron production following the interaction of neutrino with a nucleon inside an ^{16}O and the resulting FSI and SI interactions in the detector medium.

Supernovae Classification

Supernovae occur when a star with a mass around eight times the mass of our sun explodes, and in a galaxy these occur only a few times in a century. Supernovae are classified into different types: Type 1a, Type 1b, Type 1c and Type II. The classification of supernovae are determined by looking at the spectral lines in the light emitted from these supernovae. Table 1.1.6 shows how these supernovae are classed and which spectral line elements are associated with each class.

Supernova Classification	Element lines present in spectra
Type 1a	No hydrogen, silicon
Type 1b	No hydrogen, no silicon, helium
Type 1c	No hydrogen, no silicon, no helium
Type II	Hydrogen

The kinetic energy of a supernova is 10^{44} J, and 99 % of the energy from core-collapse supernovae (CCSN) are released in the form of neutrinos. Unlike Type 1a supernovae which are usually thermonuclear supernovae, Type 1b, Type 1c and Type II are core-collapse supernovae, from which more neutrinos are emitted which is why these types of supernovae are of more interest.

Core-Collapse Supernovae Mechanism

Using the pressure produced by the process of nuclear fusion, a star is able to support itself against gravitational collapse. During the proton-proton chain reaction, hydrogen will fuse to produce helium and once temperatures and pressures are high enough, helium fusion will occur. After all the helium in the core is used up in the fusion process, the star will contract until the pressure and temperatures get even higher, allowing more massive nuclei to fuse. This reaction will carry on until iron nuclei are produced, this being the element with the highest binding energy, causing the fusion to stop.

As more and more iron accumulates in the core of the star, the density and temperature of the core will increase, and these higher energy electrons will increase the rate of electron capture on protons that will occur in the iron nuclei. This will cause a reduction in the electron degeneracy pressure, which is further enhanced by the breakdown of the iron nuclei which occurs at higher temperatures when gamma rays interact with them. The degeneracy pressure is no longer greater than the gravitational forces acting inwards, and gravitational



Figure 1.10: Schematic showing core collapse of a star, and the resultant shockwave and neutrino production

core collapse occurs.

The point at which in the core the neutrino mean free paths become approximately the same size as the proto-neutron star is called the “neutrinosphere”. Figure 1.10 shows the formation of a proto-neutron star (PNS) and the neutrino flux and neutrinosphere produced by the core-collapse mechanism.

The radius of the neutrinosphere becomes as large as that of the inner core of the star, when the inner core of the star reaches a density of $10^{11} \text{ g cm}^{-3}$, and the electron neutrinos produced from electron capture become unable to escape. Gravitational collapse of the star continues until the inner core reaches nuclear density, at which point a shock wave is produced due to the repulsive force between nuclei.

When this shock wave reaches the neutrinosphere, neutrino emission begins, which lasts less than 10 milliseconds. After this shockwave passes, nucleons and electrons fall back onto the proto-neutron star which heats it up. This causes neutrinos of all flavours to be

produced via pair production and electron capture. This is called the “accretion phase”. Due to this expulsion of neutrinos the shock wave loses energy, but it is revived through matter behind the shock wave being heated by neutrino absorption from the proto-neutron star region. The mechanism for this shown in Figure 1.11, where the shockwave produced depends on antineutrinos being absorbed by the dense post-shock gas.

After the shock wave is revived, if it has enough energy to blow off the outer layer of matter a supernova occurs. Then, depending on the mass of the PNS, it cools to either become a neutron star or a black hole. If the shock wave energy is not high enough to blow off the outer layer of matter, the accretion phase continues until a black hole is formed.

The energy of the emitted neutrinos depend on their flavour - neutrinos emitted from a deeper layer inside the supernova will be higher in temperature and therefore have a higher energy. For electron neutrinos and electron anti-neutrinos, the dominant interactions are charged current interactions with nucleons. Due to the number of neutrons in a proto-neutron star greatly outnumbering the number of protons, the interaction involving ν_e will be far more efficient than those involving $\bar{\nu}_e$, meaning the neutrinosphere for $\bar{\nu}_e$ is smaller than for ν_e , so they are emitted from the PNS with greater energies.

Due to there being no charged current interactions involving muon neutrinos in the medium, they are involved instead in neutral current reactions, including Bremsstrahlung, neutrino-pair annihilation, and electron-positron pair annihilation. Due to only undergoing these reactions their neutrinosphere is even smaller than that of their electron neutrino and electron anti-neutrino counterparts, therefore being emitted with even higher energies [28]. Figure 1.12 shows the luminosity (top panels) and average energy (bottom panels) for three different neutrino flavours as a function of time for the neutronisation phase (left), accretion phase (centre) and cooling phase (right). Taken from [14].

Kamiokande-II observed neutrinos produced from a supernova, later named 1987A, in the Large Magellanic Cloud. These neutrinos were also observed by the Baskan Neutrino Observatory and the Irvine-Michigan-Brookhaven detector (IMB) [21]. The neutrinos detected from 1987A were detected via the inverse beta decay (IBD) interaction (shown in Figure 1.7), as opposed to the electron elastic scattering, CC interaction with ^{16}O or NC interaction with ^{16}O channels. The positron from this reaction is what is searched for, and these positrons are produced isotropically within the detector. A neutrino burst search from SN1987A was carried out on the data run which ran continuously between 16:09 21

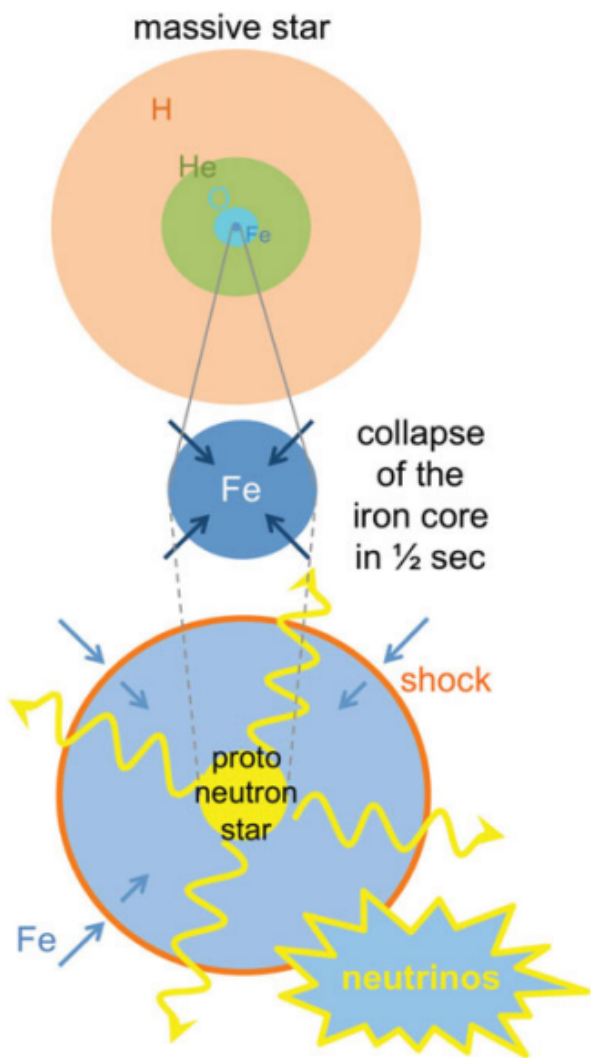


Figure 1.11: Schematic showing core collapse of a star, and the resultant shockwave and neutrino production

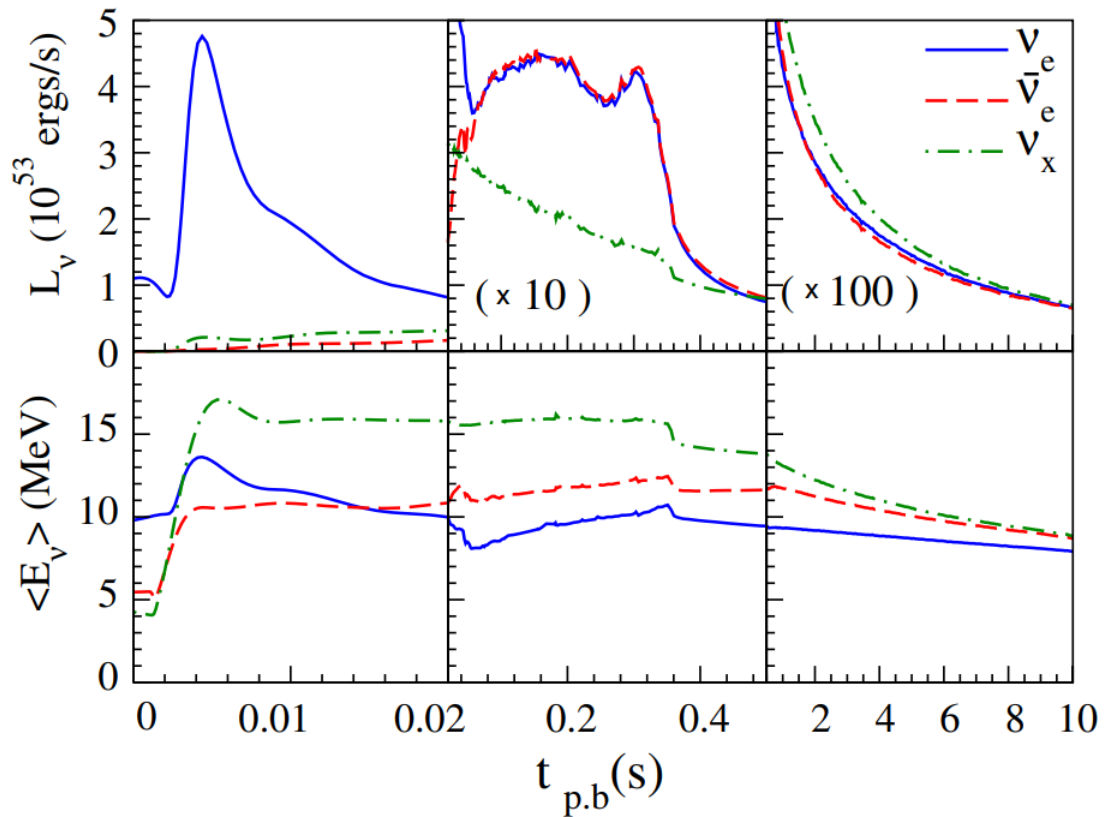


Figure 1.12: Luminosity (top panels) and average energy (bottom panels) for three different neutrino flavours as a function of time for the neutronisation phase (left), accretion phase (centre) and cooling phase (right). Taken from [14].

February 1987 to 07:31 24th February 1987 JST [22].

The event selection criteria for a supernova neutrino event were as follows: firstly, the total number of photoelectrons per event should be less than 170, as this corresponds to an electron with an energy of 50 MeV, and the neutrinos released from a supernovae have a typical energy of the order of 10 MeV. Secondly, the total number of electrons in the outer detector per event needed to be less than 30, in order for the event to be considered fully contained, and finally, the time between previous events has to be greater than 20 μ sec, in order to avoid electrons produced from Michel electrons. Figure 1.13 shows the time-sequence of all low-energy events. If the neutrinos were to show up in Kamiokande-II, they would arrive in a cluster lasting of order 10s, so intervals of 10 seconds were used to search for clusters of events. In order to classify the event as a supernova neutrino candidate, the event had to be registered by atleast 30 PMTs, and 6 events were found in the first 10s interval which satisfied this, and 2 events in the next 10s interval. A second search was performed on a larger data sample of 42.9 days, from 9th of January to 25th of February 1987, and no other supernova neutrino burst candidates were found. The first two events shown in Figure 1.13 also correlate in angle to the direction of 1987A. As a result, this was considered detection of a genuine supernova neutrino burst, and was the first direct observation of this in neutrino astronomy.

Due to neutrinos carrying away 99% of the energy produced by supernovae, they are the most important signal a supernova can produce, and can be used for finding out when the supernova explosion actually happened - due to neutrinos leaving the supernovae immediately while gamma rays from the the explosion can only leave the supernova when the shock wave reaches the surface of the star [11].

The supernova relic neutrinos emitted from all past CCSN are accumulated and form an everpresent background due to the fact that neutrinos only weakly interact with matter. The total flux of this neutrino background has been theoretically predicted and is called the “diffuse supernova neutrino background” (DSNB). When calculating the total DSNB flux, the redshift caused by the expansion of the universe needs to be taken into account.

Equation 1.17 gives the differential of the DSNB flux with respect to the DSNB energy at Earth.

$$dn_\nu(E_\nu) = R_{\text{SN}}(z) \frac{dt}{dz} dz \frac{dN_\nu(E'_\nu)}{dE'_\nu} (1+z)dE_\nu \quad (1.17)$$

Here $E'_\nu = (1+z)E_\nu$ is the energy of neutrinos at a certain redshift z , $R_{\text{SN}}(z)$ is the

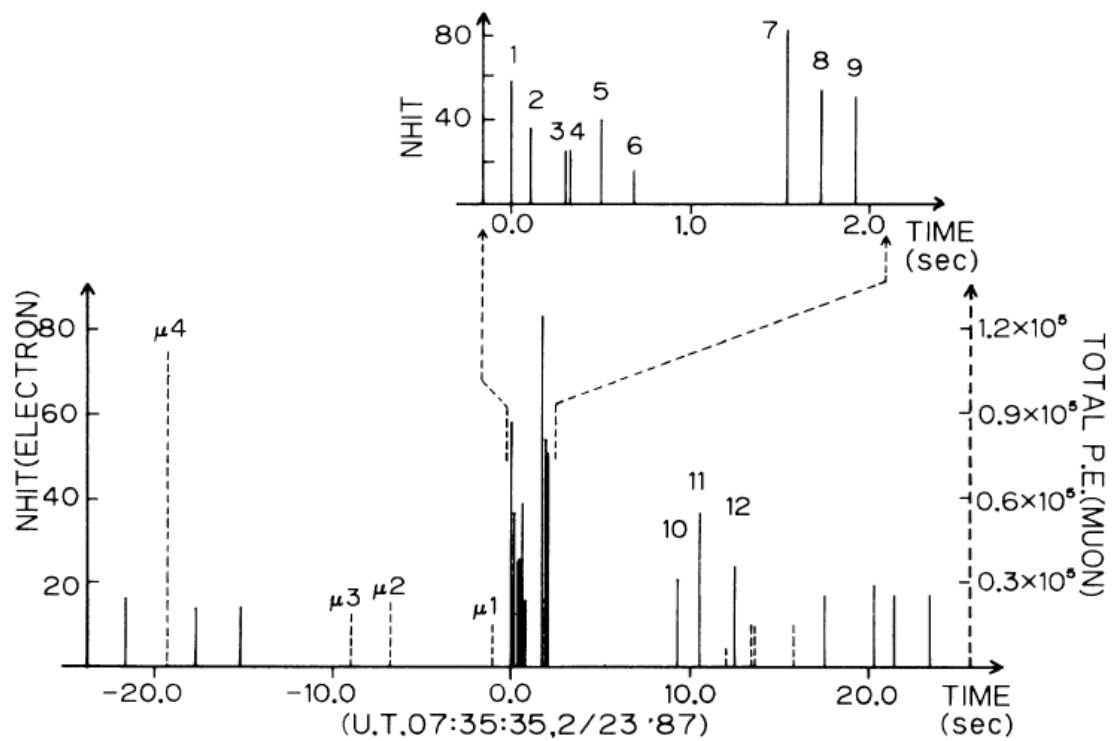


Figure 1.13: Events detected centered on 16:35:35 JST, where the solid lines are the number of hit PMTs and dashed lines are muon events. The zoomed in plot in the top-right shows an expanded version of the 0.0 - 2.0 second time scale.

supernova rate at a comoving volume at z , dN_ν/dE_ν is the number spectrum of neutrinos emitted by one supernova explosion, and $(1+z)^{-3}$ is the expansion of the universe factor. The relationship between redshift and time (dt/dz), is given by the Friedmann equation (Equation 1.18), where H_0 is the Hubble constant, Ω_m is the matter density and Ω_Λ is the cosmological constant [8].

$$\frac{dz}{dt} = -H_0(1+z)\sqrt{\Omega_m(1+z)^3 + \Omega_\Lambda} \quad (1.18)$$

It is worth reviewing the lastest searches from Super-Kamiokande for DSNB neutrinos, and the limit on the flux prediction from different Super-Kamiokande phases. While Figure 1.14 shows that the majority of DSNB neutrinos have an energy below 10 MeV, due to massive backgrounds these DSNB are hard to detect, so Super-Kamiokande therefore searches for the DSNB signal in the order of 10 MeV. As mentioned previously the main detection channel is inverse-beta decay, with the prompt signal being the emitted positron and the delayed signal constituting of the photon emission from neutron capture. Up to and including now, there has been no DSNB signal evidence but upper-limits on the flux have been set from both KamLAND and from Super-Kamiokande phases I-IV, shown in Figure 1.15.

Regarding important backgrounds to the DSNB signal, below neutrino energies of 15 MeV NCQE interactions from atmospheric neutrinos form the main background to DSNB searches. The importance of this background motivates the analysis in this thesis: by measuring the NCQE interaction using T2K beam neutrinos, the large uncertainty of this interaction in the low energy region can be reduced due to the reason that the atmospheric neutrino energy region is similar to that of the T2K beam energy region. The differential cross section of the neutral-current elastic interaction of a neutrino on a free proton or neutron can be written as shown in Equation 1.19.

$$\frac{d\sigma^{\nu(\bar{\nu})}}{dq^2} = \frac{M^2 G_F^2}{8\pi E_\nu^2} \left\{ A(q^2) \pm B(q^2) \frac{s-u}{M^2} + C(q^2) \frac{(s-u)^2}{M^4} \right\} \quad (1.19)$$

where E_ν is the initial neutrino or antineutrino energy, M is the mass of the nucleon, G_F is the Fermi coupling constant, s and u are the Mandelstam variables, and q is the transfer of four momentum between incoming (anti)neutrinos and outgoing (anti)neutrinos. Depending on whether it is an incoming neutrino or antineutrino, there is either a plus or a minus between the A and B terms. A,B and C are terms which are made

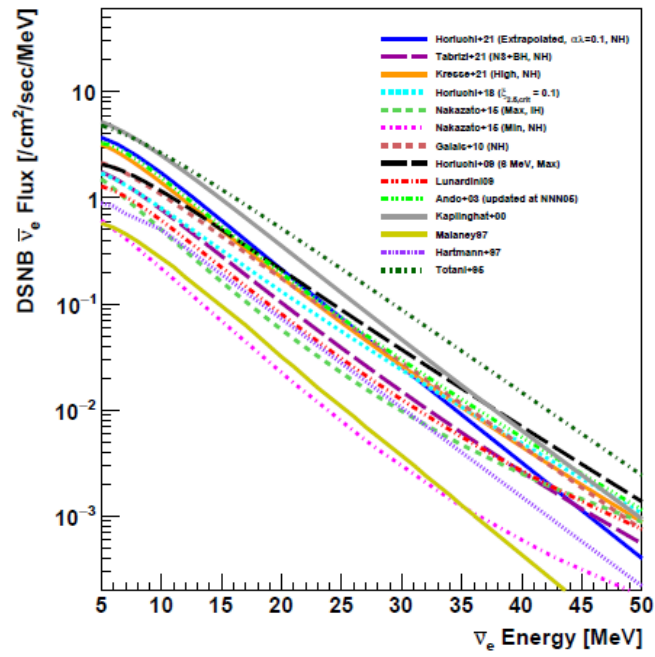


Figure 1.14: DSNB flux against neutrino energy for various theoretical models, "NH" and "IH" are the normal and inverted mass hierarchies respectively

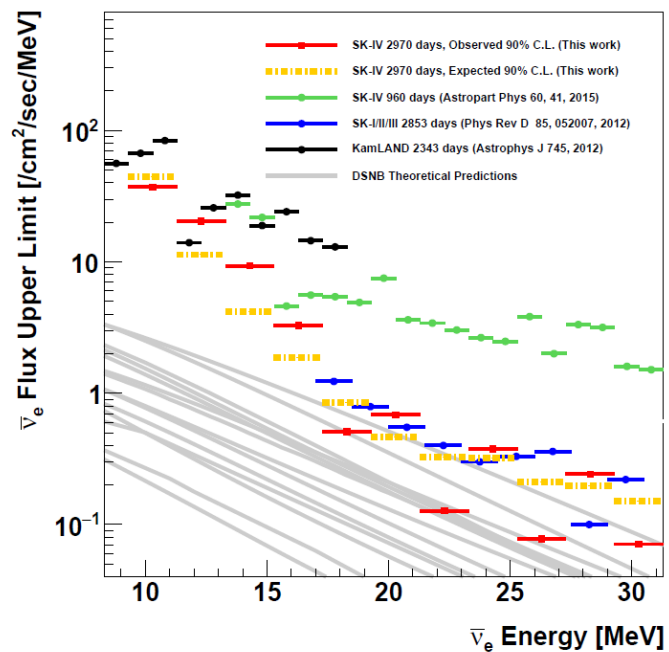


Figure 1.15: The 90% C.L. for observed and expected upper limits on the electron antineutrino flux from SK-I - SK-IV and KamLAND, with the theoretical predictions in Figure 1.14 shown in grey.

up of form factors specific to neutral current interactions. The ideal goal of this analysis is to complement prior analyses which investigate the NCQE cross-section and analyses which produce neutron multiplicity distributions for NCQE interactions, with the added benefit of comparisons to Run 11 T2K data, which brings with it the first beam events with gadolinium in the far detector. The emphasis on the distributions of neutrons in this thesis and the methods of neutron tagging used are of increasing interest due to the fact that the main purpose behind adding Gadolinium to the detector is to make these neutron captures more visible.

Chapter 2

The Tokai-to-Kamioka experiment

2.1 The Tokai-to-Kamioka experiment

The Tokai-to-Kamioka (T2K) experiment is a long baseline neutrino oscillation experiment based in Japan and its purpose is to study neutrino oscillations: specifically a precision measurement of the neutrino oscillation parameters Δm_{23}^2 and $\sin^2 \theta_{23}$ and to improve the measurement of the leptonic CP violating phase δ_{CP} , which is mentioned in Chapter 1. The experiment produces a beam of intense anti-muon neutrinos at J-PARC (Japan Proton Accelerator Research Complex) in Tokai, which is located on the east coast of Japan in Ibaraki Prefecture. The muon neutrino beam travels 295 km west towards the far detector Super-Kamiokande (see Chapter 3.) The neutrino beam is measured by other detectors such as ND280 and INGRID, prior to reaching Super-Kamiokande which is important with regards to measuring the neutrino oscillation parameters. Both ND280 and Super-Kamiokande are off-axis detectors, meaning that they are located 2.5° off axis from the centre of the neutrino beam. This results in the peak of the energy of the muon neutrinos to be 0.6 GeV, maximising the neutrino oscillation on the 295 km baseline. This chapter explains production of the muon neutrino beam from the JPARC proton beam line and the near detector complex.

2.1.1 Neutrino beam production

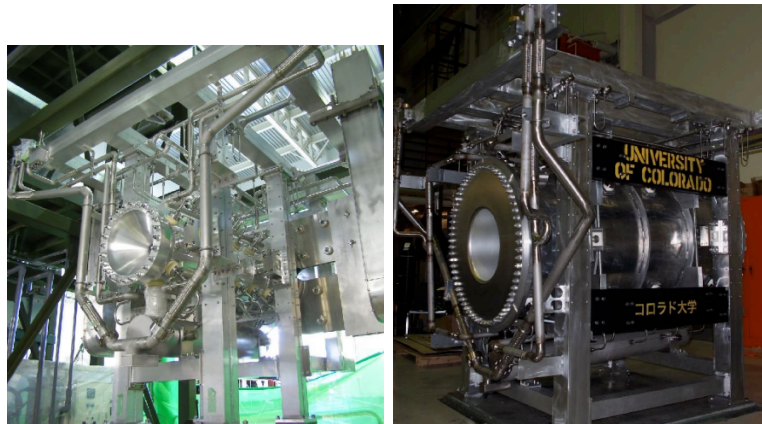
JPARC proton beam production

A sequence of three accelerators results in the production of a proton beam from the JPARC accelerator complex, these are the LINAC (linear accelerator), the RCS (rapid cyclic synchrotron) and the main ring synchrotron (MR). A negative hydrogen ion is accelerated to a kinetic energy of 400 MeV by a linear accelerator (LINAC), from which a beam of protons is created by converting the negative hydrogen ion beam using charge-stripping foils. This proton beam is then accelerated to a kinetic energy of 3 GeV by the RCS, and about 5% of the bunches produced from this process are passed to the MR where the proton beam will be accelerated up to 30 GeV. The rest of the proton bunches are passed to the neutron and muon beamline in the Material and Life Science Facility.

Neutrino beam production

The neutrino beam is produced using the primary and secondary beamline as shown in Figure 2.2. The primary beamline takes the proton beam from the MR and directs it towards Kamioka. The beam is then transferred through a succession of beam monitors which measure facets of the proton beam including the beam profile, intensity and position. The beam monitor which is closest to the graphite target measures the "Protons-On-Target" (POT), a value used to determine the neutrino beam flux. The secondary beamline takes the proton bunches and passes them through a target station, the decay volume and the beam dump. After interacting with the target station, the proton bunches are collimated through a 1.7 m graphite rod where the collimated hole the proton bunches pass through are 30 mm in diameter. Beam profile reconstruction occurs in the OTR (Optical Transition Radiation) monitor, made up of titanium alloy foil placed at a 45 degree angle in order to intercept the beam. As the proton beam enters the foil, the visible light that is produced escapes through a collection of mirrors and is then captured by a charge injection device camera, which creates the beam profile.

After beam profiling, the proton beam then impacts upon a graphite rod target which is 91.4 cm long and 2.6 cm in diameter - this collision produces secondary hadrons, including pions which are focused by three magnetic horns (shown in Figures 2.1a, 2.1b and 2.1c). These magnetic horns can be used to produce either a muon neutrino or muon antineutrino beam depending on the polarity of the 250kA current they are pulsed with. If a +250 kA



(a) T2K Horn 1

(b) T2K Horn 2



(c) T2K Horn 3

current is used, the positive pions and kaons produced can go on to make muon neutrino beams whereas if a -250 kA current is used negative pions and kaons can decay to create muon antineutrino beams (both are shown in Equation 2.1). The +250 kA mode is called Forward Horn Current (FHC) mode and the -250 kA mode is called Reversed Horn Current (RHC) mode. The analysis in this thesis will occur in FHC mode only.



A 75 ton volume beam dump made of graphite and iron stops the particles, specifically

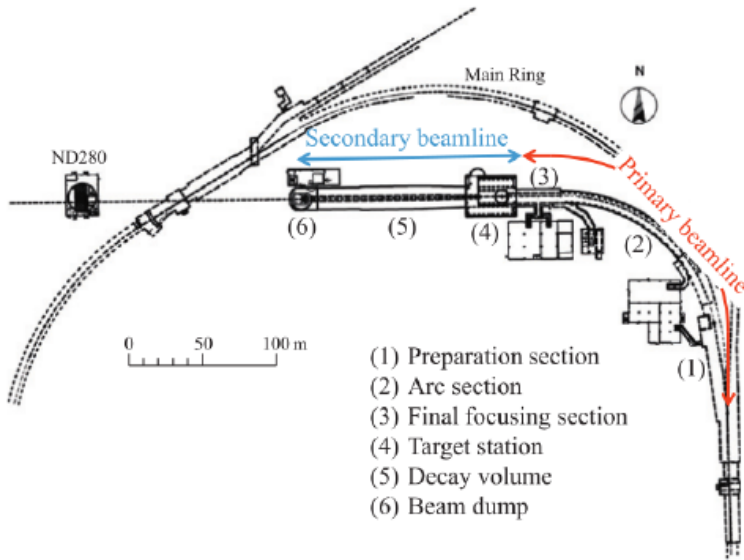


Figure 2.2: Schematic of the neutrino beam line

the protons, secondary hadrons and mesons which have a momentum below $5 \text{ GeV}/c$, and therefore end up being absorbed by the beam dump. A muon monitor is placed after the beam dump in order to directly measure the the beam intensity and beam direction. Muons can be used to monitor the beam properties because along with the neutrinos these are the main particles produced from pion decay. After the muon monitor, a nucleon emulsion plate detector measures the flux and momentum of the muons.

2.1.2 Near detectors

INGRID detector

The INGRID (Ineractive Neutrino GRID) detector is a neutrino detector which unlike ND280 is placed on-axis instead of off-axis. This allows it to directly monitor the direction and the intensity of the neutrino beam by measuring the interactions of the neutrinos with the alternating iron plates that make it up. INGRID is also placed 280 m from the graphite target and consists of 14 modules placed in a cross formation, with the centre of the cross placed at the centre of the neutrino beam. The INGRID modules are comprised of nine iron plates alternating with 11 tracking scintillator planes, which are themselves surrounded by scintillator plates the purpose of which is to reject interactions that occur

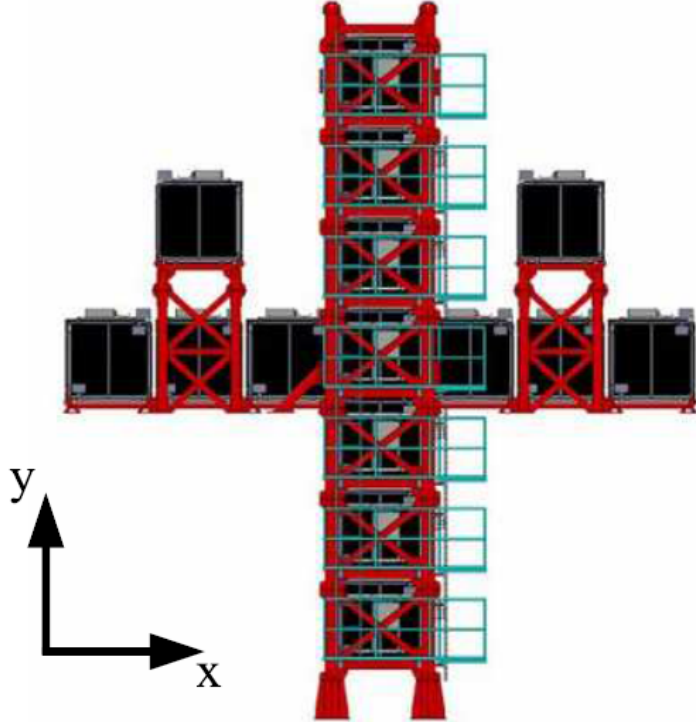


Figure 2.3: Schematic of the INGRID cross taken from [4].

outside the module. A schematic of the INGRID cross is shown in 2.3 and a schematic of the modules is shown in 2.4.

An additional module, called the proton module, was added to more precisely measure the neutrino interaction cross-section with the T2K on-axis neutrino beam. This module is used to distinguish the quasi-elastic interaction channel in order to compare it with Monte Carlo simulations of the beamline and neutrino interactions. The Proton Module is made of scintillator planes (no alternating iron plates) and is contained by veto planes. The Proton Module was placed in the centre of the INGRID cross at the intersection of the vertical and horizontal modules. Figure 2.5 shows what a standard neutrino event looks like on the INGRID module. A neutrino enters from the left and after interacting with the scintillator cells (shown in green) produces hits (shown in red), with the relative size of each circle corresponding to the observed signal in that cell. The blue cells show the



Figure 2.4: Individual INGRID module schematic taken from [4].

position of the veto scintillators, while the gray planes show the iron plates.

By reconstructing the profile of the beam in x and y directions using the number of neutrino events in seven horizontal and vertical INGRID modules, and fitting the profiles with a Gaussian, the centre of the beam can be defined as the peak of the Gaussian fit. The beam direction can then be reconstructed as the direction from the proton beam target to the reconstructed beam centre. Figure 2.6 shows these neutrino beam centres from the centre of INGRID, for both the x and y directions, measured in April 2010 [1].

ND280

ND280 is a near detector which sits 280 m from the target. It is an off-axis detector, meaning that just like Super-Kamiokande, it is placed 2.5 ° off-axis from the center of the beam. This stems from the relationship between the energy of the neutrinos produced from the decay of the pions, a relationship shown in Equation 2.2.

$$E_\nu = \frac{m_\pi^2 - m_\mu^2}{2(E_\pi - \sqrt{E_\pi^2 - m_\pi^2} \cos \theta)} \quad (2.2)$$

where E_π is the energy of the parent pion and θ is the scattering angle between the direction of the outgoing neutrino and the direction of the parent pion's momentum, m_{pi} is the parent pion mass and m_μ is the mass of the outgoing muon. Figure 2.7 shows the neutrino energy from pion decay plotted against the energy of the parent pion for a range of off-axis angles.

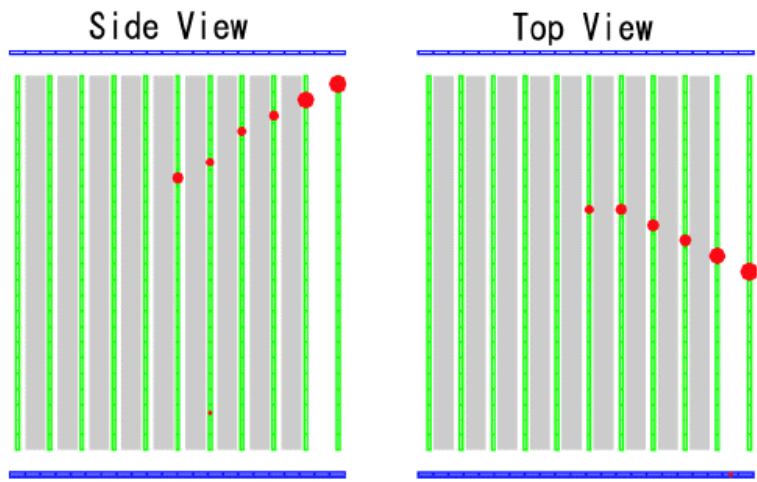


Figure 2.5: INGRID event display showing a typical INGRID event, taken from [3].

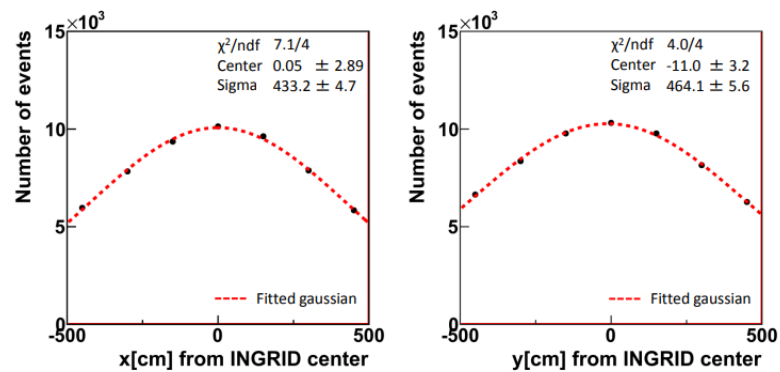


Figure 2.6: Neutrino beam profiles for x (left) and y (right) directions.

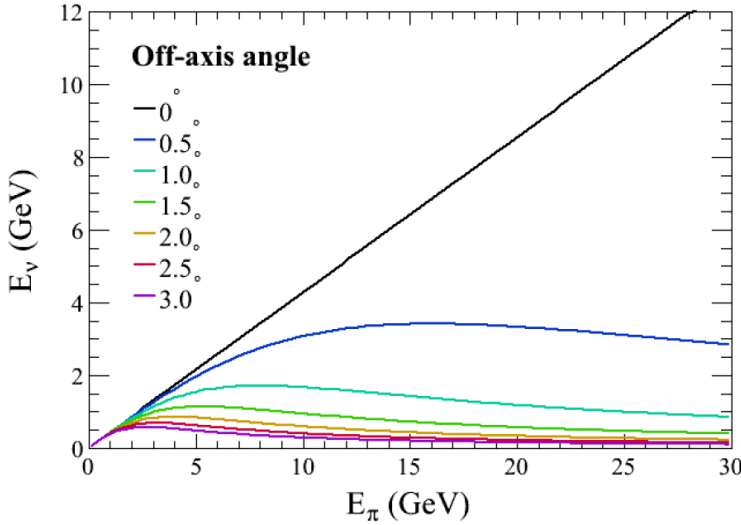


Figure 2.7: Energy of the neutrino plotted against the energy of the parent pion for multiple different off-axis angles

As off-axis angle increases, the intensity of the neutrino beam decreases, and therefore picking an off-axis angle of 2.5° at which to place the ND280 detector complex strikes a good balance between keeping a high beam intensity while ensuring a peak energy of 0.6 GeV in order to have the neutrino oscillation be maximised at 295km. The relationship between muon neutrino oscillation probability and muon neutrino energy is shown at the top in Figure 2.8, and at the bottom the muon neutrino flux 295 km away from the graphite target can be seen for three different off-axis angles.

Figure 2.9 shows a schematic of the ND280 detector complex. It has five main goals: firstly, to measure the cross sections of muon neutrino interactions, so neutrino-nucleus interaction models can reduce their systematic uncertainties. Secondly, measuring the component of the neutrino beam which is made of electron neutrinos, hence being able to better constrain the background to electron neutrino appearance at the far detector. Thirdly, to predict the event rate at Super-Kamiokande by measuring the energy spectrum of the muon neutrinos produced. It also aims to study non quasi-elastic processes which produce pions below the Super Kamiokande Cherenkov threshold, and to measure the neutral current (NC) pion-nought production rates.

N2D280 is made of a neutral pion detector (*P0D*), three Time Projection Chambers

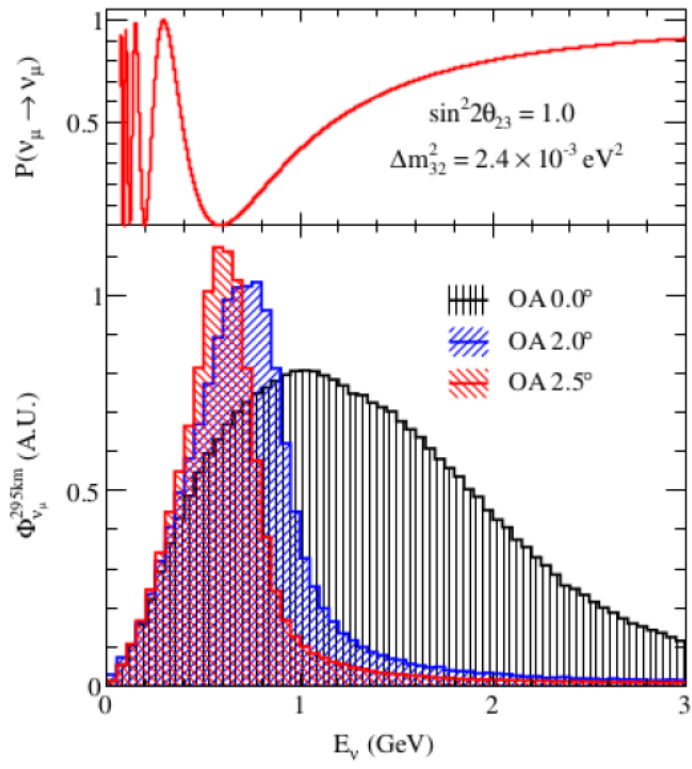


Figure 2.8: The probability of survival of muon neutrinos (top plot) and neutrino beam flux at the 295km far detector (bottom) Taken from [4].

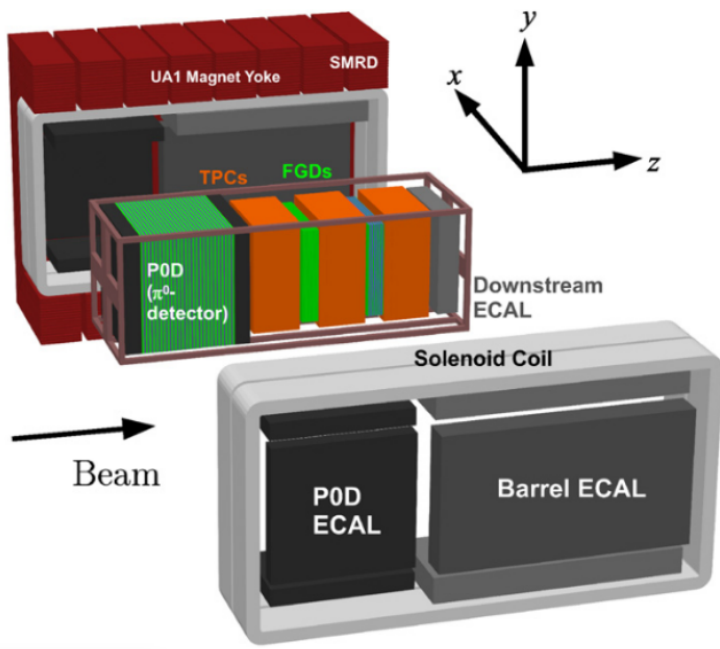


Figure 2.9: Near detector ND280 schematic taken from [3].

(TPCs) and two Fine Grained Detectors (FGDs). These are enclosed within Electromagnetic Calorimeters (ECals) and a Side Muon Range Detector (SMRD). These detectors are magnetised using a magnet originally used in the UA1 detector at CERN.

The neutral pion detector is important due to its ability to detect a process that can imitate the signal event of electron neutrino appearance at Super-Kamiokande. Neutral pions are produced during the neutral current interactions on water ($\nu_\mu + N \rightarrow \nu_\mu + N' + \pi^0 + X$) and the purpose of *P0D* is to measure the cross-section of this interaction.

There are also two electromagnetic calorimeters which remove events entering the detector from the outside. The SMRD (Side Muon Range Detector) is used as a way to measure the momenta of muons which escape the detector complex at a large angle relative to the direction of the beam.

There are three time projection chambers placed downstream of the neutral pion detector. These are used for reconstruction of charged particle tracks, particle identification and determination of the momentum of the particle. There are two fine grained detectors (FGDs) in ND280, which have two purposes. Firstly to yield a mass for the neutrino interaction, and secondly, to track the charged particles issuing from the neutrino interaction vertex. The ECal is an electromagnetic calorimeter which surrounds the P0D, the TPCs and the FGDs. It consists of plastic scintillator layers sandwiched between lead absorber sheets. Its purpose is to aid in the full event reconstruction through detecting photons and measuring their energy and direction, along with detecting charged particles and getting information which helps in their identification (separating out electrons, muons and pions.)

Chapter 3

The Super Kamiokande Detector

3.1 The Super-Kamiokande detector

3.1.1 Background and detector design

Super-Kamiokande is a neutrino observatory consisting of a cylindrical tank which is 41.4 m in height and 39.3 m in diameter, and filled with 50kton of ultrapure water and currently with 0.026% gadolinium sulphate. It is used as a neutrino detector for atmospheric, solar and astrophysical neutrinos, as well as being a far detector of the T2K neutrino beam. It is based in the Mozumi mine, located in Gifu Prefecture, Japan. Due to its location being underneath Mount Ikenoyama, 1000m underground, it is shielded from the cosmic ray muon detector background. Super-Kamiokande is divided into two concentric cylinder volumes, consisting of the inner detector (ID) and outer detector (OD) using a stainless steel structure which supports the photomultiplier tubes. Tyvek and black polyethylene terephthalate sheets are mounted on this structure in order to optically separate the inner and outer detector [33].

The inner detector is a cylinder which has a diameter of 33.8 m and a height of 36.2m, and has a fiducial volume of 22.5 ktons of water. The fiducial volume is defined as the region inside a surface drawn 2.00 m from the inner detector wall. Using this fiducial volume gives protection against events produced from natural radioactivity in the surrounding rock. The detector contains 11,129 photomultiplier tubes which give 40% photocoverage of its inner surface, with the specific photomultiplier model chosen being the hemispherical, 50.8 cm diameter Hamamatsu R3600 model. The 2 m wide outer detector has only 1885

photomultiplier tubes which are mounted on the outside of stainless steel structure, each with a smaller diameter of 20cm, and are either the R1408 or R5912 Hamamatsu model. Each outer detector photomultiplier tube is attached to a 50cm x 50cm wavelength shifting plate, improving the light collection ability in the OD [20].

A detailed schematic of the photomultiplier tubes used in Super-Kamiokande can be seen in Figure 3.1. The photocathodes used in these PMTs are comprised of bialkali antimony-potassium-caesium material (Sb-K-Cs), which give a greater sensitivity to longer wavelengths, giving the greatest spectral response at 360 nm, near the ultraviolet range. This makes these types of photocathodes suitable to use for matching with light sources in the blue region of the visible spectrum, which is the region in which the wavelength of Cherenkov photons lie. The 11 dynodes which are inside the photomultiplier tube are arranged in a “venetian blind” fashion, meaning that the dynodes consist of an assembly of parallel strips. This results in a good collection efficiency of the multiplied electrons and gives decent protection from external magnetic fields. More protection from external magnetic fields is provided by a set of Helmholtz coils which are aligned outside the inner detector, which reduce the ambient background geomagnetic field from 450mG to 50mG. This is needed due to the systematic bias that could occur due to the strength and uniform direction of this magnetic field affecting the photo-electron trajectories and consequently the photomultiplier tube hit timing.

Radioactivity from radon, uranium and thorium radioisotopes in the Super-Kamiokande tank water and radon in the surrounding air could provide a low energy background to measurements which should be negated. In low-energy analyses, such as the analysis in this thesis, this becomes an even more significant issue. Microbes present in the mine water also present a problem as they cause a reduction in the the light attenuation length. Therefore the water used in Super-Kamiokande has to undergo a purification process - the water used is continuously reprocessed at a rate of 30 tons h^{-1} in a closed loop system, which is the same method used to purify the water when refilling the tank. The first step of this water purification process is to use a 1 μm mesh filter to remove large particulates of impurities from the water [19]. A heat exchanger is then used to cool down the water to a constant 13.0 °C to reduce the dark noise hits of the photomultiplier tubes and the growth of the microbes. A treatment with ultraviolet light is then used to kill any remaining microbes in the water. Radon-free air is then dissolved into the water to aid in the later process of radon removal from the water and a high performance membrane ultra filter (UF) is used to remove organic compounds about 10 nm in diameter from the

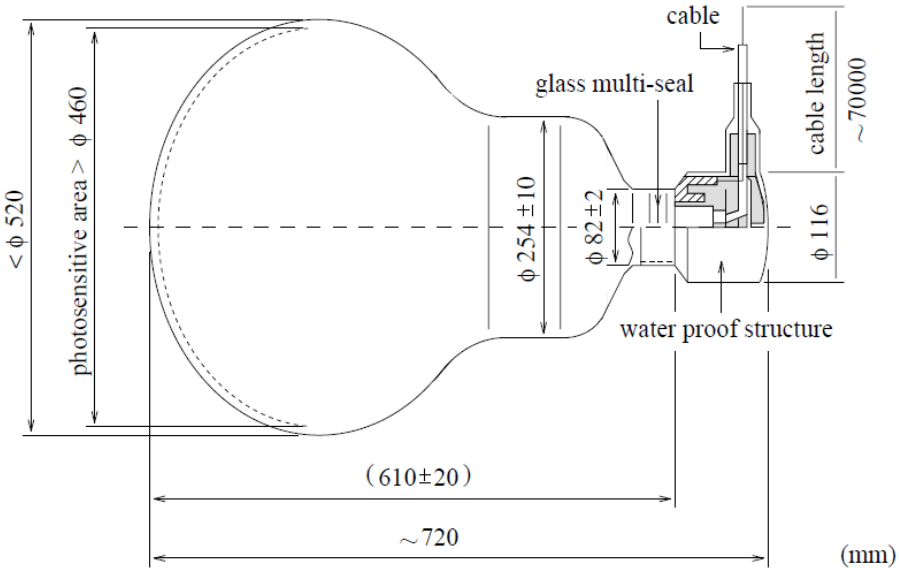


Figure 3.1: Schematic of an ID 50 cm Super-Kamiokande PMT [20].

water. After this step a membrane degasifier removes the dissolved radon, where 30 L of radon reduced air is supplied to the membrane degasifier. The dissolved radon will transfer across the membrane but the water will not, allowing for efficient radon reduction.

The inner detector tank water is circulated by injecting the water at the bottom of the tank and extracting it from the top, where the convection currents are able to maintain the temperature in the region within 11 m to the bottom of tank, however, outside this region the present temperature gradient causes an asymmetry in the attenuation of light, which is discussed more in Chapter 3.

An air purification system is also installed in Super-Kamiokande in order to reduce the amount of Radon present which could dissolve into the tank and affect measurements. The level of radon activity achieved after this air purification has taken place is $1 \text{ mBq}/\text{m}^3$.

The Super-Kamiokande experiment began taking data on 1st April 1996, and due to maintenance was shut down in July 2001, which was phase I of the experiment. A table of the Super-Kamiokande phases is shown in Table 3.1. During the refilling of the tank after maintenance, there was cascade of PMT implosions that occurred on the 12th of November 2001, which were triggered by the implosion of a single photomultiplier tube,

due to a microfracture in the neck of the tube. This implosion destroyed about 7,000 of the PMTs and in order to avoid such chain reactions in the future, from 2002 onwards all of the inner detector PMTs are fitted with acrylic covers and fiber-glass reinforced plastic (FRP) cases. Detector shutdown and rebuild took nine months and Super-Kamiokande resumed data taking with the full number of photomultiplier tubes in July 2006 which marked the beginning of Super-Kamiokande phase III. Super-Kamiokande phase IV began in September 2008 where a new data acquisition system and charge to time (QTC) based electronics with Ethernet (QBEE) was deployed in order to measure arrival times and integrated charge for inner detector and outer detector photomultiplier tube signals. This replaced the ATM (Analogue and Timing Module). The improvements in electronics and calibration methods meant that when Super-Kamiokande phase IV started running in September of 2008, electrons with energies as low as 3.5 MeV were able to be detected.

Phase	Phase Period	Total PMT number		FRP case?	Readout	Gd%
		ID (Coverage)	OD			
SK-I	Apr. 1996 - Jul. 2001	11146(40%)	1884	no	ATM	0
SK-II	Oct. 2002 - Oct. 2005	5182(19%)	1884	yes	ATM	0
SK-III	Jul. 2006 - Sep. 2008	11129(40%)	1884	yes	ATM	0
SK-IV	Sep. 2008 - May 2018	11129(40%)	1884	yes	QBEE	0
SK-V	Jan. 2019 - Jul. 2020	11129(40%)	1884	yes	QBEE	0
SK-VI	Aug. 2020 - May 2022	11129(40%)	1884	yes	QBEE	0.01%
SK-VII	Jun. 2022 - Today	11129(40%)	1884	yes	QBEE	0.03%

Table 3.1: Phases of Super-Kamiokande and main properties of each phase

3.1.2 Data aquisition system

As shown in Table 3.1, Phase IV of the experiment marked the beginning of Super-Kamiokande using QTC-based Electronics with Ethernet (QBEEs). Each QBEE board used in Super-Kamiokande contains 24 photomultiplier tube input channel, where each channel uses a charge-to-time (QTC) converter and a time-to-digital converter placed in series as shown in Figure 3.2. After a single photoelectron is produced by the photomultiplier tubes after incident photons have been received upon it, the dynodes inside the photomultiplier tube amplify this photoelectron so that each photoelectron that strikes the

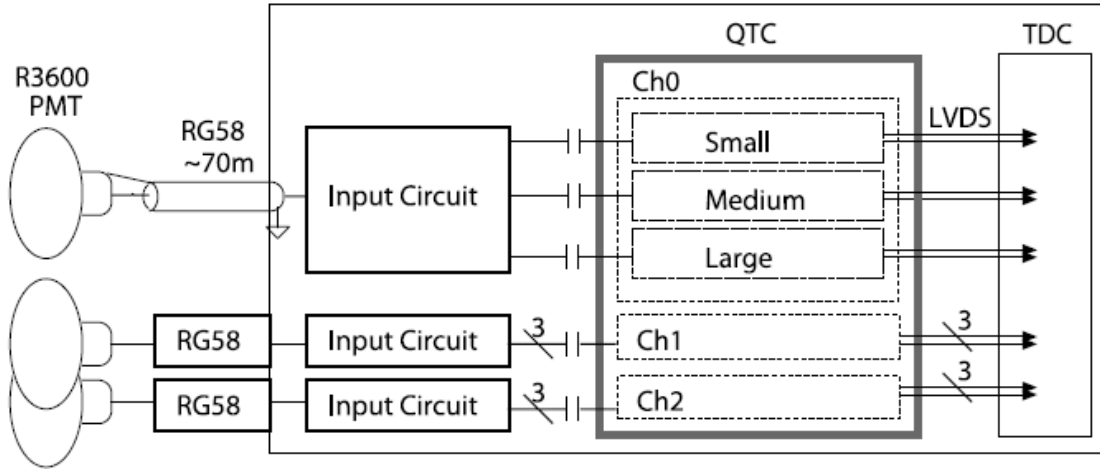


Figure 3.2: Schematic of the charge-to-time converter circuit [30].

surface of the dynode produces several more photoelectrons, which are produced from the dynodes as an analogue signal. This signal then enters a charge-to-time converter (QTC), an application specific integrated circuit (ASIC) which was specifically designed for Super-Kamiokande in order to detect photomultiplier tube signals using built-in discriminators and to produce output timing signals whose widths represent the integrated charge of the PMT signal. The QTC used has three input channels per chip, which has three gain ranges (Small, Medium, Large as shown in Figure 3.2). There is a built in discriminator inside the QTC which determines whether the the signal from a PMT is a “hit”. If the PMT signal exceeds the threshold value of this discriminator, the QTC integrates the charge of the signal over the next 400 ns, and a square wave pulse is generated whose pulse width is proportional to the intergrated charge of the input signal from the PMT. The next 400 ns is used to discharge the integrated charge from the QTC, leading to a total channel dead time of 900 ns due to summing the charge integration and discharge of the QTC.

A time-to-digital converter (TDC) then digitises the output time signal, so the PMT charge information is retained. These digitised outputs are collated by 20 front-end computers which collects all the information from the inner and outer detectors, with each computer taking the PMT hit information from 30 inner detector and 20 outer detector QBEE boards and sorting the PMT hit time information in order of the raw hit time. This

information is then sent to “merger” computers, who then produce a full time-ordered list of all PMT hits. These merger computers then apply software triggers to select event candidates, using N_{200} , a quantity which determines the number of PMT hits in a 200 ns timing window. When the value of N_{200} surpasses the threshold value of a certain trigger type (whether it is a SLE (Super Low Energy), LE (Low Energy), HE (High Energy), SHE (Super High Energy), OD (Outer Detector) or AFT (After Window) trigger), the trigger is used to select an event candidate. The SLE, LE, HE and SHE triggers roughly define the energy of a certain event, based on the number of hits detected. The OD trigger is used to veto events, and the AFT trigger is of special importance to the analysis in this thesis: it is used to discern when a neutron is produced after a neutrino interaction. The AFT Trigger is issued to take 500 μ sec of data after SHE trigger in order to identify the positron from the prompt event and the delayed 2.2 MeV gamma released from the neutron capture on the proton during the IBD reaction. Another set of computers acts as an “organiser”: it takes all the information regarding the event candidates from the “merger” computers and writes them onto disks [20].

3.2 Event Reconstruction

3.2.1 Vertex Reconstruction

For low energy events (events up to 100 MeV), Super-Kamiokande currently uses BONSAI (Branch Optimisation Navigating Successive Annealing Interactions) for event reconstruction. Vertex reconstruction for Super-Kamiokande has undergone changes and improvements depending on the phase of the experiment.

For Phase I of Super-Kamiokande, vertex reconstruction depended on a lattice of test vertices with 4 m spacing throughout the detector, with a specific measure of goodness for each test vertex: the test vertex with the highest measure of goodness would have around it a more finely spaced grid, and the process would be repeated. For Phase II of Super-Kamiokande due to the reduced number of PMTs, this approach was no longer as successful as it was in Phase I and as a result the reconstruction performance declined, and BONSAI was created as a replacement. Instead of using a fixed grid which was the case with SK-I and SK-II, BONSAI creates test vertices by selecting groups of four PMT hits and seeing where the timing residuals of the PMT hits would be most reduced. After these test vertices have been identified, a maximum likelihood fit over all the PMT hits in the

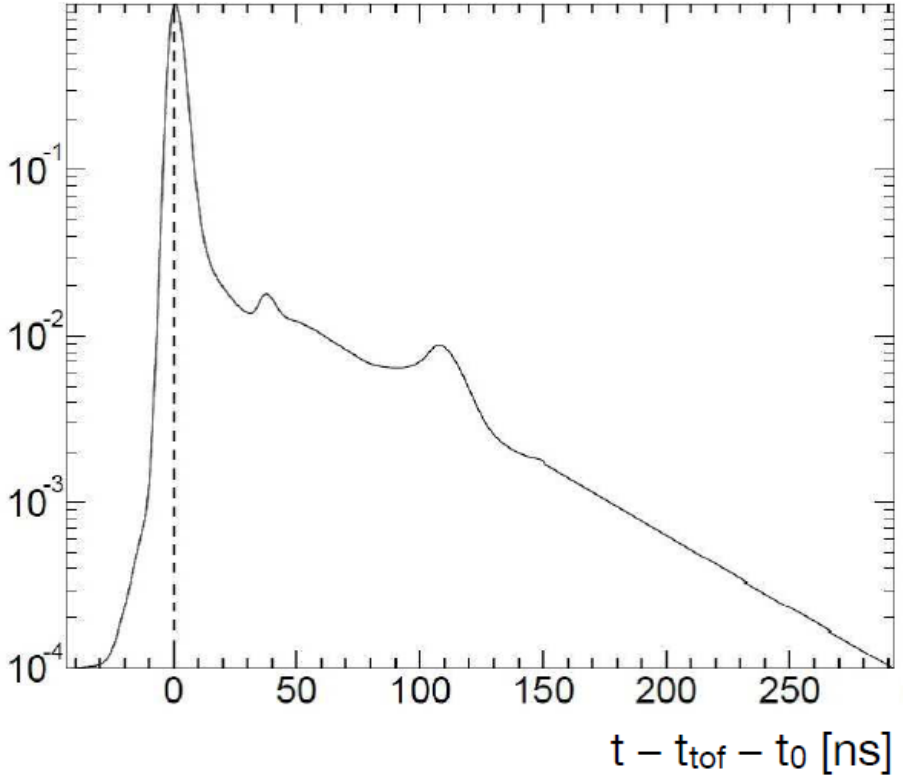


Figure 3.3: Probability density of the timing residual $P(t - t_{\text{tof}} - t_0)$, where t_0 is used for the vertex reconstruction maximum likelihood fit. The peaks at 30ns and 100ns are caused by PMT after-pulsing.

event is performed, shown in Equation 3.1.

$$\mathcal{L}(\vec{x}, t_0) = \sum_{i=1}^{N_{\text{hlt}}} \log(P(t - t_{\text{tof}} - t_0)) \quad (3.1)$$

where (\vec{x}, t_0) is the test vertex, and $(P(t - t_{\text{tof}} - t_0))$ (shown in Figure 3.3) is the probability density function of the timing residual, which for each PMT hit is defined as $(t - t_{\text{tof}} - t_0)$, where t_0 is the time of the interaction, t_{tof} is the time of flight from the interaction vertex position to the position of the hit PMT, t is the PMT hit time. The 1σ difference between the true vertex position and the reconstructed vertex position plotted as a function of true electron energy is shown in Figure 3.4.

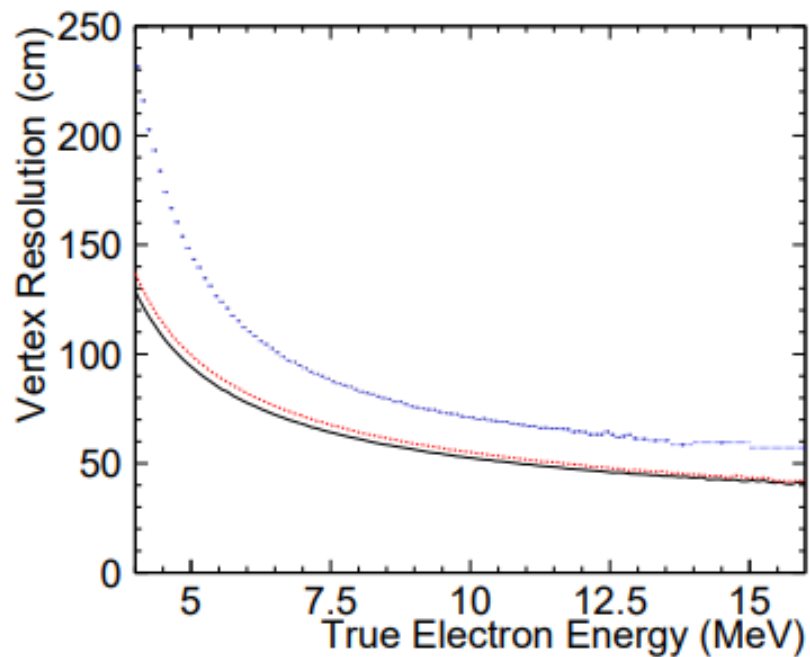


Figure 3.4: The vertex resolution (the point at which 68% of the events in the distance distribution between the actual and reconstructed vertex are contained) for the different SK phases. SK-I (Blue), SK-III (Red), SK-IV (Black).

3.2.2 Direction Reconstruction

Cherenkov light is emitted in a conical formation as electrons and positrons travel through water, with a Cherenkov angle of $\approx 42^\circ$. BONSAI can reconstruct the direction of these particles by using this information along with the reconstructed vertex. This reconstruction occurs using a maximum likelihood function defined in Equation 3.2.

$$\mathcal{L}(\vec{d}) = \sum_i^{N_{20}} \log(f(\cos \theta_i, E)) \times \frac{\cos \theta_i}{a(\theta_i)} \quad (3.2)$$

The term $f(\cos \theta_i, E)$ in Equation 3.2 is the expected distribution of the angle between the vector of the direction \vec{d} of the particle, and the observed Cherenkov photon from the position of the reconstructed vertex. The reason there is a spread in this energy distribution is because while the highest value of this distribution occurs at the cosine of the opening Cherenkov angle of 42° , due to the particle travelling through the water being Coulomb scattered multiple times, there is a variation in the angle because of the varying particle energy. The term N_{20} is the number of hits whose residual hit time is within 20 ns of the time of the reconstructed event, which is used in order to reduce the amount dark noise and scattered photons contribute to the direction reconstruction calculation. The variable $a(\theta_i)$ is a correction factor stemming from the acceptance of PMTs and therefore linked to the shape of the PMT and its acrylic case, is linked to the angle of incidence of the photon on the PMT, and is related to the angle of incidence of the photon on the PMT.

3.2.3 Energy reconstruction

The kinetic energy of a particle is proportional to the amount of Cherenkov photons emitted from it, and if we assume that the Cherenkov photons in a single event come from a single electron, we can reconstruct the total energy of the electron. Instead of using the number of photoelectrons of all hit photomultiplier tubes to reconstruct the energy of low energy events, the number of hit photomultiplier tubes is used instead. The reasons for this are threefold - firstly, low energy events emit a small number of Cherenkov photons, and therefore average about one photon per hit PMT. Secondly, at single photoelectron level, the resolution of the PMTs is poor, and third, the number of photoelectrons produced is related to the gain of the PMT.

Due to the variation in gain value not affecting the number of hit photomultiplier tubes as much as it does for the number of photoelectrons, number of hit PMTs is used instead.

To reduce dark noise, energy reconstruction uses N_{50} , which is the number of time of flight corrected photomultiplier tube hits in a 50 ns window. The number of effective photomultiplier tubes which are hit in this timing window of 50 ns are summed up, while being weighted with correction factors, to give N_{eff} shown in Equation 3.3 [34].

$$N_{eff} = \sum_{i=1}^{N_{50}} \left[(X_i - \epsilon_{dark} + \epsilon_{tail}) \times \frac{N_{all}}{N_{alive}} \times \frac{1}{S(\theta_i, \phi_i)} \times \exp\left(\frac{r_i}{\lambda}\right) \times G(i) \right] \quad (3.3)$$

where X_i is the correction factor hits with many photoelectrons. This correction factor is important because if some photomultiplier tubes are hit by multiple photons (for example, if the edge of the fiducial volume is where the event vertex took place). The number of photoelectrons produced by each hit photomultiplier tube is estimated using the occupancy of the eight photomultiplier tubes which surround it. Using the number of hit photomultiplier tubes (n_i) and the number of functional photomultiplier tubes that surround the i-th photomultiplier tube (N_i), the formula for X_i is shown in Equation 3.4.

$$X_i = \begin{cases} \log(1 - n_i/N_i)^{-N_i/n_i} & (n_i < N_i) \\ 3 & (n_i = N_i) \end{cases} \quad (3.4)$$

The term ϵ_{dark} in Equation 3.4 is a correction factor for dark noise hits, shown in Equation 3.5, where R_{dark} is the average value for the dark rate during the run period that the event is in and $N_{PMTalive}$ is the number of active photomultiplier tubes in the inner detector.

$$\epsilon_{dark} = \frac{N_{PMTalive} \times R_{dark} \times 50 \text{ ns}}{N_{50}} \quad (3.5)$$

The term ϵ_{tail} is the correction factor for photomultiplier tube hits which are in the tail end of the 50ns timing window, and is defined in Equation 3.6.

$$\epsilon_{tail} = \frac{N_{100} - N_{50} - N_{alive} \times R_{dark} \times (100 - 50)\text{ns}}{N_{50}} \quad (3.6)$$

The term $\frac{1}{S(\theta_i, \phi_i)}$ is the inverse of the effective area of the ith hit photomultiplier tube photocathode, from the direction of the incident photon given by it's solid angle (θ_i, ϕ_i) .

$G(i)$ is the gain correction for the quantum efficiency of the photomultiplier tubes and $\exp(\frac{r_s}{\lambda})$ is the correction for water transparency which accounts for the amount of attenua-

tion undergone by the photons in water, where λ is the water transparency measured during the run period which includes the event, and r_i is the distance between the reconstructed event vertex and the i-th hit PMT.

The average of each N_{eff} distribution is taken, after producing multiple N_{eff} distributions with fixed energies using Monte Carlo. These energies are fitted with a polynomial which is a function of the averaged N_{eff} distribution, so the reconstructed energy is converted from N_{eff} .

To summarise, Super-Kamiokande has undergone a lot of transformations over its lifetime, with modifications made to its data acquisition system and methods of event reconstruction with each successive new phase. The biggest change made to the detector is the upgrade to Super-Kamiokande Gd, where in the summer of 2020 0.02% of gadolinium sulphate was added to the detector: a long-awaited next step which would enhance sensitivity to the detection of neutrons emitted in inverse beta decay compared to that in water, something discussed in much more detail in Chapter 6.

Chapter 4

Super-Kamiokande Detector Calibration

In order to achieve optimal event reconstruction for physics analyses, calibration of the Super-Kamiokande detector is crucial. For example, when conducting Monte Carlo simulations of certain processes in the detector, facets of the experiment such as properties of the water, photomultiplier tube response and the inner detector and outer detector electronics are all calibrated so that input parameters for the Monte Carlo simulations can be obtained. This chapter will concern itself with the inner and outer detector calibration, including photomultiplier tube and electronics calibration, PMT gain calibration, quantum efficiency determination and hit timing and charge information calibration.

4.1 Inner detector calibration

4.1.1 PMT High-voltage setting calibration

The high-voltage (HV) setting for all photomultiplier tubes need to be adjusted individually so all the PMTs produce the same amount of charge for a certain light intensity received by them. Placing a light source which distributes light isotropically in the centre of the inner detector to achieve this calibration means that there is no position in the detector from which the inner detector PMTs are equidistant, so each PMT will not receive the same amount of light from the light source. To avoid this problem, a set of 420 pre-calibrated PMTs inside the detector were used, separated into groups relating to their geometrical

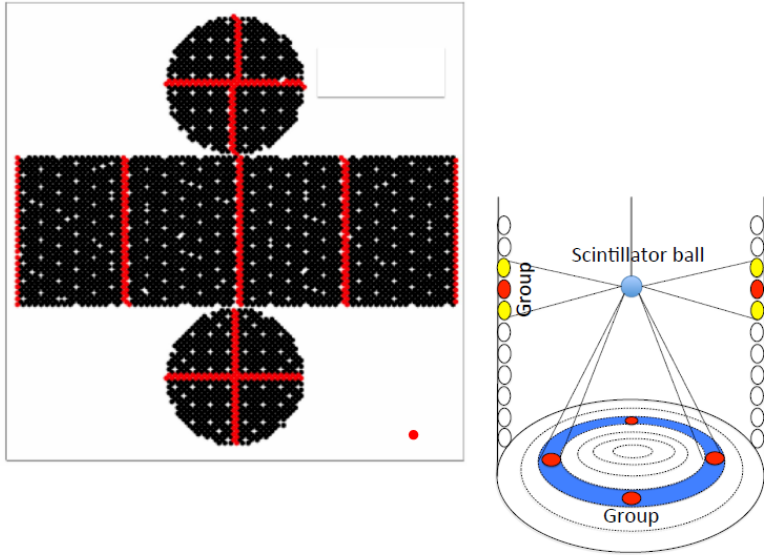


Figure 4.1: Location of 420 reference PMTs used for HV setting calibration. The red lines in show the placement of these PMTs with respect to the others (left). The grouping of these PMTs due to their geometry in relation to the light source is also shown (right)

distance from the HV calibration light source, which is shown in Figure 4.1 for their location with respect to the other photomultiplier tubes.

4.1.2 Relative gain calibration

Understanding the timing information from the hit photomultiplier tubes depends on how well the charge from the hit PMT is calculated. To conceive charge calibration, a quantity called photomultiplier tube “gain” must be calculated. “Gain” is the conversion factor from the number of photoelectrons produced by the hit PMT and charge, specifically how much charge one can expect from a single phtotoelectron from the PMT anode. Along with the PMT gain, there are three other quantities which relate to charge calibration: quantum efficiency, collection efficiency and light collection efficiency.

The quantum efficiency (QE) is the ratio of the number of photoelectrons produced by the photocathode, to the number of incident photons on the photocathode. The collection efficiency is the fraction of the total number pf photoelectrons produced which are collected by the first dynode in the PMT. The product of the quantum efficiency and the collection

efficiency, gives the light collection efficiency.

Knowing the gain and light collection efficiency of each PMT in the detector is important in order to accurately measure the output charge from each individual PMT, which is done by first calculating the relative gain difference among all PMTs and then working out the average gain difference over all PMTs in the detector. After this, the variation away from this average gain value can be calculated for each separate inner detector photomultiplier tube, and the gain value for each can be extracted.

The relative gain difference is calculated by two measurements using a light source to produce constant-intensity flashes. The first measurement involves using the light source to produce high-intensity flashes so that all photomultiplier tubes in the detector get a certain number of photons, and the second measurement has the light source produce low-intensity flashes so that only a few PMTs are hit. The first measurement provides an average charge value ($Q_{obs}(i)$) for each inner detector PMT, while the second measurement gives single photoelectron hits, providing a number of times ($N_{obs}(i)$) that a single PMT gives a charge which is greater than the PMT threshold value. Equations 4.1 and 4.2 shows how these two values are calculated from the high and low intensity flash values (I), the acceptance of the PMT(i) ($a(i)$), the QE value of the PMT (ε_{qe}) and the PMT gain G .

$$Q_{obs}(i) \propto I_{high} \times a(i) \times \varepsilon_{qe}(i) \times G(i) \quad (4.1)$$

$$N_{obs}(i) \propto I_{low} \times a(i) \times \varepsilon_{qe}(i) \quad (4.2)$$

Therefore, by simply dividing these two values of $Q_{obs}(i)$ and ($N_{obs}(i)$) the average gain over all PMTs can be calculated. Figure 4.2 shows the spread of the relative gain over all the PMTs.

4.1.3 Absolute gain calibration

In order to calculate absolute gain, the single photoelectron distribution needs to be measured, this is because absolute gain relates to the observed charge in the photomultiplier tube with the number of photoelectrons produced. A nickel-californium source (shown in Figure 4.3) is used for this measurement due to it releasing gamma rays isotropically, with a total gamma ray cascade energy of 9 MeV. Thermal neutron capture on nickel is used as the gamma ray source, with the neutrons provided by the spontaneous fission of

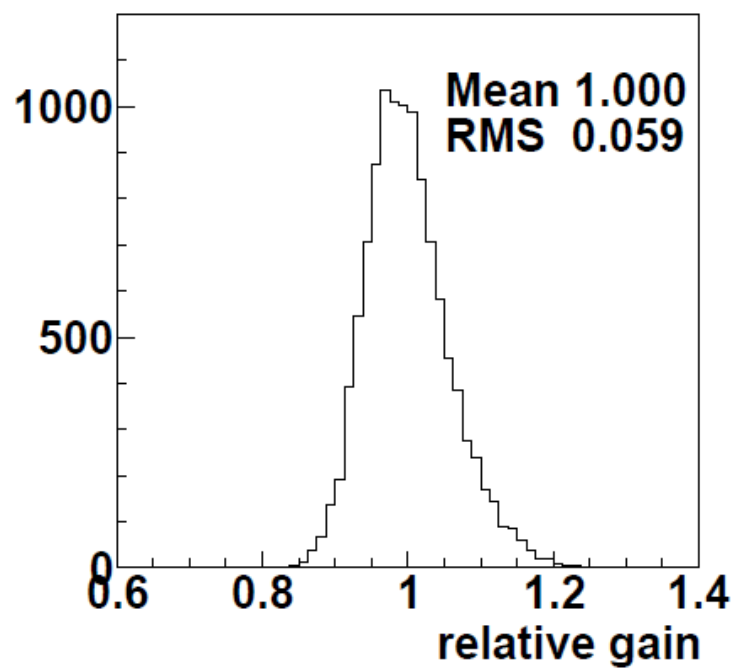


Figure 4.2: Relative gain of PMTs in Super-Kamiokande



Figure 4.3: Nickel-californium source used for absolute gain calibration [5]

^{252}Cf . This nickel source is placed in the centre of the inner detector and the gamma rays produced are detected by all the inner detector PMTs. On average the observed number of photoelectrons is 0.004 per event per PMT, meaning that single p.e. hits are observed for more than 99% of the hits. The observed charge distribution of all the hits from this nickel source is used to give the average charge, which is used as a conversion factor from a charge measurement in picoColoumbs and single photo-electrons. The factor is 2.658 pC per photoelectron (calculated at the beginning of SK-IV) which is then used to extract the single-p.e. distribution, shown in Figure 4.4.

4.1.4 Relative quantum efficiency measurement

To measure the relative quantum efficiency, the gamma rays from neutron capture on the nickel source are simulated. Inside this simulation, a common value of QE is used for all the ID PMTs to predict the number of hits for each PMT. Comparing this number of hits to the actual data obtained for each individual PMT by calculating the ratio between them provides us with a value for relative QE for each inner detector PMT which is then used

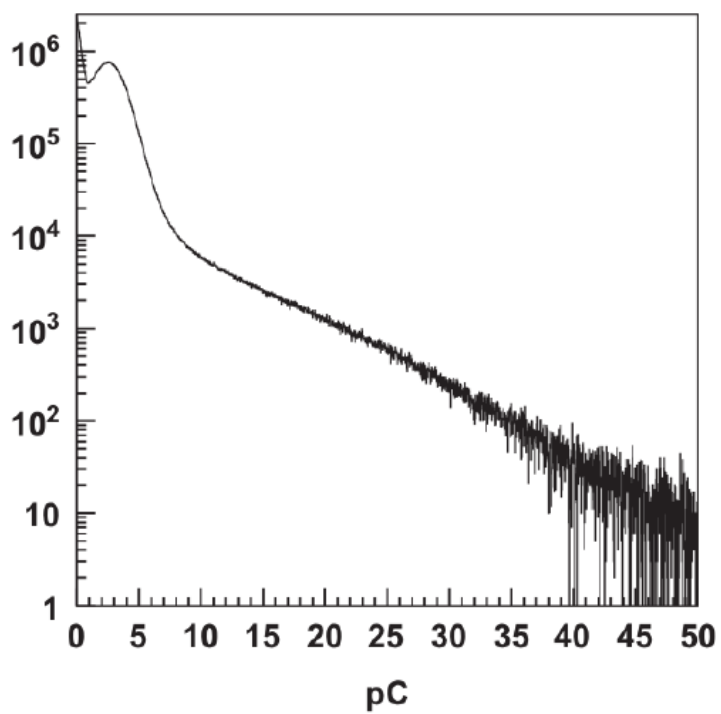


Figure 4.4: Single p.e distribution of charge in pC [5]

inside the simulation.

4.1.5 Timing information calibration

Calibrating the hit timing information of the photomultiplier tubes is essential due to its importance in accurately being able to reconstruct events. Event reconstruction makes use of determining exactly where interaction vertices are and the direction in which particles travel, and to do this the time response needs to be very carefully calibrated. The response time of the PMT also relates to the amount of charge observed: in order for a hit to be registered, the PMT signal must pass the discriminator value of the hit threshold, and the time in which this happens is dependent on the height of the pulse, which is correlated with the observed charge. All these factors need to be considered when calibrating hit timing information.

To aid the timing calibration, a diffuser ball is placed near the centre of the inner detector, into which a nitrogen laser injects pulsed laser light. By varying the intensity of this light, the laser light can be outputted in flashes, and the timing of the laser pulses is monitored using a 2-inch monitor PMT. The schematic of this timing calibration system is shown in Figure 4.5.

The value of these laser pulse timings, and the time-of-flight value from the diffuser ball are subtracted from the PMT hit time. Using the observed charge values and these adjusted hit times, “TQ” (time and charge) distributions can be plotted for each inner detector PMT. An example TQ distribution is shown for an inner detector PMT (cable number 00010) in Figure 4.6, where the vertical axis shows the corrected TOF and laser pulse time corrected PMT hit time, and the horizontal axis shows the observed charge of each hit. Figure taken from [5].

The timing resolution of the PMTs (also known as the transit time spread) is also something that must be calibrated. This is calculated by using the same timing and charge data used to produce the TQ distributions. By correcting all the ID PMT hits by their TQ distributions, these residual timing distributions have an asymmetric Gaussian function fitted to them, from which two values of sigma are extracted: σ_t and $\sigma_{t'}$. These are the values for the timing resolution for before and after the peak time of this distribution. Equation 4.4 shows how the asymmetric Gaussian is defined.

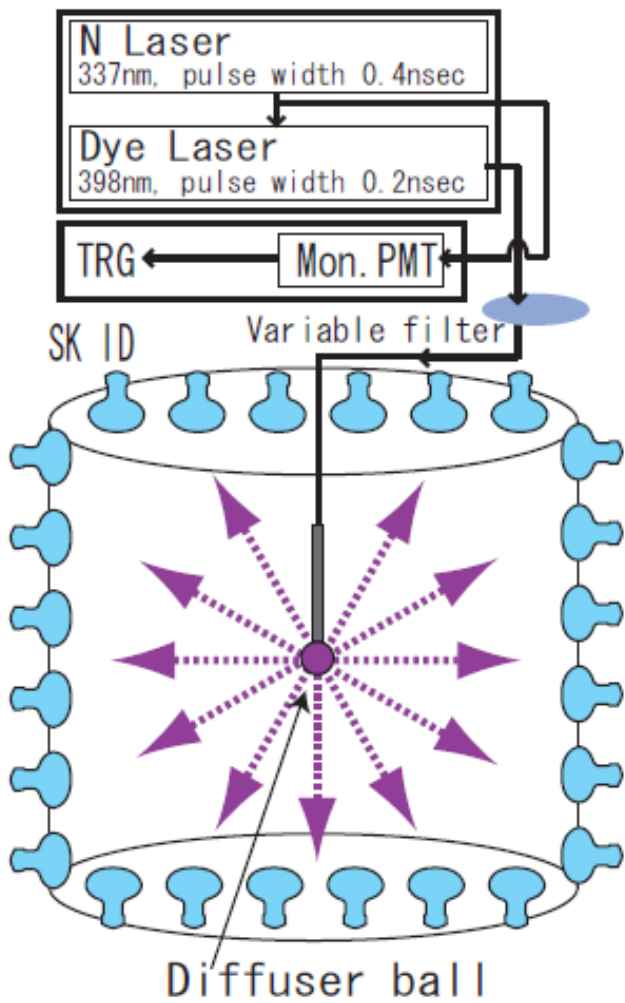


Figure 4.5: Schematic of the timing calibration system, with SK ID PMTs in blue and the diffuser ball in purple. The dye laser shifts the wavelength of the laser light to 398 nm to maximise the quantum efficiency of the PMTs and light absorption.

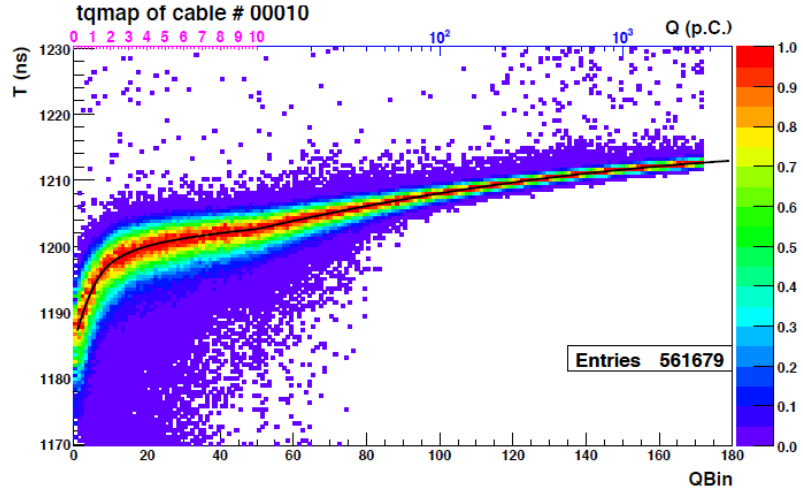


Figure 4.6: Example TQ distribution for an inner detector PMT

$$f(t; t > T_{\text{peak}}) \equiv A_1 \cdot \exp\left(-(t - T_{\text{peak}})^2 / \sigma_t^2\right) + B_1 \quad (4.3)$$

$$f(t; t \leq T_{\text{peak}}) \equiv A_2 \cdot \exp\left(-(t - T_{\text{peak}})^2 / \sigma_t'^2\right) + B_2 \quad (4.4)$$

Figure 4.7 shows an example of the residual timing distribution fitted with an asymmetric gaussian for a certain value of binned charge.

Figure 4.8 shows timing resolution plotted as a function of charge for both before and after the peak time of the residual time distribution (red and blue points respectively) for SK-IV TQ calibration data.

4.1.6 Measurement of light reflection on the black sheet and the PMTs

For SK-IV, four types of material, corresponding to four different refractive indices are taken into account: water, glass, bialkali, and vacuum. Table 4.1 shows the values for each of these materials, λ is the wavelength of the light in nm and n_{real} and n_{img} are the real and imaginary parts of the complex refractive index.

Regarding the black sheet used to line the inside of Super-Kamiokande, it can either reflect or absorb Cherenkov photons. The amount of Cherenkov photons detected is measured by a light injector setup, shown in Figure 4.9. For three different incident angles of

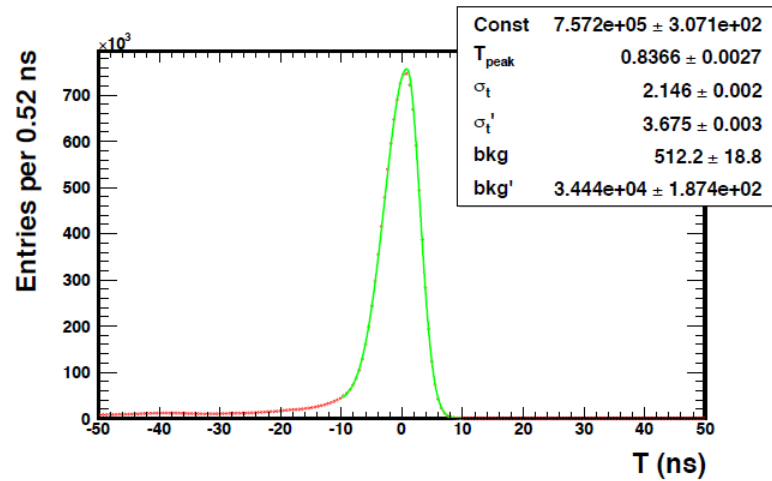


Figure 4.7: Residual timing distribution summed over all the readout channels in charge bin 14 (QBin in 4.6.)

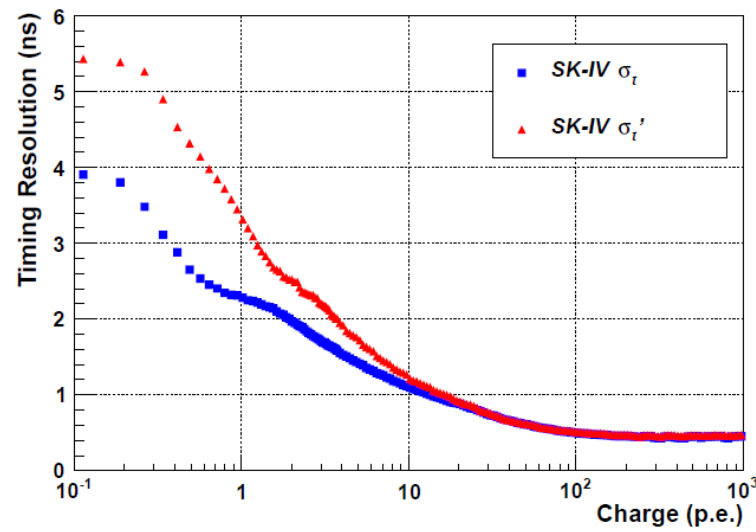


Figure 4.8: Timing resolution as a function of charge for SK-IV

laser light (30° , 45° and 60°) and three different laser light wavelengths (337 nm, 400 nm and 420 nm) the charge from the light scattered off the black sheet was measured. The direct charge (i.e. the same setup without the black sheet present) was also measured, with the total black sheet reflectivity being the ratio between the scattered charge and the direct charge.

Material	Refractive index
Water	1.33
Glass	$1.472 + 3670/\lambda^2$
Bi – alkali	$n_{real} + i n_{img}$
Vacuum	1.00
x_{abs}^N	Nucleon absorption probability
x_π^N	Nucleon π -production probability

Table 4.1: Refractive indices of materials inside the Super-K detector.

Measurement of absorption and scattering coefficients

In Super-Kamiokande, the detector medium scatters and absorbs the Cherenkov light, attenuating its wavelength. The amount of light attenuation after the light has travelled distance l is given by $\exp(-l/L(\lambda))$. Here $L(\lambda)$ is the attenuation length of the detector medium and is shown by Equation 4.5,

$$L(\lambda) = \frac{1}{\alpha_{sym}(\lambda) + \alpha_{asym}(\lambda) + \alpha_{abs}(\lambda)} \quad (4.5)$$

In Equation 4.5, the α_{sym} parameter consists of two types of scattering: the symmetric component of Mie scattering and Rayleigh scattering, whereas α_{asym} only consists of asymmetric Mie scattering. Figure 4.10 shows the difference between these two types of scattering:

Rayleigh scattering occurs when light is scattered from very small particles, the size of these particles being less than 1/10 of the wavelength of the light. For particles larger than the wavelength of the light being scattered, Mie scattering becomes more dominant, with more asymmetric scattering occurring the larger the particle is (i.e. with a greater forward lobe for larger particles.) As a result of this α_{sym} has an angular dependence of $1 + \cos(\theta)^2$ where θ is the angle between the incoming and outgoing scattered photon vectors, but

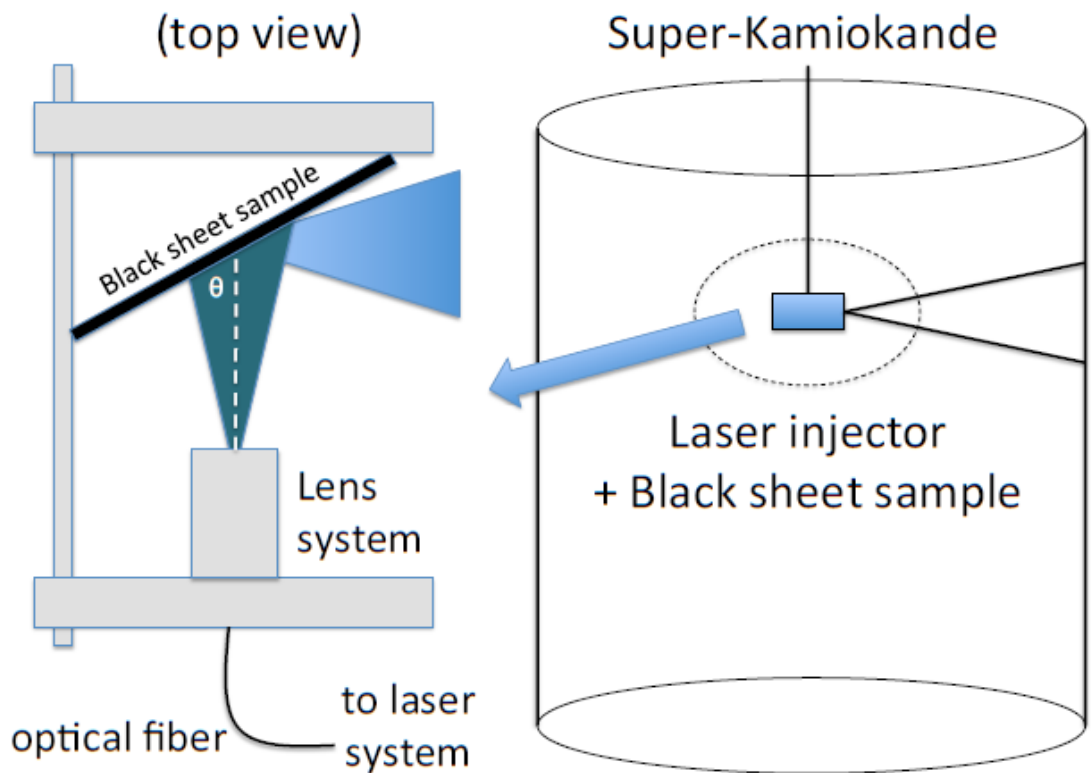


Figure 4.9: Schematic of the laser light reflectivity. Bird's-eye view (left) and setup inside of Super-Kamiokande (right).

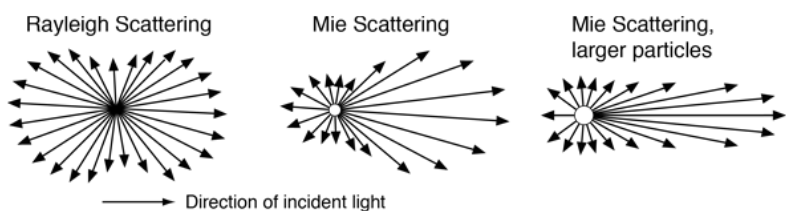


Figure 4.10: Schematic of the differences between Rayleigh and Mie scattering

α_{asym} has a $\cos\theta$ dependence, only for forward scattering, and an amplitude of zero for backward scattering. The $\alpha_{\text{abs}}(\lambda)$ is the amplitude of the light absorption. The method by which these measurements were made is by using a laser system (shown in Figure 4.11), where laser light is injected at several points in the tank, denoted in Figure 4.11 by the barrel injectors (B1-B5), the previously used old top injector (OT), the new top injector (NT), and an injector on the tank bottom (BT).

The absorption and scattering coefficients are measured using data from light injected from the new top (NT) injector. A large set of calibration Monte Carlo are generated using laser generation software and the Super-Kamiokande detector simulation (SKDETSIM). These set of Monte Carlo are generated with different values of absorption, symmetric and asymmetric scattering, and their timing distributions are compared to the data from the laser system in order to tune the amount of absorption, symmetric and asymmetric scattering in the calibration Monte Carlo. The way in which the $\alpha_{\text{abs}}(\lambda)$, α_{sym} and α_{asym} are defined is shown in Equation 4.6.

$$\begin{aligned}\alpha_{\text{abs}} &= P_0 \times \frac{P_1}{\lambda^4} + C \\ \alpha_{\text{sym}} &= \frac{P_1}{\lambda^4} \times \left(1 + \frac{P_5}{\lambda^2}\right) \\ \alpha_{\text{asy}} &= P_6 \times \left(1 + \frac{P_7}{\lambda^4} \times (\lambda - P_8)^2\right)\end{aligned}\quad (4.6)$$

The term C in the equation for $\alpha_{\text{abs}}(\lambda)$ is based on data from [32] for laser light with wavelengths greater than 464 nm while Equation 4.7 is used for wavelengths less than 464 nm.

$$C = P_0 \times P_2 \times (\lambda/500)^{P_3} \quad (4.7)$$

The values of P_0 to P_8 in Equations 4.6 and 4.7 were taken from fits to laser data taken in April 2009, the water coefficient functions of which are shown in Figure 4.12.

As well as the amount of absorption and scattering in the detector, there is also a dependence with respect to z-position in the detector, defined by Equation 4.8.

$$\alpha_{\text{tba}} = (\langle N_{\text{top}} \rangle - \langle N_{\text{bottom}} \rangle) / \langle N_{\text{barrel}} \rangle \quad (4.8)$$

Here $\langle N_{\text{top}} \rangle$, $\langle N_{\text{bottom}} \rangle$, $\langle N_{\text{barrel}} \rangle$ are the averaged hit probabilities of the top, bottom

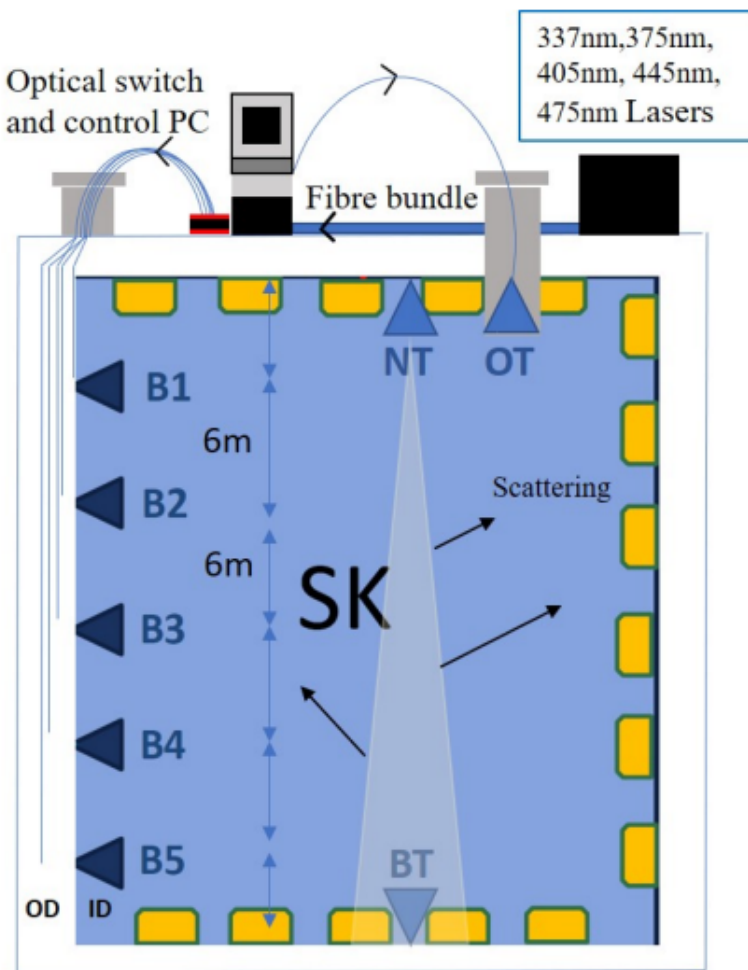


Figure 4.11: Schematic of the laser system

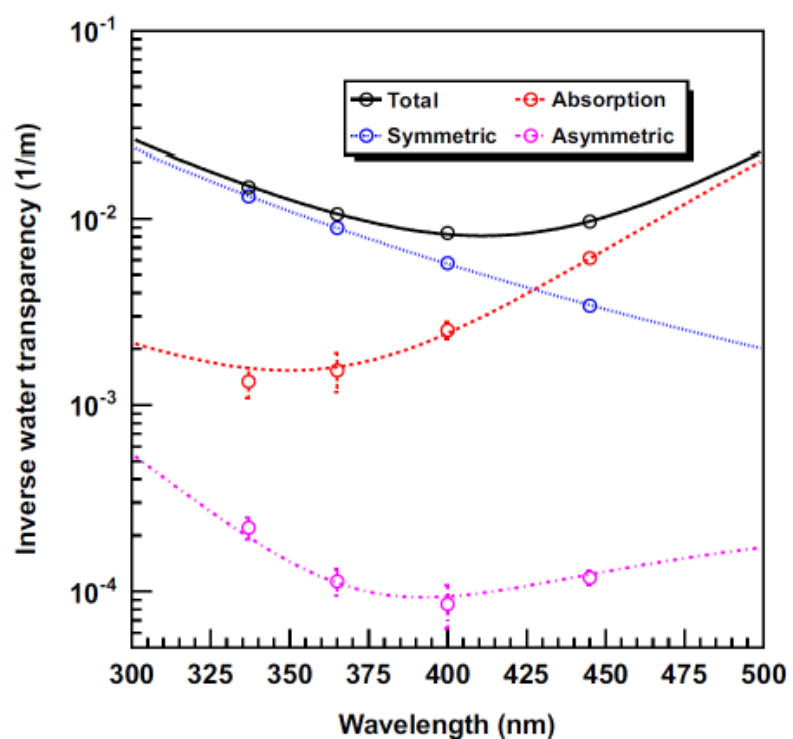


Figure 4.12: Plot of water coefficient functions used in Monte Carlo production, showing points for symmetric and asymmetric scattering and absorption.

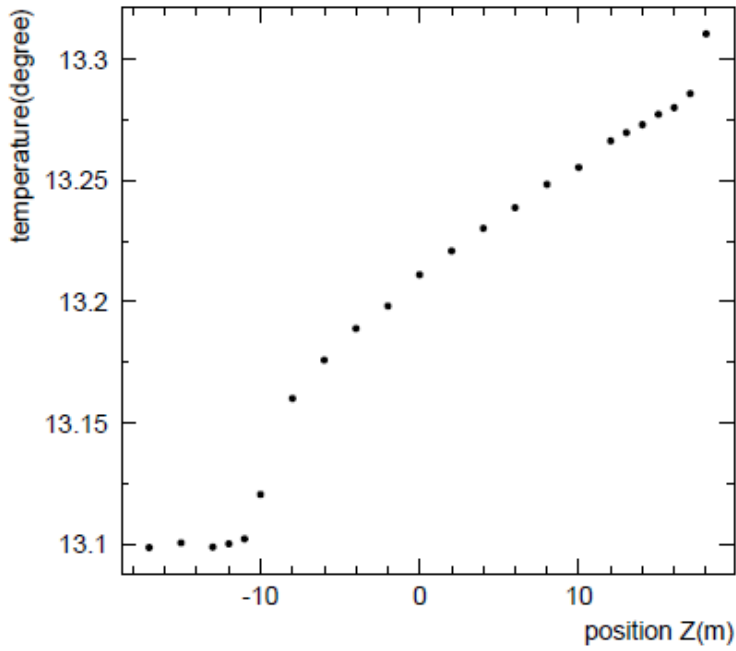


Figure 4.13: Dependence of temperature on vertical position in the Super-Kamiokande ID.

and barrel PMTs, where $\langle N_{\text{top}} \rangle$ is about 5% less than $\langle N_{\text{bottom}} \rangle$ due to the temperature gradient in the tank. Figure 4.13 shows this dependence, and Equation 4.1.6 shows how this is taken into account for the absorption coefficient α_{abs} by the factor $A(z, t)$:

$$\begin{aligned} A(z, t) &= 1 + z \cdot \beta(t) && \text{for } z \geq -11 \text{ m} \\ &= 1 - 11 \cdot \beta(t) && \text{for } z \leq -11 \text{ m} \end{aligned}$$

where from Figure 4.13, the value of $A(z, t)$ is constant below $z = -11 \text{ m}$, and above $z = -11 \text{ m}$ this value is determined by the z-position in the tank. The relationship between the value of β is related to the top-bottom asymmetry parameter α_{tba} , and for the April 2009 data α_{tba} and β are -4.91% and 0.01.

Chapter 5 expands upon these measurements by going into detail about the newly developed UK Light Injection system which improves upon the Korean laser system mentioned here used to make water coefficient measurements - it offers much narrower beam profiles which are shone onto the barrel regions, allowing for better analysis of the depth dependence of the water coefficients.

Chapter 5

The UK Light Injection System

The UK calibration group's efforts have been focussed on improving the data analysis method and improving the accuracy of the water coefficient measurements. To aid this effort a new UK developed Light Injection (UKLI) system was installed into Super-Kamiokande during the refurbishment that occurred in the summer of 2018 and this system has its own set of optics, which has optics with multiple beam spot diameters, which will be described in detail in this Chapter. The UKLI calibration system also involves the generation of Monte Carlo specific to the diameter of the beam spots produced from the UKLI, the production methods of which will also be discussed in detail in this chapter.

5.1 The UK Light Injection System Electronics

The electronics setup architecture for the UK Light Injection system is made of sixteen light emitting diode boards which are each coupled to three optical fibres, as well as a monitor PMT, an optical power meter and two motherboards as shown in Figure 5.1.

The light being pulsed has a wavelength of 435 nm and is produced by light emitting diodes which are controlled by Field Programmable Gate Arrays and uses sixteen LED pulser boards placed on two motherboards (8 LED pulser boards on each) which controls which channel to send a signal to. Fifteen of the sixteen channels deliver light into the detector, while the remaining channel sends light to a separate monitoring system. Each LED is coupled to three optical fibres, a channel connected to the monitor PMT, secondly to an optical fibre which sends light into the Super-Kamiokande detector, and to a spare. The monitor PMT is a 2 inch Hamamatsu PMT which has a peak sensitivity to 400 nm

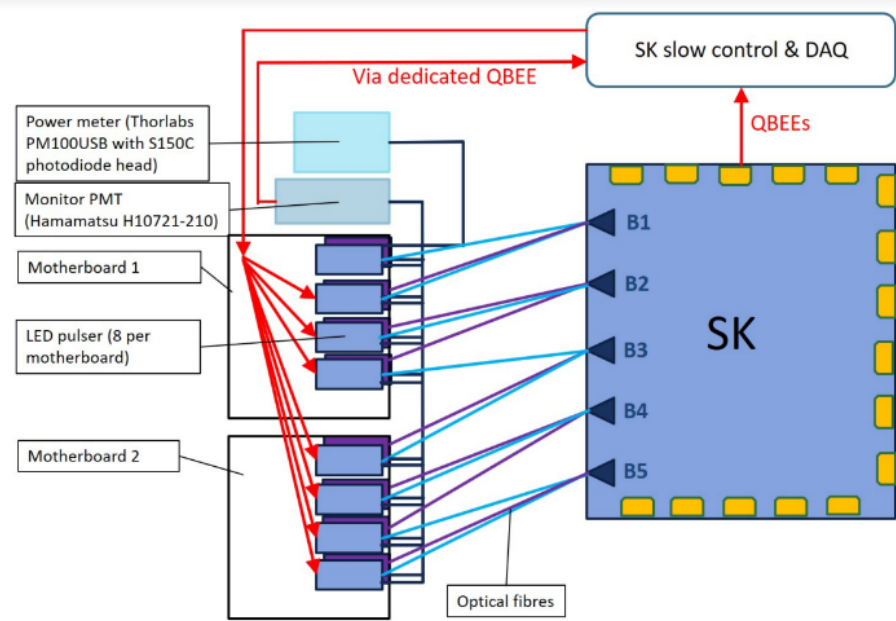


Figure 5.1: UKLI electronics system architecture, showing optical fibre and motherboard couplings and QBEE connections.

wavelength light. The monitor PMT is connected to one of the QBEE (QTC-based electronics with Ethernet) channels for the detector to record the monitoring signal into the data stream.

The monitor PMT is installed inside a custom 3D printed box to make sure there is no external light reaching it. There are nineteen fibres input to the PMT, these are kept in place against the PMT's photocathode. There is one fibre for each of the sixteen LEDs and the last three channels are reserve. The channel which is coupled to the LED board for monitoring of the system is used to calibrate the monitor PMT, where the signal from this channel is inputted into the optical power meter.

5.1.1 UKLI System Optics

Unlike the Korean laser system mentioned in Chapter 4 that injects light into the detector using an optical fibre which has an opening angle of 4 degrees, the UK Light Injection system contains three different types of light injection optics, with each having a different opening angle: a bare fibre, a collimator and a diffuser. This range of optics can accomodate

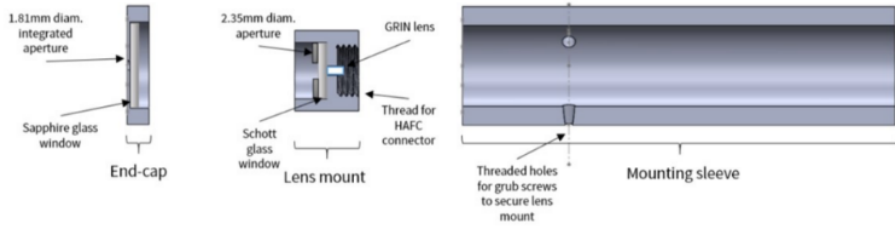


Figure 5.2: Collimator schematic including the end-cap, lens mount and mounting sleeve structures.

a larger variety of calibration measurements, and better suit the multiple applications of the light injection system, including it being better for monitoring purposes.

The Collimator Optic

A 2-degree opening half angle is achieved by the collimator optic by using a graded index lens (GRIN) connected to a bare fibre optic cable - this GRIN lens reduces the opening angle of the light coming from the fibre optic. A schematic of the collimator design can be seen in Figure 5.2. The GRIN lens is kept in position within the lens mount where a HAFC connector is drilled in to take a lens through the centre of the hole inside it, and there is a 2.35 mm diameter opening in front of the glass window in front of the GRIN lens in order to reduce background light which is not on-axis. All holes drilled into the collimator setup are filled with epoxy to prevent water from damaging the components.

Having such a confined beam allows for a very exact target position on the tank wall, and by decreasing the size of the target beam spot compared to the bare optical fibre, less hit PMTs outside of the target spot are excluded meaning that there are more hits in the water calibration data. Due to the fact that the very collimated beams mean that there is no overlap of beam spots, there can be measurements of the water scattering and absorption coefficients made that are position dependent, allowing for an observation of how the water parameters depend on depth in the tank.

The Diffuser Optic

The diffuser optic is a wide angled beam with a opening half-angle of 40 degrees. It allows for water coefficient measurement calibration and light attenuation length in water. The diffuser optic is made of a Poly(methyl methacrylate) (PMMA) ball which is a piece of acrylic resin in the shape of a half sphere and it contains PMMA particles suspended in

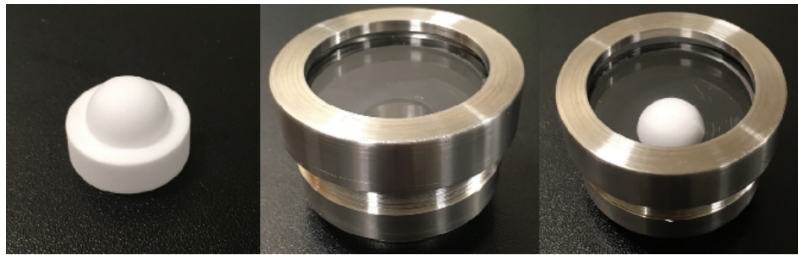


Figure 5.3: Photograph of the diffuser by itself (left), empty diffuser enclosure (centre) and diffuser inside enclosure (right).

silicone gel, similar to the design of the “laserball” used to calibrate the SNO+ detector [27]. As a result of this, the mean free path of light that is injected into the center of the diffuser ball is much shorter than the radius of the ball, so each photon scatters many times off the PMMA particles at random so that the exiting angle of the light is also random. This randomised exit direction of the photons means that the beam timing and intensity would be uniform.

Figure 5.3 shows a photograph of one of the diffusers used, and one of the diffuser ball enclosures. The enclosure is made of high grade stainless steel and using a chemical and water resistant epoxy resin, all the components were ensured to be watertight.

Bare Fibre and Optical Plate

The bare fibre injector are 1 mm step index fibres, and are approximately 20 cm in length and are used for validation purposes with the bare fibres in the Korean optical calibration system. These short fibres are screwed into the back end of the optical plate that the collimator and diffuser optics are mounted on.

Results of optics test stands

In order to test the collimator and diffuser optics, scans of the angular distributions were made using diffuser and collimator test-stands. These scans would show angular distributions of the light intensity, and details of the setup of each test stand are given here. For the diffuser test-stand the angular distribution of the light output was captured using the setup shown in Figure 5.4. A birds-eye view schematic of the setup is shown in Figure ??.

The test stand setup for the diffuser optics consists of a test diffuser ball placed inside a diffuser enclosure, a rotation stage which allows for the movement of the diffuser between

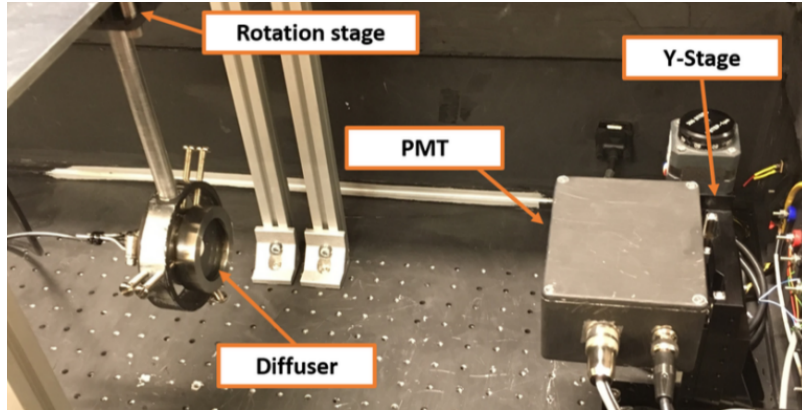


Figure 5.4: Setup of the diffuser test stand provided by Warwick University

-40 and 40 degrees, and a PMT used for pulse intensity measurement set up 250 mm away from the diffuser. An optical fibre couples the diffuser under test to a laser set to a wavelength of 450 nm.

The setup for the collimator test stand at the University of Warwick is shown in Figure 5.5. The setup for the collimator optic captures the beam cross section by moving a CMOS camera along the beam direction.

Figure 5.6 shows distributions provided by this test stand data which are preliminary TF1 fits made by ROOT to the light profiles for the diffuser. The x-axis scale shows the polar angle the rotation stand moves through, while the y-axis scale shows the average of the integrated area under all the pulses recorded by the PMT and is not normalised.

Figure 5.7 shows TF1 fits made by ROOT to the light profiles for the collimator. The angular distributions shown give the distribution of the polar angle in degrees of light intensity which are relative to the virtual position from which the light cone originates, averaged over all the orientations of the azimuthal angle.

UK Calibration data

In September of 2019 and November of 2019 two sets of test data were taken of the collimator, the diffuser and the bare fibre optic (the B2 bare fibre). For the September 2019 data, all of the data for the B1-B5 optics was taken with 100,000 events, however due to the B3 and B5 collimator from the September 2019 data showing a very weak signal, 150,000 events were taken with the B3 collimator data and 200,000 events were taken with

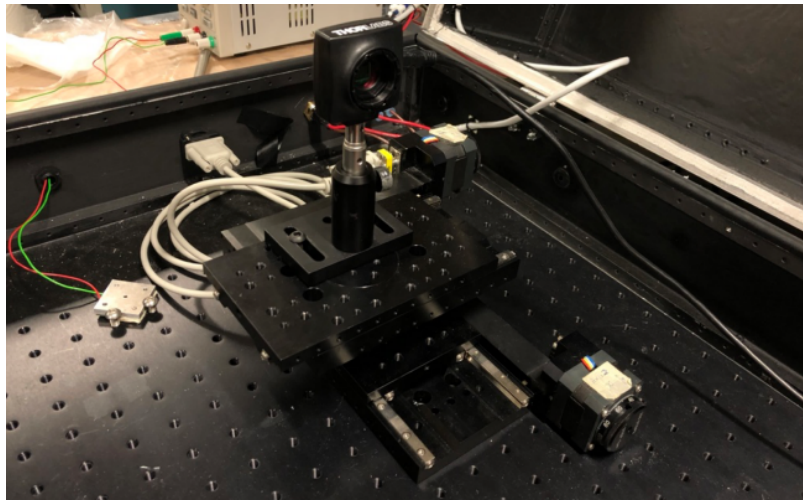


Figure 5.5: Setup of the collimator test stand provided by Warwick University

Figure 5.6: Light profiles for the diffuser optics provided by The University of Warwick

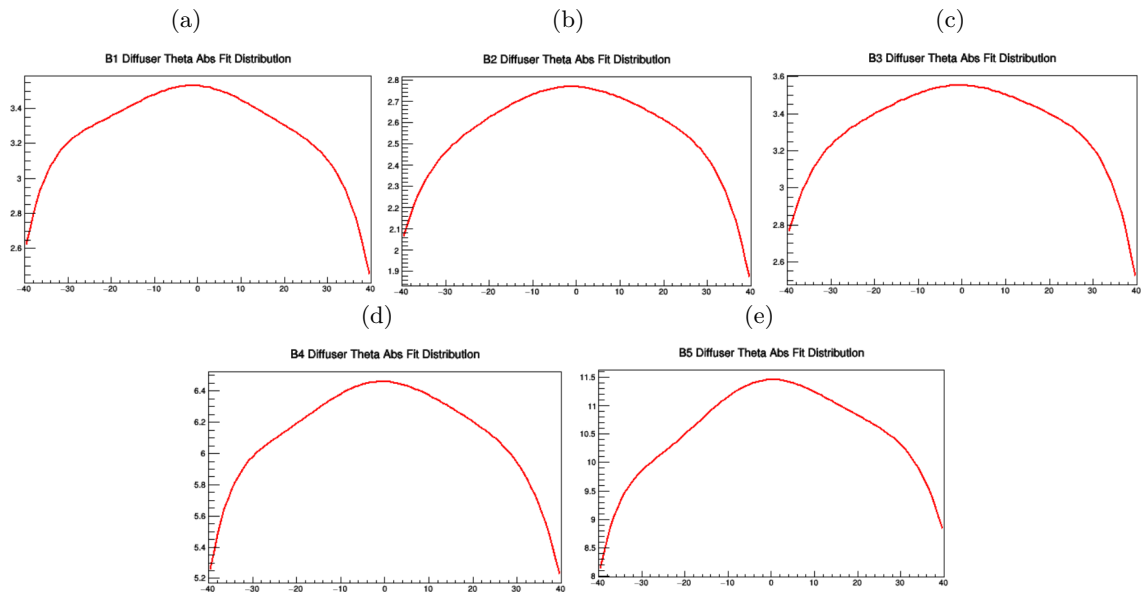
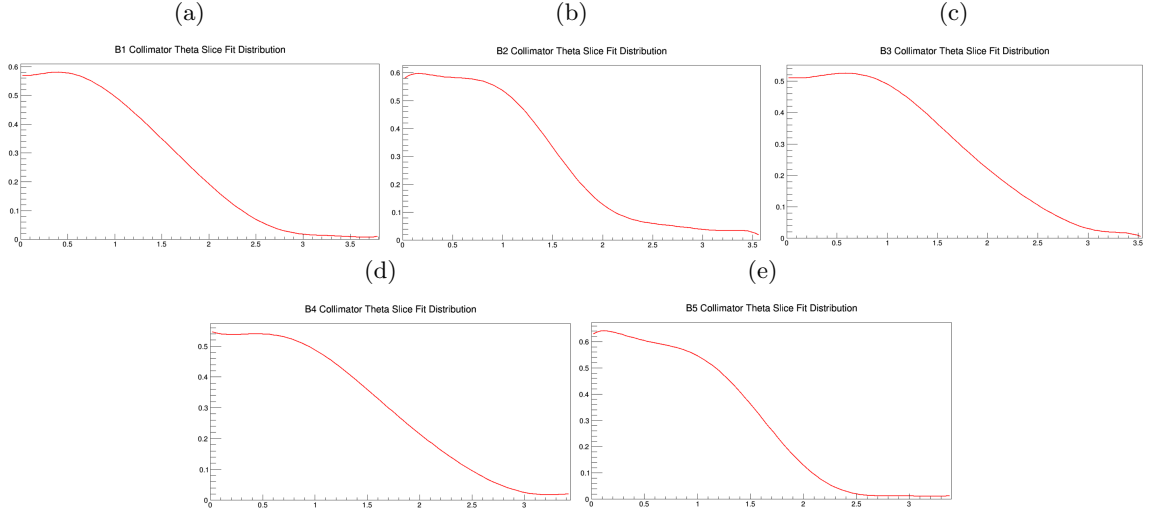


Figure 5.7: Light profiles for the collimator optics provided by The University of Warwick



the November 2019 data. Using an event display developed by the University of Warwick, occupancy plots of the test data sets were produced. Figure 5.8 shows the occupancy plots for the collimator optic from the November 2019 dataset showing the beam spot inside the unrolled volume of the Super-Kamiokande detector. Similarly, Figure 5.9 shows the occupancy plots for the diffuser optic from the November 2019 dataset. The graph in the bottom right hand corner of the occupancy plots show the corrected time-of-flight plots for the PMT hits from the injector.

In addition to test data being taken, there is also an “autocalib” system used for long term monitoring of the water parameters in Super-Kamiokande by the Korean laser system. In early 2020 the autocalib scheduler was modified to incorporate data taking by the UKLI system which was very useful for Gadolinium loading calibration purposes but also in the longer term, it will be useful in the monitoring of daily/weekly water coefficient property measurements, investigation of depth dependence with respect to the water properties and PMT property calibration. Figure 5.10 shows the schedule for autocalib, and the black dashed lines show the position of the UK barrel collimator and diffusers with respect to the other autocalib data taking streams. The horizontal blue line shows the length of the one autocalib cycle, which is about 4.6 seconds, with each UKLI optic taking about 3310 events per day.

Figures 5.11 and 5.12 shows the occupancy plots for autocalib data taken in July 2020:

Figure 5.8: Occupancy plot for the collimator optics from the UKLI November 2019 test run

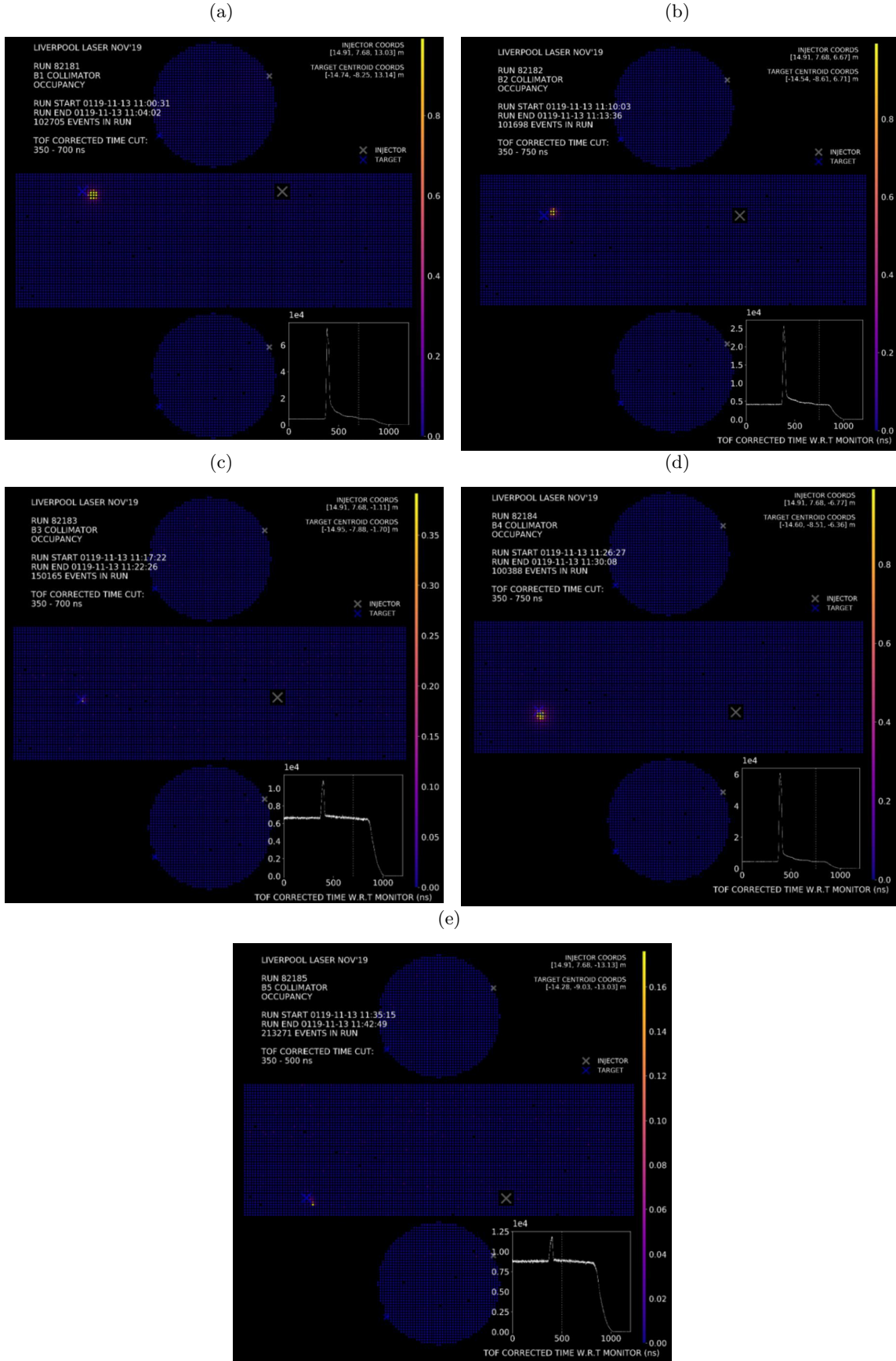
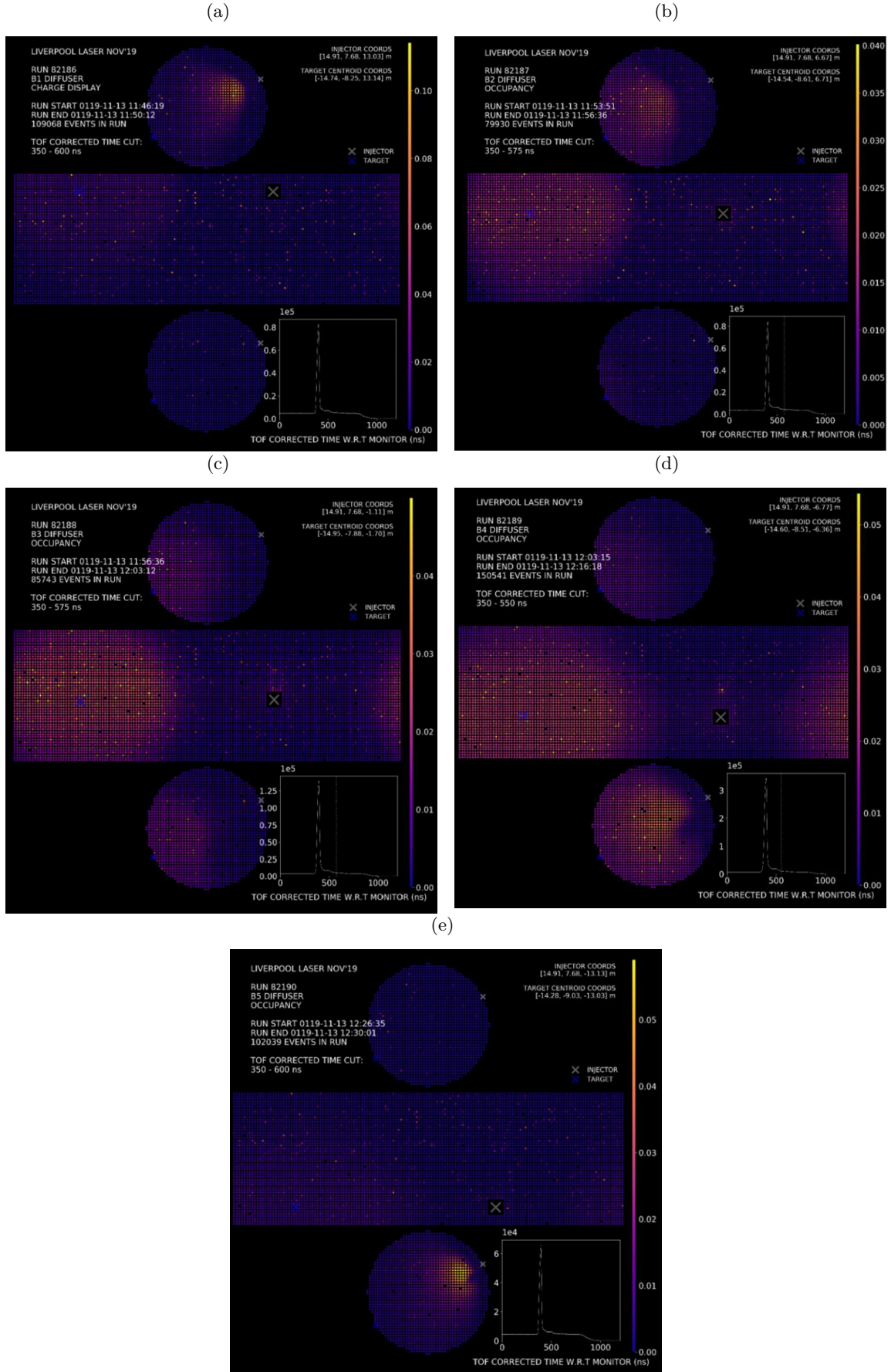


Figure 5.9: Occupancy plot for the diffuser optics from the UKLI November 2019 test run



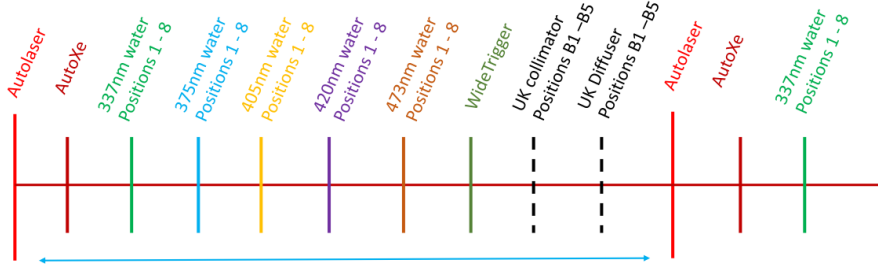


Figure 5.10: Schematic showing position of the UKLI in autocalib scheduler: the black dashed lines show the UKLI B1-B5 collimator and diffuser optics and the horizontal blue line shows the length of one autocalib cycle.

as can be seen in the text in the upper left hand corner, the number of events in the run is a lot less than the 100,000 events or so taken in the test runs, however they are more than sufficient for monitoring purposes.

Implementation of UKLI MC in SKDETSIM

After making these fits to data the next aim was to use these light profiles as an input to SKDETSIM, the Super Kamiokande Detector Simulator. SKDETSIM uses GEANT3 (GEometry ANd Tracking 3) to simulate what the particles in each event would do inside the detector, and tracks the particle's trajectories and energy loss. Simulating the light injection from the UKLI system in SKDETSIM was done in a similar way to the Korean method of producing Monte Carlo: the same versions of the calibration scripts were used however, small modifications were made to them and to the version of SKDETSIM used to simulate the input photons from the system in the detector. The calibration scripts used for the Korean and UKLI systems both allow for the number of events and the number of injected photons to be set, in order to generate many Monte Carlo files with the absorption, Rayleigh and Mie scattering parameters.

The first step regarding making UKLI based Monte Carlo was changing the position of the injector locations from the positions of the Korean system (shown in Table 5.1) to that of the UKLI system (shown in Table 5.2), due to the fact that the spacing gap rungs between the UK system and the Korean system is +70.7 cm for the B1, B2, B3 barrel injectors and -70.7 cm for the B4 and B5 injectors. The opening angle of the injectors determined by the simulation also had to be changed because the simulation had to accomodate the fact that the injectors for the UKLI system now consisted of three different opening angles for the

Figure 5.11: Occupancy plot for the collimator optics from the UKLI Autocalib July 2020 run

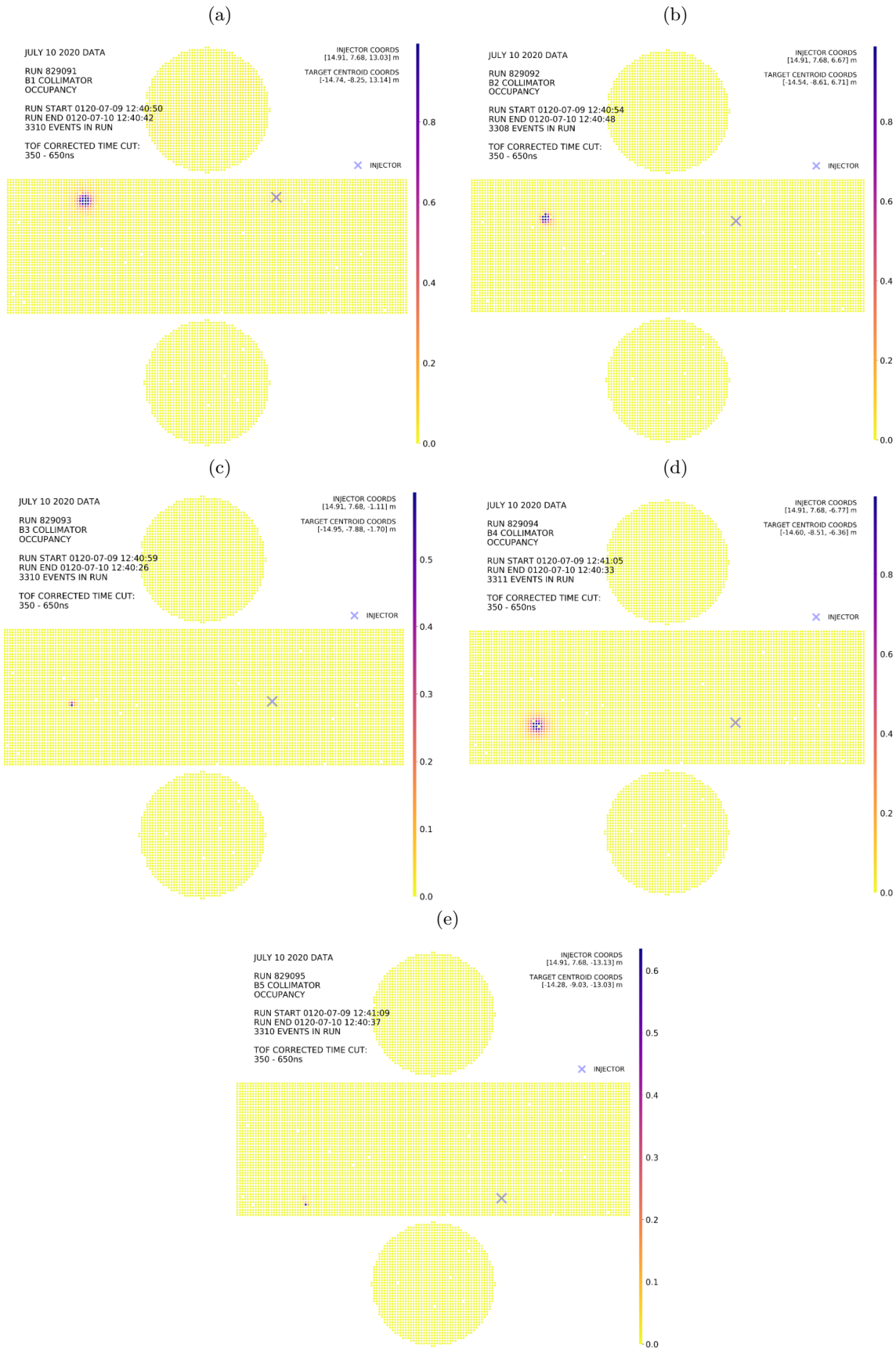
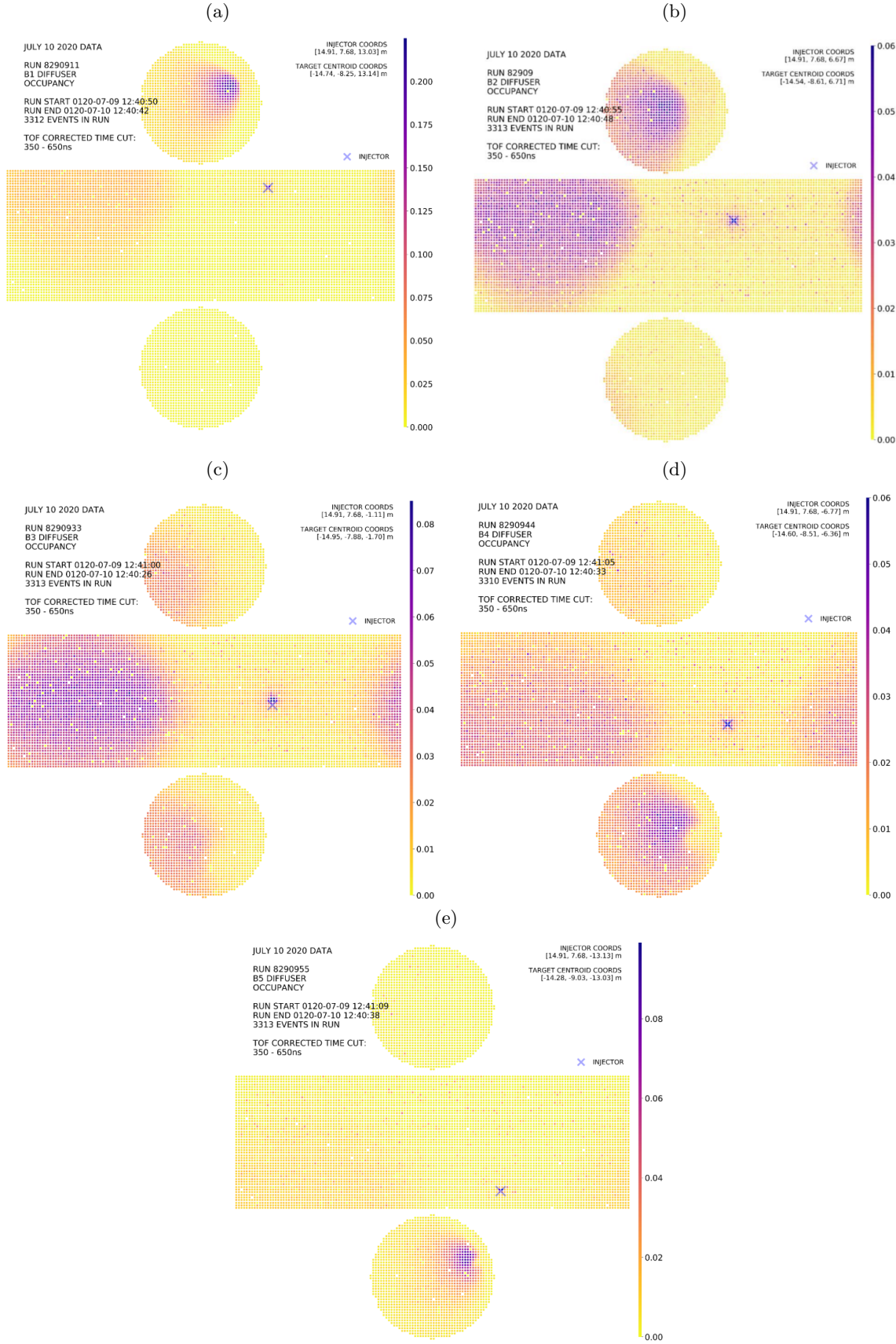


Figure 5.12: Occupancy plot for the diffuser optics from the UKLI Autocalib July 2020 run



collimator, diffuser and bare fibre optics, instead of just the bare fibre optics used in the Korean system. The way the opening angle for the Korean was set was using the “SIGBM” parameter which stands for the sigma of the input injector beam, and was produced using a Gaussian random number generator to produce the phptpn angle. However an entirely new method of determining the opening angle of the beam was needed to include the information from the light profiles taken from the test stands at Warwick. In order to understand the SIGBM parameter further however, the relationship between opening angle in degrees and SIGBM was plotted by outputting the SIGBM value and the angle to a text file during laser generation Monte Carlo production (shown in Figure 5.13.)

Korean Barrel Injector	x (cm)	y (cm)	z (cm)
B1	1490.73	768.14	1232.25
B2	1490.73	768.14	595.95
B3	1490.73	768.14	-40.35
B4	1490.73	768.14	-605.95
B5	1490.73	768.14	-1242.25

Table 5.1: Barrel injector positions (x,y,z) of the Korean injectors in cm

UKLI Barrel Injector	x (cm)	y (cm)	z (cm)
B1	1490.73	768.14	1302.95
B2	1490.73	768.14	666.2
B3	1490.73	768.14	-111.05
B4	1490.73	768.14	-676.65
B5	1490.73	768.14	-1313.95

Table 5.2: Barrel injector positions (x,y,z) of the UKLI injectors in cm

In order to validate the positions of the targets for the UKLI system, and the relationship between the SIGBM parameter and output angle, producing charge weighted histograms from UKLI test runs is very helpful. It allows us to explore the shape of the beam profile and intensity. Figures 5.14 and 5.15 shows the charge weighted z-profiles for the September and November 2019 datasets for the B1 and B4 collimator injectors, where the blue dashed line shows the expected target position. These are produced by selecting hit PMTs which are greater than 2 m away from the injector (to avoid including PMT hits from backscattered light), and filling the histogram with the z-position of the

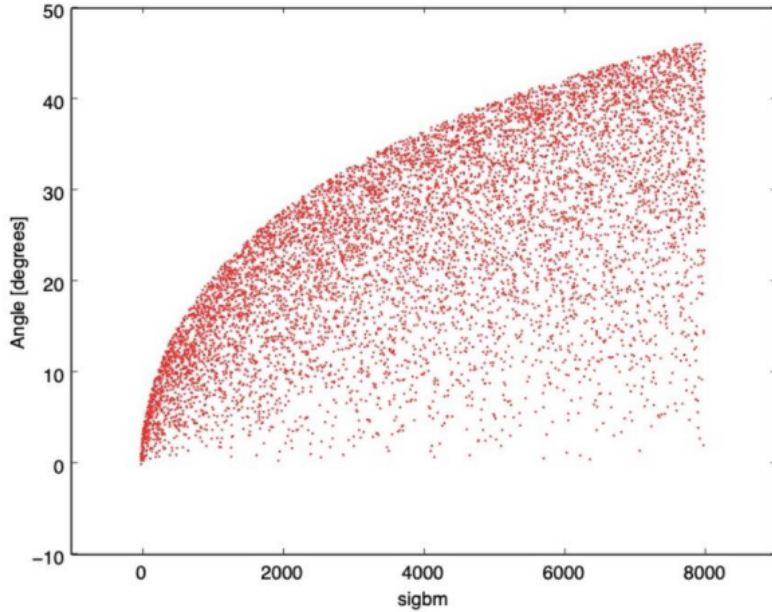


Figure 5.13: Relationship between the SIGBM parameter value and the opening angle of the beam in degrees

hit PMT and the number of hits the hit PMT receives multiplied by the corrected charge from the PMT. The corrected PMT charge is calculated using Equation 5.1, where the gain correction value is taken from official Super-Kamiokande gain tables.

$$q/(1 + gain) \quad (5.1)$$

The B1 and B4 collimator optics give the largest peaks in the charge weighted plots, while the B3 and B5 optics give the weakest peaks, practically indistinguishable from the background pedestal (even with the additional number of events taken during the November data taking runs.) The charge weighted plots were used to validate the relationship between the opening angle of the injector beam in the Monte Carlo production calibration scripts by generating Monte Carlo scripts with varying values of the SIGBM parameter (while keeping the absorption and scattering parameters the same). Fitting the charge weighted profile plots with a Gaussian and using the position of the injector target and the edge of the beam spot, the opening angle of the beam in degrees could be determined.

The width of the beam needed to be defined in order to do this however, and the

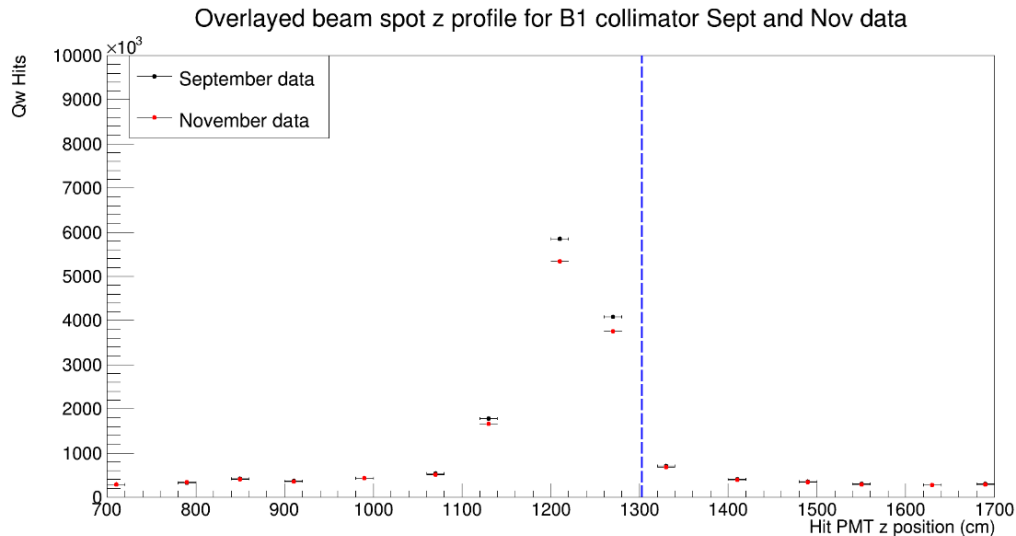


Figure 5.14: Charge weighted z profile plots for the B1 collimator UKLI injector optic

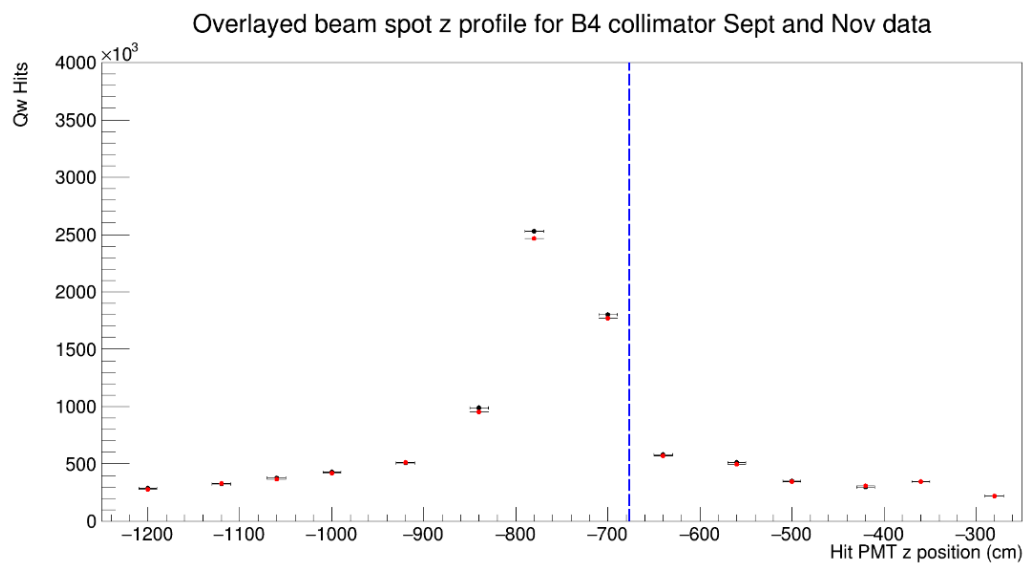


Figure 5.15: Charge weighted z profile plots for the B4 collimator UKLI injector optic

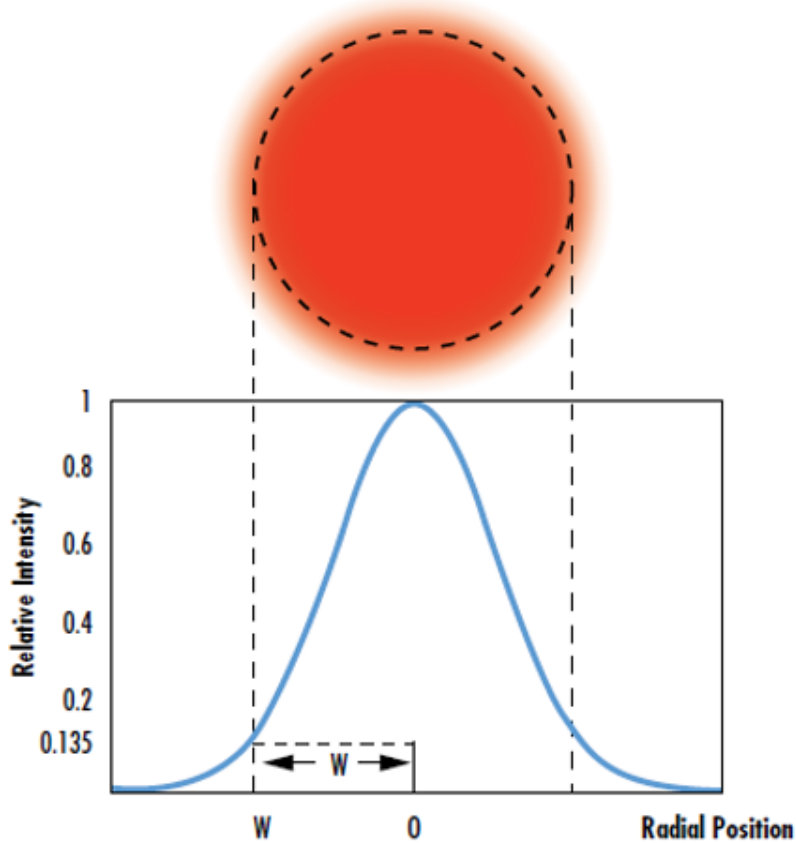


Figure 5.16: Schematic showing how the width of the MC beam was defined

standard beam radius definition is shown as in Figure 5.16. This schematic shows that the width of the beam was defined as using $1/e^2$ for the edge of the beam width, so it is taken as the point where the intensity drops to 0.135 of the Gaussian peak value. While there is good agreement at small opening angles, there is a slight discrepancy between this plot and Figure 5.13 at larger opening angles, where in Figure 5.13 the angle in degrees is consistently greater than in Figure 5.17 for the same value of SIGBM, and this is due to SIGBM being defined as the maximum opening angle, however for small opening angles as for the collimator, the comparison is valid.

After using the charge weighted hit plots to understand the SIGBM parameter and how the opening angle is generated by SKDETSIM more thoroughly, the next step involved using the profiles from the Warwick optic test stands (shown in Figures 5.7 and 5.6)

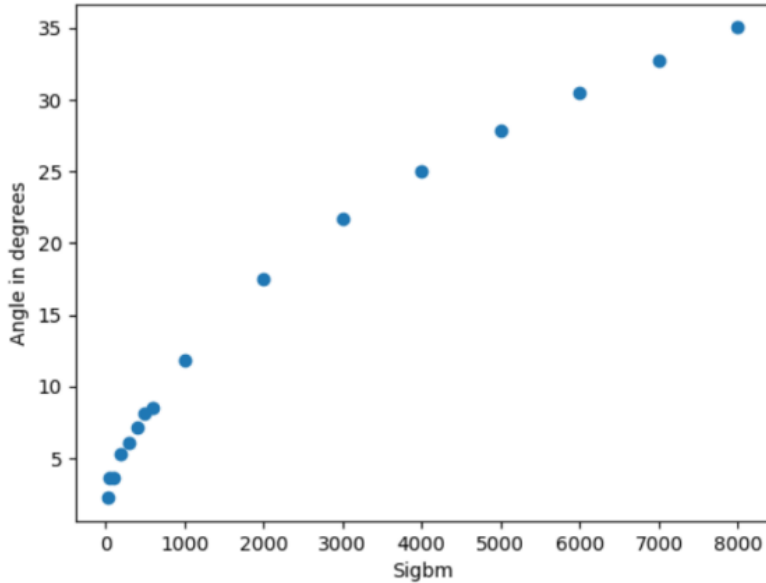


Figure 5.17: Plot of the sigbm parameter vs angle in degrees produced using calculation of the opening angle from the beam width

in the production of this opening angle in the detector simulation. This was done by treating the profiles in Figures 5.7 and 5.6 as Probability Distribution Functions (PDFs) and using inverse transform sampling to make the detector simulation sample at random from it. Inverse transform sampling is a method for generating random numbers from any probability distribution by using the inverse of its cumulative distribution $F^{-1}(x)$. For continuous distributions, such as the results from the collimator and diffuser optics test stands, the algorithm for inverse transform sampling is simple. Firstly, a random variable U is uniformly distributed between $[0,1]$, and secondly the relation $X = F_x^{-1}(U)$ would then produce a distribution X following the original probability distribution function, i.e. that of the original PDFs from the optics test stands.

The first step is to produce the CDFs from the PDFs from the optic test stand profile tests. Figure 5.7 shows that the original fits to the collimator data did not reach 4 degrees, and as a result the PDFs produced needed to be linearly extrapolated from 3.5 degrees where the measurements cut off to reach 4 degrees. Figure ?? shows the PDFs and CDFs produced from the collimator data, and Figure ?? shows the PDFs and CDFs produced from the diffuser data. The CDFs are normalised with a max of one using min-max scaling.

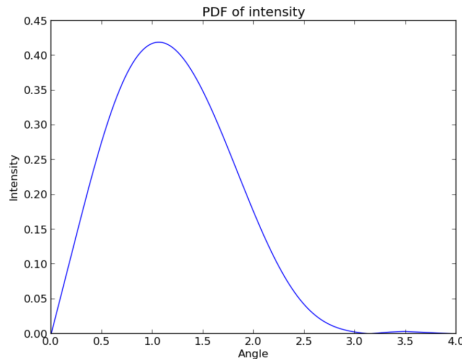


Figure 5.18: PDF for the B1 collimator

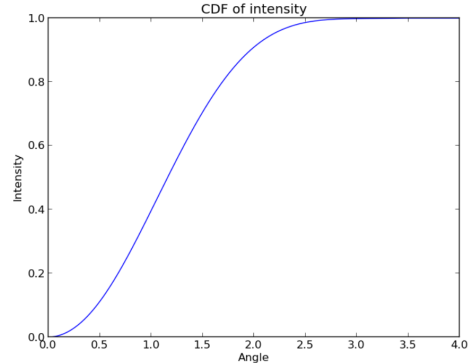


Figure 5.19: CDF for the B1 collimator

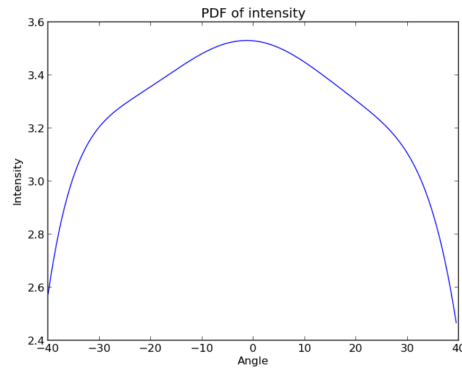


Figure 5.20: PDF for the B1 diffuser

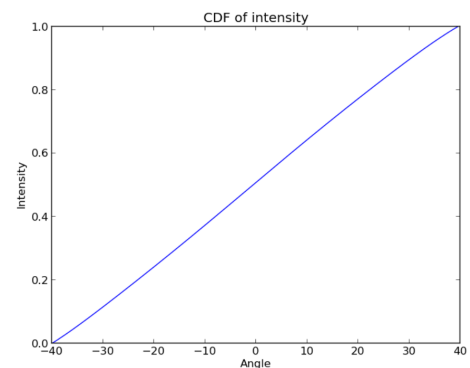


Figure 5.21: CDF for the B1 diffuser

The PDFs and CDFs for the B2 - B5 collimators are shown in Figure ?? and the PDFs and CDFs for the B2 - B5 diffusers are shown in Figure ??.

After producing the normalised CDFs, the inverse of these CDFs are calculated - Figures 5.22 shows the comparison of the normalised CDF data for the B1 collimator (top subplot, shown in blue) and the polynomial fit to the CDF for the B1 collimator (top subplot, shown in red), and the inverse CDF function (bottom subplot shown in green) and the polynomial fit to this inverse CDF function (bottom subplot shown in purple). Figures 5.23 shows the same plot for the B1 diffuser.

After producing the fits to the inverse cumulative distribution functions, these functions were inputted into the detector simulation, SKDETSIM. Removing the SIGBM parameter from the calibration scripts meant there needed to be a new way with which to generate the angle at which the photons were produced in the simulation, and this is where the

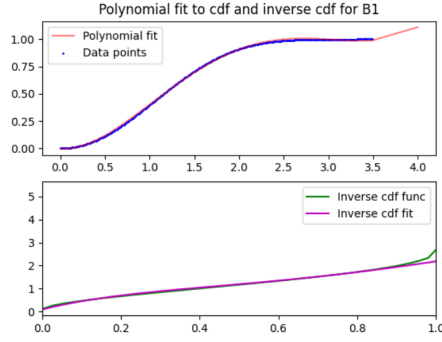


Figure 5.22: Inverse CDF for the B1 collimator

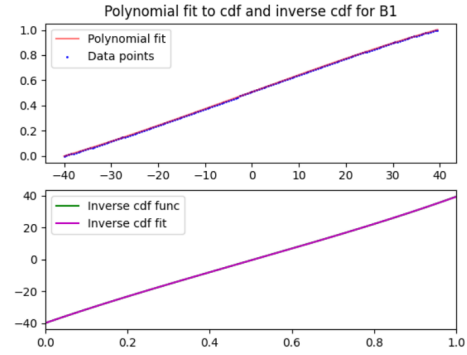


Figure 5.23: Inverse CDF for the B1 diffuser

inverse transform sampling occurs for the relevant fit for the selected injector and optic type. Using the same event display used to produce the occupancy plots for the autocalib data and the test run data, occupancy plots of the Monte Carlo were produced. These are shown for the B1 - B5 collimators in Figure 5.24, and for the B1 - B5 diffusers in Figure 5.25. These MC were produced with the abs, ray and mie parameters in the calibration scripts set to 1.0, 1.0, and 1.0 (i.e. the current detector simulation values) and the top-bottom asymmetry parameter set to 7.598, which is the most recently tuned value of this parameter. Because the original profiles from the test stands were taken in air, adjustments were made so that the refractive index of the water in the detector was taken into account when implementing the inverse CDFs into the detector simulation.

In order to validate the diffuser MC inverse cumulative distribution function output, a uniform distribution was run through the equation for the diffuser inverse CDF fits and the original PDF fit for each diffuser was used to fit the output points from the distribution, showing that inverse transform sampling was done correctly for the PDFs. These are shown for each diffuser in Figure 5.26.

After producing the UKLI MC, the next step was to use them to measure the absorption and scattering parameters in a similar way to the Korean system. As mentioned earlier, this was done by producing time of flight corrected hit timing plots for UKLI MC with multiple different values of absorption, and Rayleigh and Mie scattering parameters and comparing them to the TOF corrected plots for UKLI data. Figures 5.27, 5.28 and 5.29 show the time-of-flight corrected plots for the UKLI MC B1 collimator, produced with values of the “abs” and “ray” calibration script parameter between 0.7 and 1.3 to show the

Figure 5.24: Monte Carlo simulations of the B1 -B5 collimator injectors

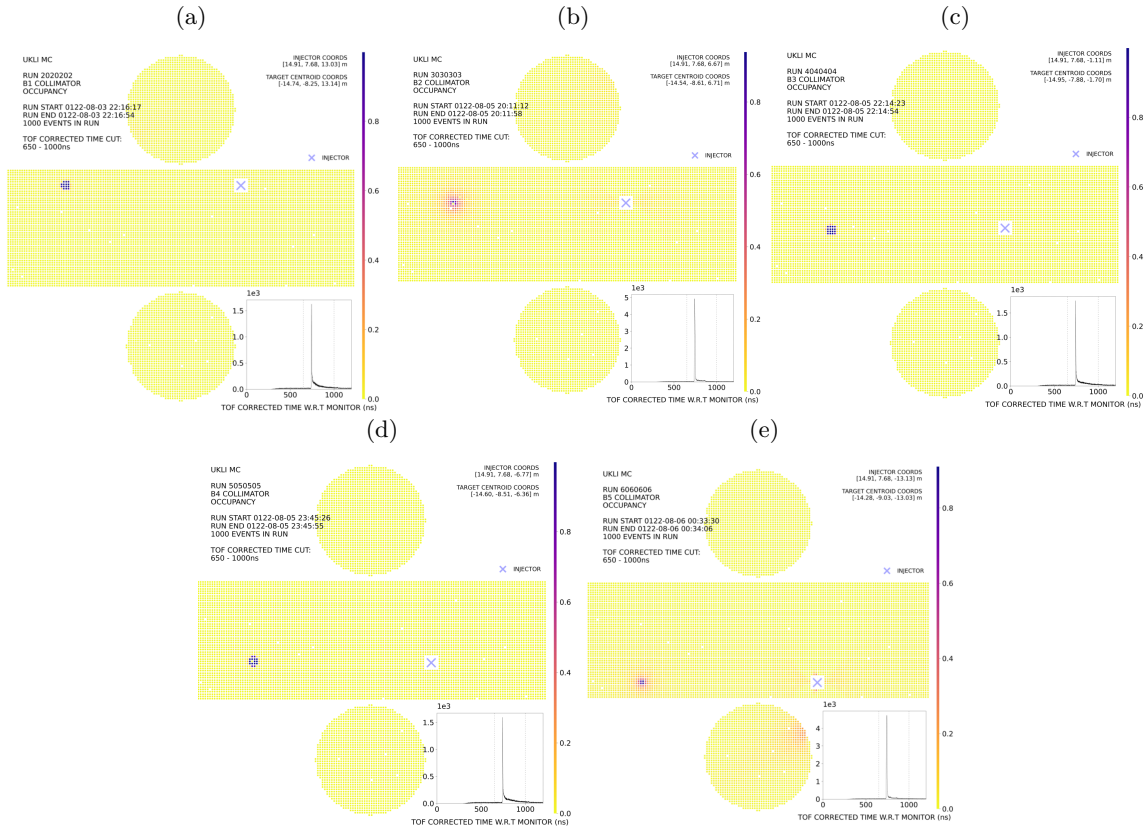


Figure 5.25: Monte Carlo simulations of the B1 -B5 diffuser injectors

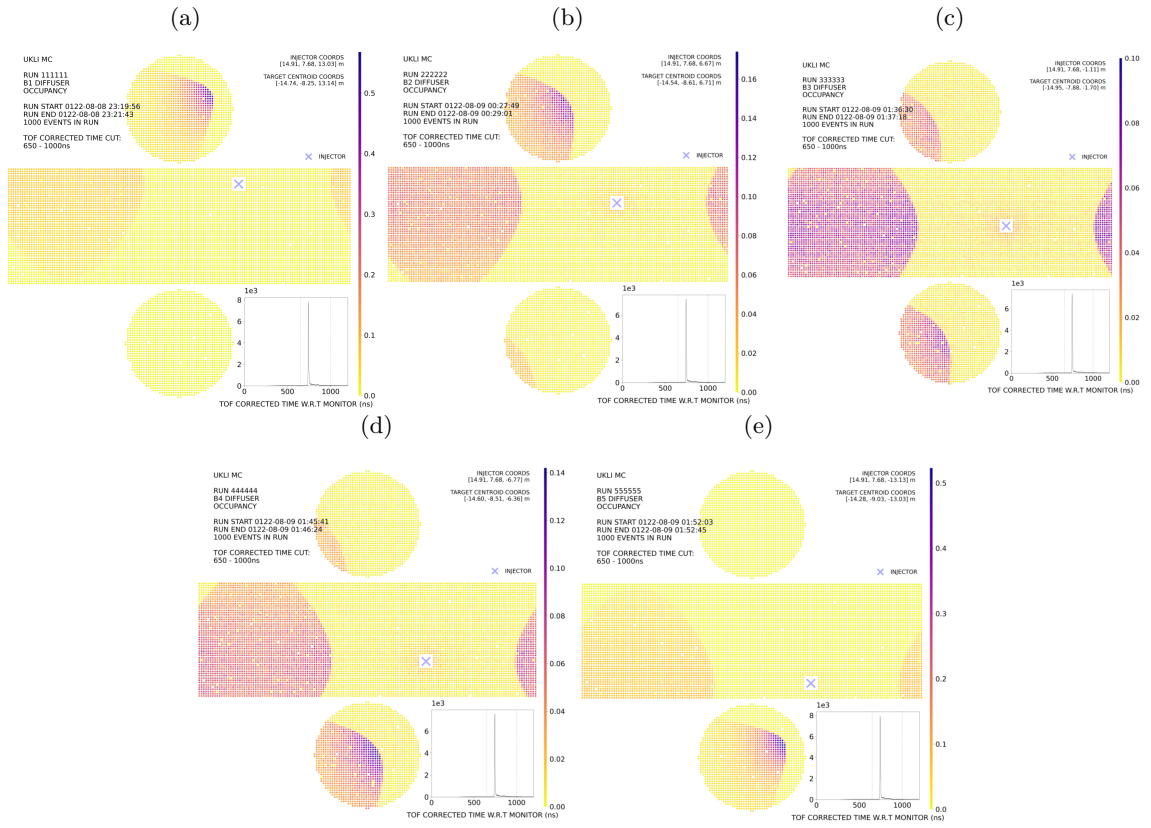
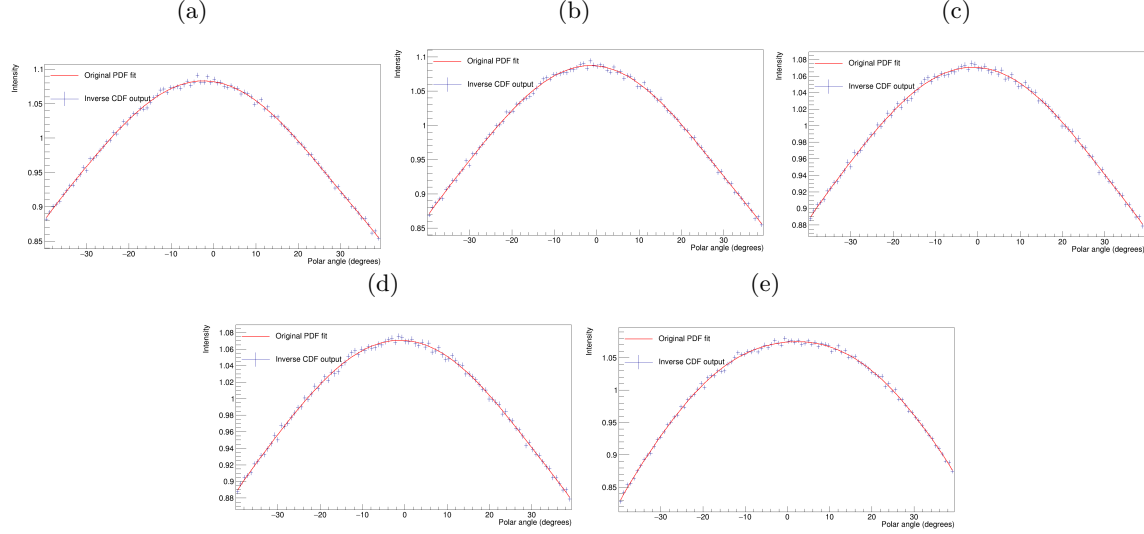


Figure 5.26: Plots of the result of running randomly sampled numbers from a uniform distribution through the inverse CDFs (in black) for each diffuser, along with the original PDF fits (in red) for the B1 - B5 diffusers.



affect that varying these parameters have on the time of flight corrected hits. The y-axis shows the number of hits normalised by the total charge in the detector.

As shown in Figure 5.28, the TOF corrected timing plots are most affected by the Rayleigh scattering parameter, which affects the amount of hits in the scattered hits region, while varying the absorption parameter mostly affects the height of the reflected peak, as the higher the amount of absorption in the tank, the smaller the number of reflected hits.

After producing time-of-flight corrected plots for the B1 collimator UKLI MC and overlaying it with the Run 82181 November test run data with the abs, ray, mie parameters set to 1.0, and a TBA value of 7.598, it was clear that there were disagreements between the Monte Carlo and data in both the scattered hits region and the reflected hits peak. In order to change this, the time dispersion of the reflected hits peak was varied, in order to shift the distribution and better match up the UKLI Monte Carlo and test run data.

The time dispersion for the injected photons in the laser generation in SKDETSIM is governed by a Gaussian distributed random number generated using a Box-Muller transform, where additional time dispersion added would be the sigma of this Gaussian, and after a random number is passed through it, the output number would be added to the time for each track step of the photon giving the time dispersion.

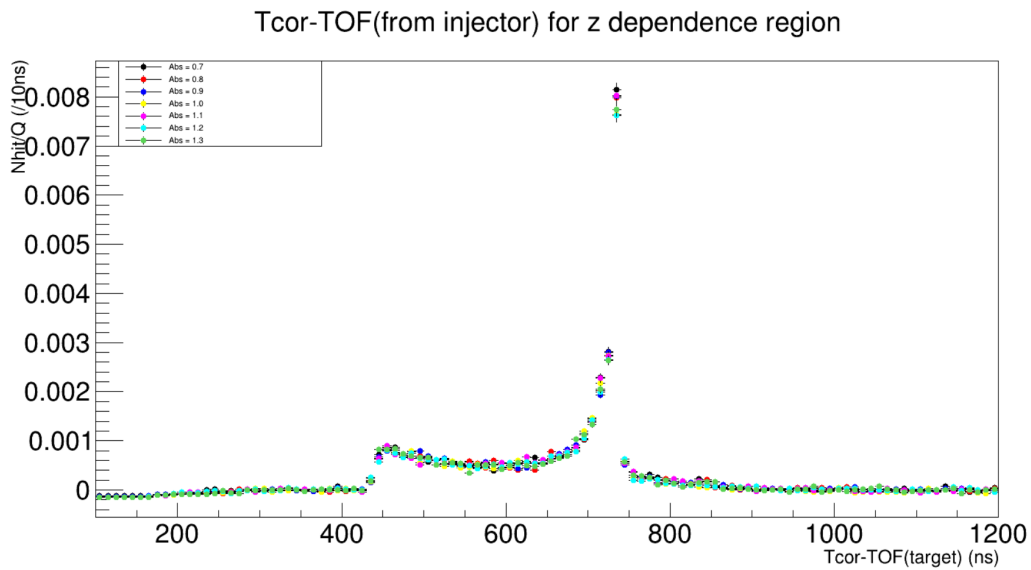


Figure 5.27: Corrected TOF plot with varied absorption, while rayleigh and mie scattering is set to 1.0

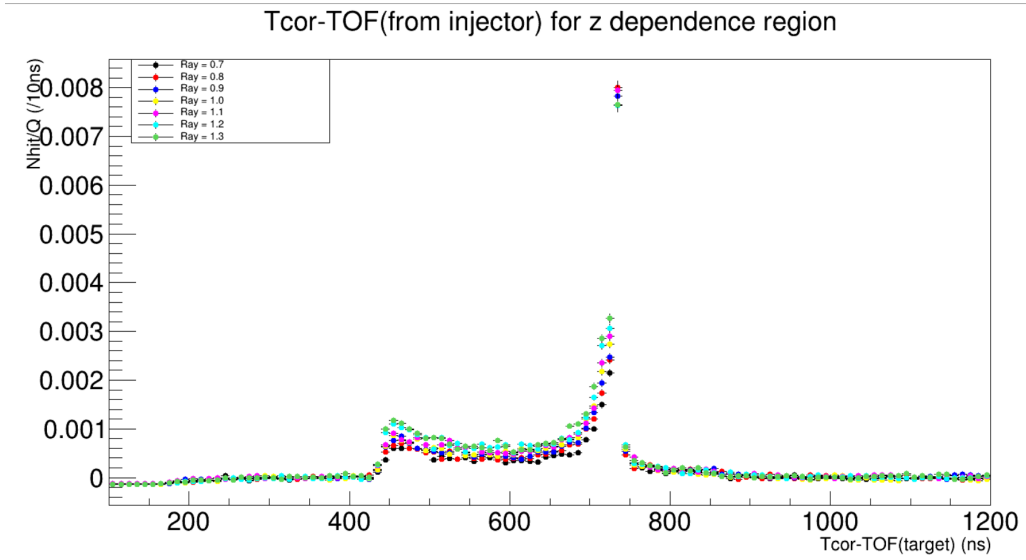


Figure 5.28: Corrected TOF plot with varied Rayleigh scattering, while absorption and Mie scattering is set to 1.0

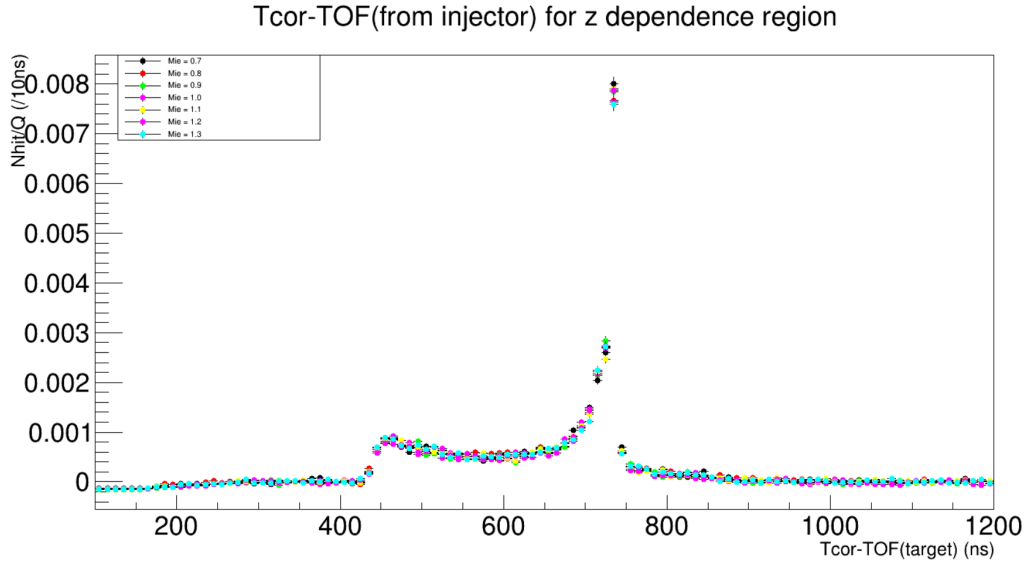


Figure 5.29: Corrected TOF plot with varied Mie scattering, while absorption and Rayleigh scattering is set to 1.0

The Box-Muller transform is a random number sampling method for making pairs of independent, normally distributed random sources from a source of uniformly distributed numbers (from between usually from between 0 and 1) [12]. The form of the Box-Muller method implemented to calculate the added time dispersion is the Marsaglia polar method [24], which works by choosing two independent and uniformly distributed numbers (u, v) between $[-1, +1]$, so that $s = u^2 + v^2$, and if $s = 0$, or $s \geq 1$, another pair of numbers are chosen. Then the standard normal deviate which is given by

$$z_0 = u \cdot \sqrt{\frac{-2 \ln s}{s}}$$

is multiplied by the chosen value of time dispersion in seconds and added to the mean (set to zero) to give the normally dispersed extra track step time for a photon in the distribution.

Figure 5.30 shows the effect of implementing this varying time dispersion on the raw hit timing output from the UKLI MC B1 collimator simulation, with the time dispersion shown for 0 ns, 5 ns, 10 ns, 15 ns, 20 ns and 100 ns.

Along with implementing the Gaussian distributed time dispersion, introducing a double gaussian for the time dispersion was also looked at, due to the height and sharpness of

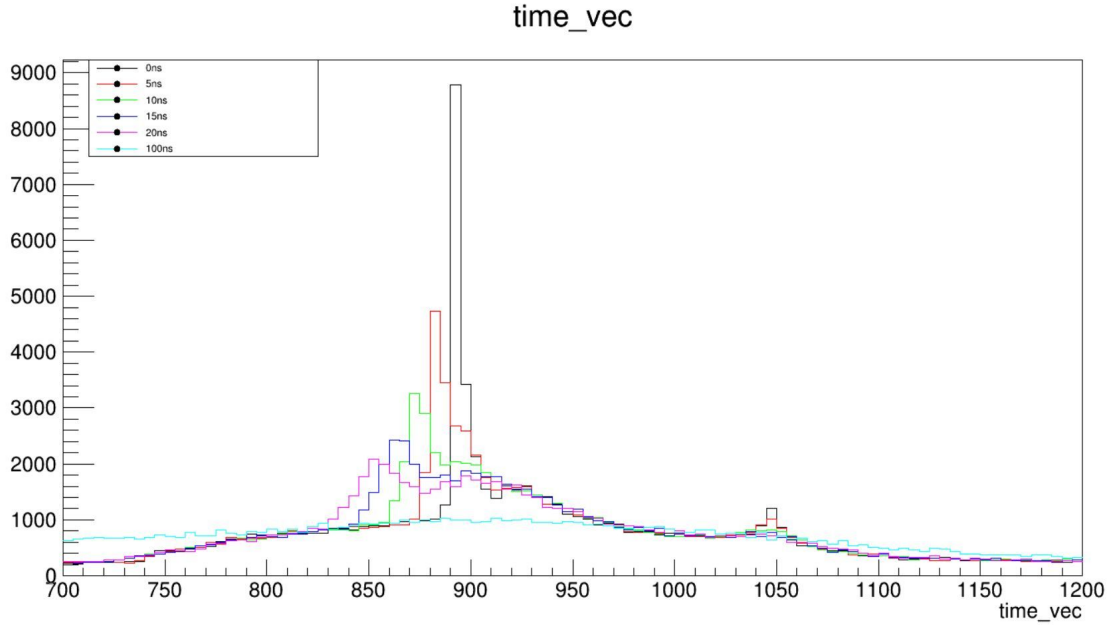


Figure 5.30: Gaussian distributed time dispersion plots, with varying amounts of time dispersion

the reflected peak in the data being something that might be better suited to such a fit. Figure 5.31 shows the raw hit timing output from the UKLI MC B1 collimator simulation with a double gaussian time dispersion, for varying time dispersion values. The x-axis on the plots show the hit time in nanoseconds, the y axis is number of events.

Figures 5.32, 5.33, 5.34, 5.35 show these time-of-flight corrected plots with both a gaussian and double gaussian time dispersion put in for varying amounts of time dispersion for 5, 10, 15 and 20 ns respectively.

For the scattered hits region (region between the dashed lines), there is now good agreement between the MC and data, with this region giving Chi2/NDF values of less than one, and the time dispersion values of 5 ns and 10 ns giving the best agreement. A problem remains regarding the reflected hits peak, where the data continues to have a much higher reflected peak than the Monte Carlo. This points to the amount of charge in the detector for the reflected peak being too large for the Monte Carlo, and further studies will be needed to be done to tune this.

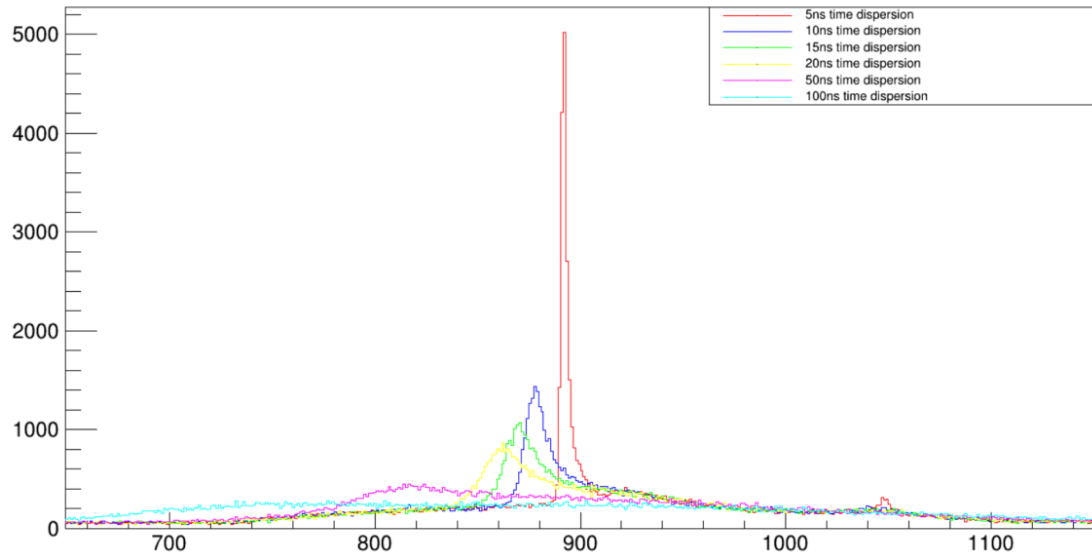


Figure 5.31: Double gaussian distributed time dispersion plots, with varying amounts of time dispersion

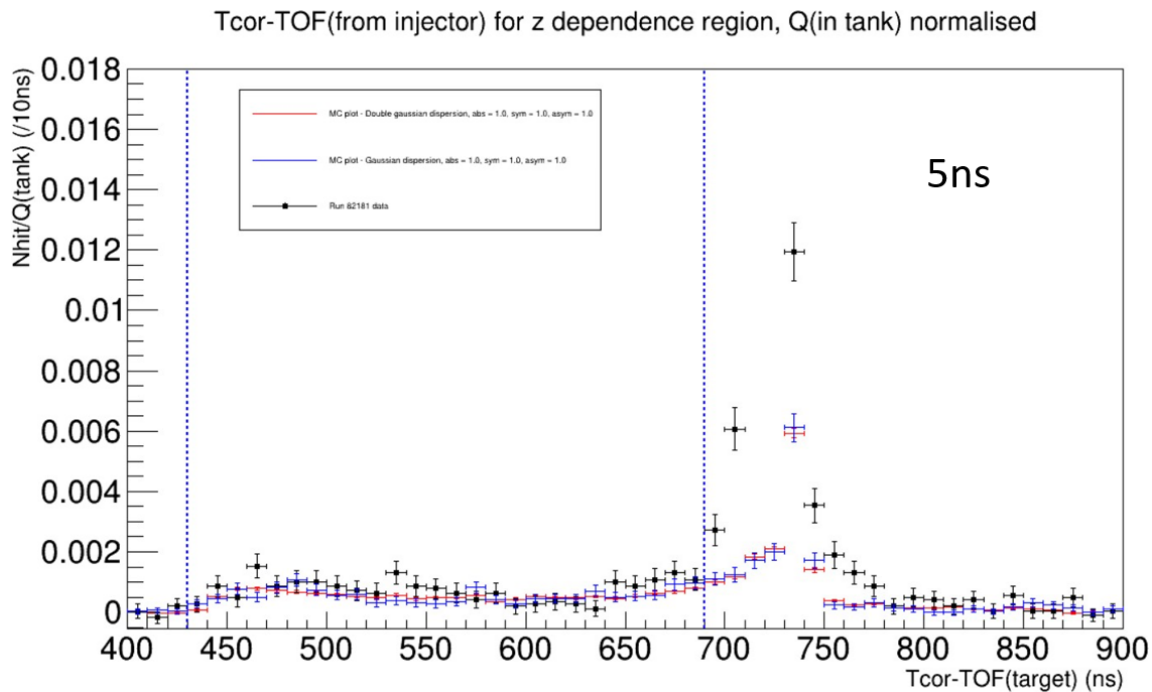


Figure 5.32: Gaussian and double gaussian time dispersion for 5ns for the B1 collimator TOF comparison between UKLI MC and Run 82181 test data

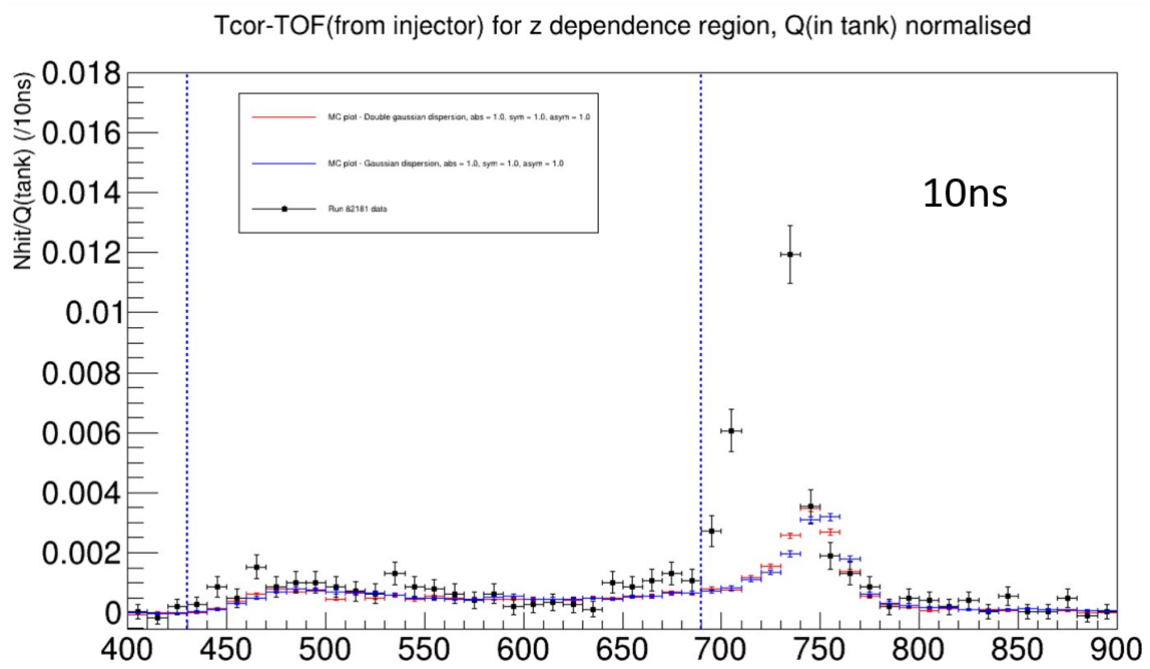


Figure 5.33: Gaussian and double gaussian time dispersion for 10ns for the B1 collimator TOF comparison between UKLI MC and Run 82181 test data

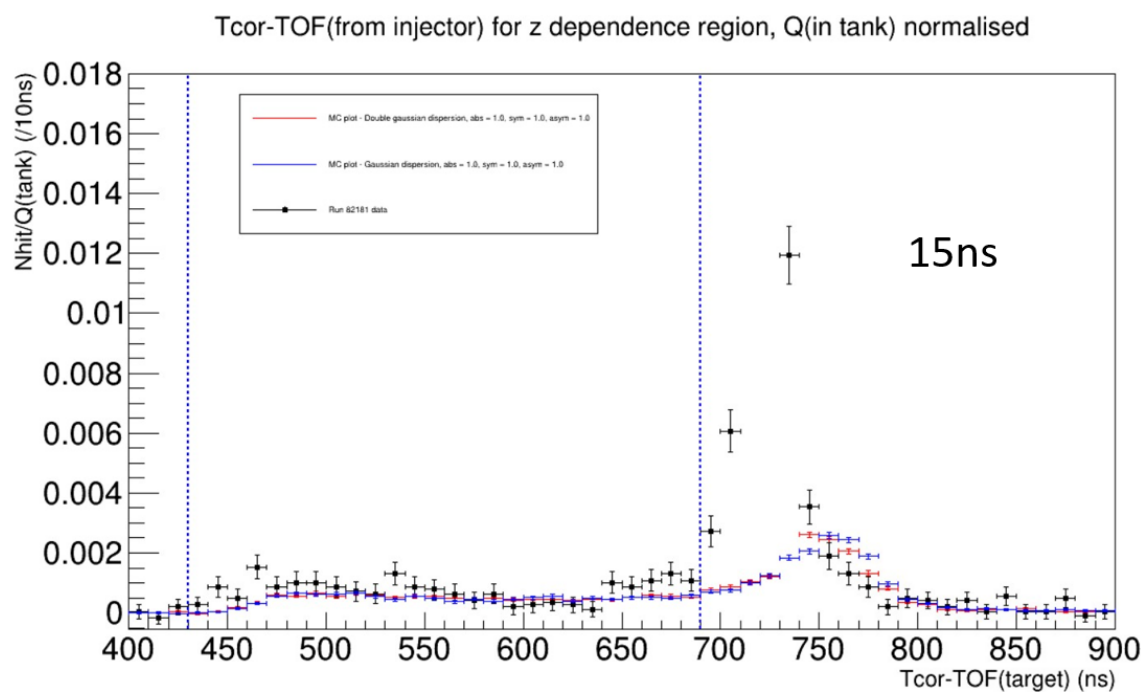


Figure 5.34: Gaussian and double gaussian time dispersion for 15ns for the B1 collimator TOF comparison between UKLI MC and Run 82181 test data

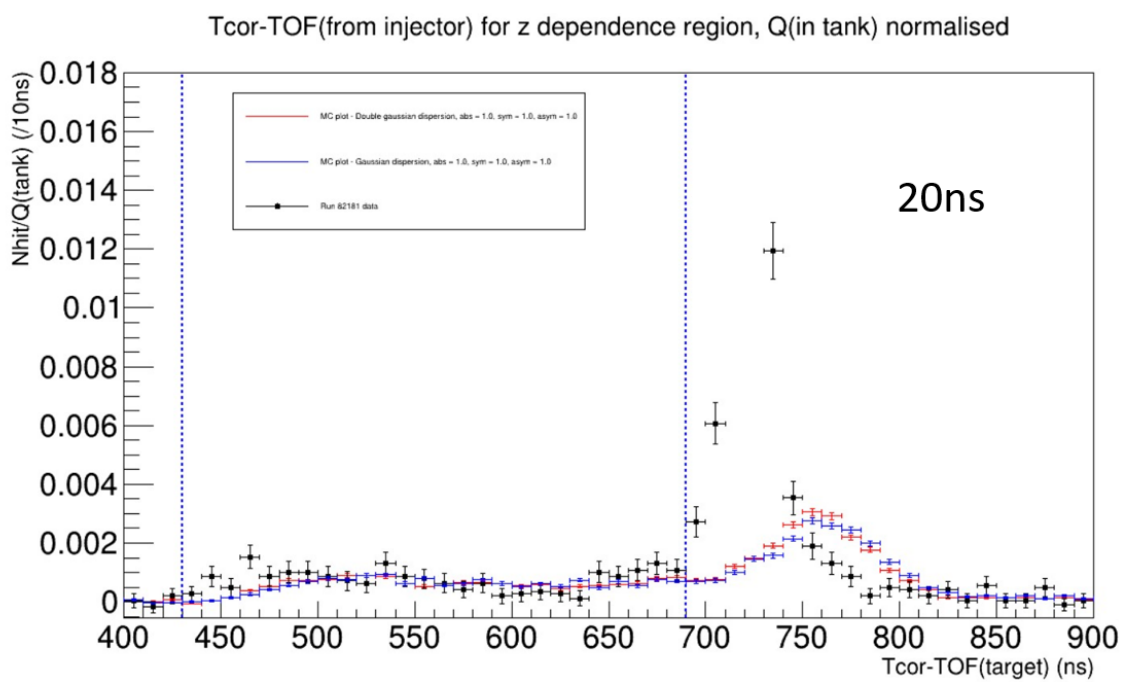
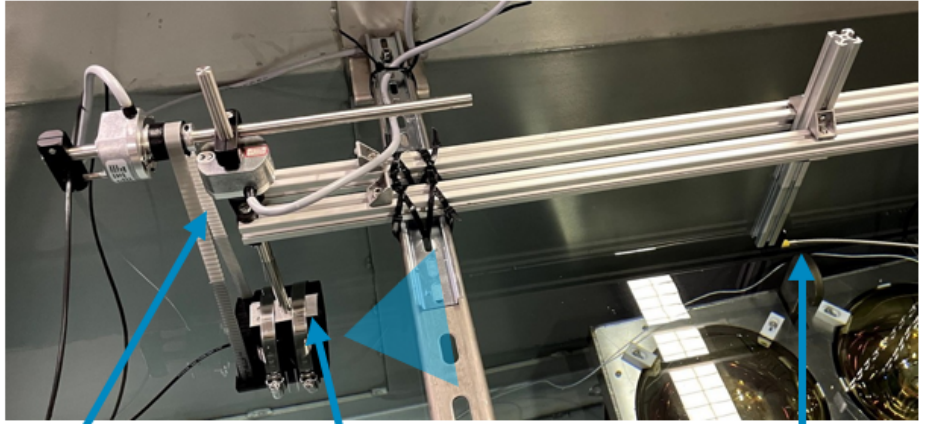


Figure 5.35: Gaussian and double gaussian time dispersion for 20ns for the B1 collimator TOF comparison between UKLI MC and Run 82181 test data



ϕ rotation about horiz. axis θ rotation about vertical axis 1.5mm dia. Fibre to optical detector

(a) Diffuser tank setup at Sheffield



(b) D5 (SK spare) diffuser

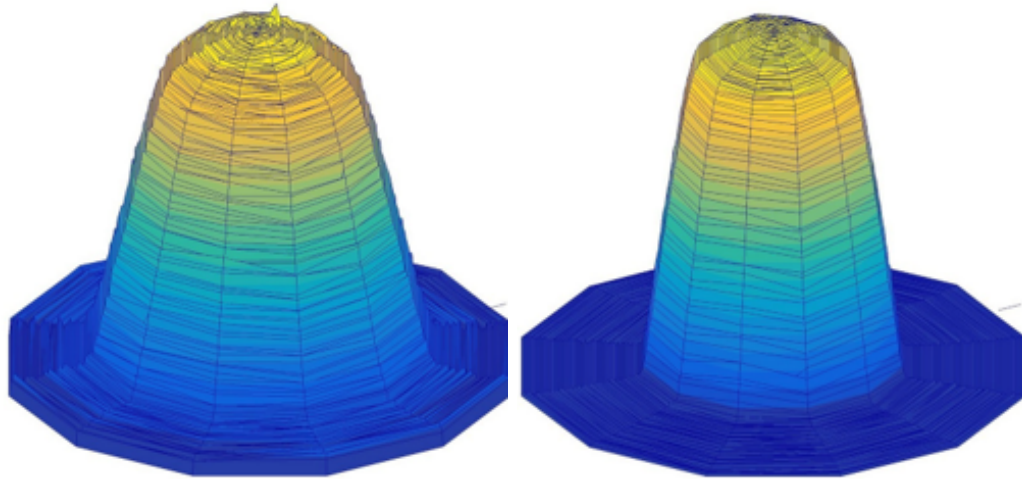


(c) HP1 (HK prototype) diffuser

5.1.2 UKLI work towards Hyper-Kamiokande

Since the first implementation of the UKLI MC, there have been several improvements made to the diffuser profiles, with a full 2π diffuser profile produced from UKLI diffusers placed in a test stand in Sheffield. There were two types of diffusers involved in creating the 2D profiles: the “D5” diffuser (and SK install spare diffuser) and “HP1”, a prototype for Hyper-Kamiokande. Profile measurements for the diffusers were made in both air and water, and Figure 5.36a shows the test stand setup at Sheffield, along with Figure 5.36b and Figure 5.36c which show the D5 and HP1 diffusers respectively.

In Figure 5.36a, not only is there a θ rotational stand about the vertical axis, there is



(a) 2D profile for the D5 diffuser in air (b) 2D profile for the D5 diffuser in water

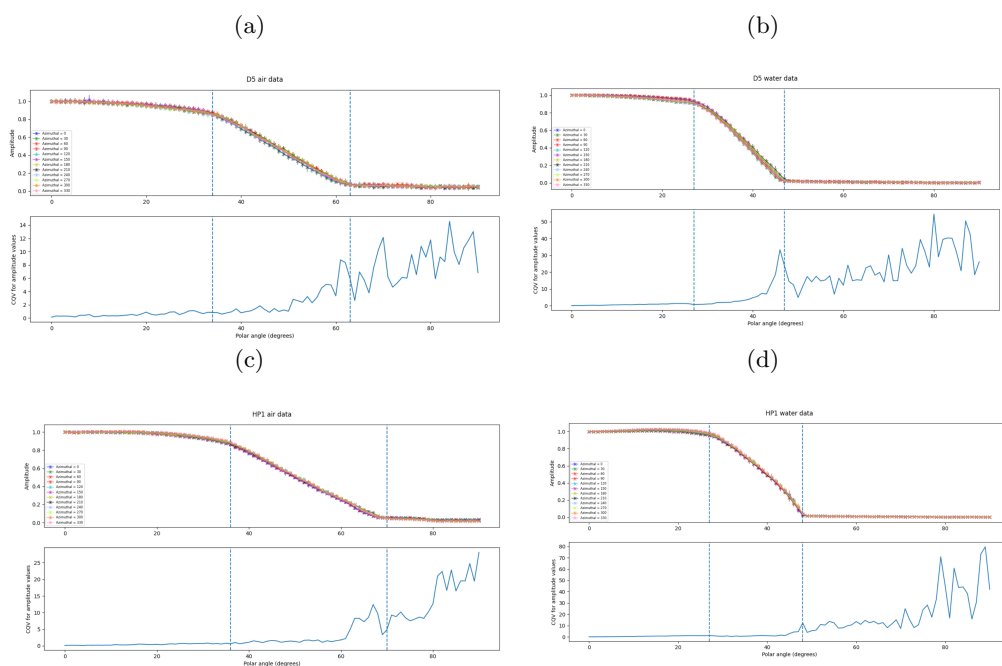
also ϕ rotation about a horizontal axis, allowing for a 2D profile instead of the 1D profiles produced by the Warwick test stand previously. Figure 5.37a and Figure 5.37b show the 2D profiles for the D5 diffuser produced in air and water, with the θ and ϕ rotations labelled.

To investigate the relationship between polar angle, azimuthal angle and the amplitude of the light, plots were made for the D5 and HP1 diffusers of the variation of amplitude vs polar angle, for measurements of azimuthal angle in 30° intervals. This would give an indication of how uniform the profile is by seeing how closely the values of amplitude for each azimuthal angle are to each other. This is shown in Figure 5.38, along with the coefficient of quartile variation (CQV) of the amplitude, to show the spread of the data and used instead of the standard deviation as a more robust measure as it will not be affected by outliers. This data is shown for both the D5 and HP1 diffusers in air and also water, with three distinct regions (shown by the dashed lines) across which the amplitude varies most.

The reason for the largest CQV values for the larger values of polar angle is due to smaller amplitude values showing more variation than for larger amplitude values if there is an inherent systematic variation stemming from measurement apparatus or dark noise in the tank.

To conclude, initial 1D light profiles for the collimator and diffuser optics from the test stand at Warwick have been put into the detector simulation and inverse transform sampling has been used to generate the output angle of the outgoing photon according

Figure 5.38: Amplitude and Amplitude CQV plotted against polar angle (in degrees) for different values of azimuthal angle in air and water for the D5 and HP1 diffusers



to the input light profile shape. This has been validated by occupancy plots and also running uniformly generated random numbers through the inverse cumulative distribution function to produce the input profile probability distribution function. In addition to this, by generating time-of-flight corrected hit time distributions, the timing region which shows the scattered hits has been adjusted to match up with test run data, by understanding how to tweak the amount of timing dispersion to have different distributions. Future work in order to implement 2D profiles have been started with the help from colleagues at Sheffield, and scans and fits to the polar and azimuthal angle have been made.

Chapter 6

Super-Kamiokande Gadolinium Upgrade

6.1 Physics motivation behind Super-Kamiokande Gadolinium Upgrade

In order to be able to observe the diffuse supernova neutrino background (DSNB) flux it was proposed that Gadolinium (Gd) should be added to the the water in Super-Kamiokande. Natural isotopes of gadolinium have large thermal neutron capture cross sections. As a result of this, when neutrons are captured on them there is a cascade of gamma rays that occurs, with an energy totalling 8 MeV, whereas neutron capture that occurs on hydrogen produces a single 2.2 MeV gamma ray. Two such natural isotopes, Gd-155 and Gd-157 have thermal neutron capture cross sections of 60740 barns and 253700 barns respectively, while the thermal neutron capture cross section of hydrogen is just 0.329 barns [26]. The Super-Kamiokande with Gadolinium experiment, formerly known as GADZOOKS! (Gadolinium Antineutrino Detector Zealously Outperforming Old Kamiokande, Super!) was proposed in 2003, which stated the intention of enriching Water Cherenkov detectors with water soluble gadolinium salt. The ultimate aim is to load a total amount of gadolinium in the form of gadolinium sulphate octahydrate ($\text{Gd}_2(\text{SO}_4)_3 \cdot 8\text{H}_2\text{O}$) in Super-Kamiokande which equates to 0.2% of Gd by mass, which would allow for 90% neutron capture efficiency. The ability to tag neutrons efficiently in Super-Kamiokande will benefit multiple physics topics, not only for the aforementioned observation of SRN flux, but also for analyses involving

atmospheric neutrinos and proton decay.

A massive amount of energy is released when a core-collapse supernova (CCSN) occurs, about 10^{46} J. The vast majority of this energy (99%) is released in the form of neutrinos, and due to neutrinos interacting with matter only very weakly, these traverse space with barely any attenuation. The interaction through which neutrino detectors such as Super-Kamiokande detect SRN flux is through inverse beta decay (IBD), shown in Equation 6.1.

$$\bar{\nu}_e + p \rightarrow n + e^+ \quad (6.1)$$

Due to the large cross section of the interaction, these events constitute about 88% of the total number of events in the detector [25]. With efficient neutron tagging in Super-Kamiokande, the backgrounds (charged current interactions and muon spallation) in the search for SRN flux neutrinos would be largely reduced. The neutral current quasielastic (NCQE) background would still remain due to the way the gamma rays arising from neutron capture mimic the signal of the inverse beta decay (IBD) reactions: a schematic of both NCQE and IBD reactions are shown in Figure 6.1. The measurement of the NCQE interactions using T2K beam flux can aid in understanding this background more due to the T2K flux peak being near the atmospheric neutrino flux peak (600 MeV).

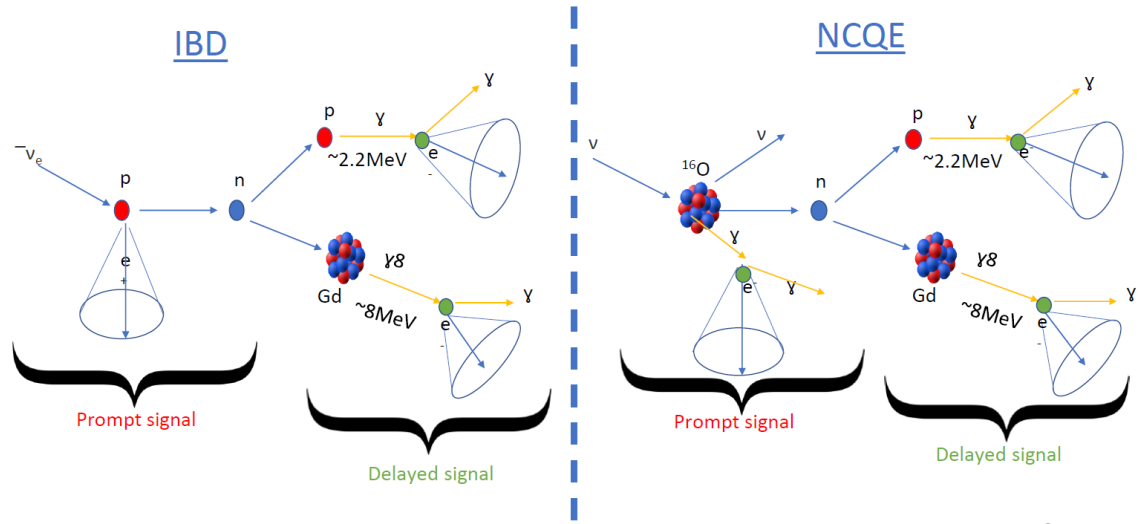


Figure 6.1: Schematic showing the IBD and NCQE interaction mechanisms

Efficient neutron tagging aids information about neutrino energy and neutrino interaction type, and when it comes to studying atmospheric neutrino oscillations, accurate neutrino energy reconstruction is particularly important. Figure 6.2 shows the fraction of non-visible energy as a function of the number of tagged neutrons from simulations of atmospheric neutrino interactions at Super-Kamiokande. Here E_ν is the energy of the atmospheric neutrino and E_{vis} is the energy that is reconstructed from charged particles. Due to these neutrinos interacting with nuclei in the detector, more neutrons are produced, and with efficient neutron tagging on gadolinium the neutrino energy can be properly reconstructed.

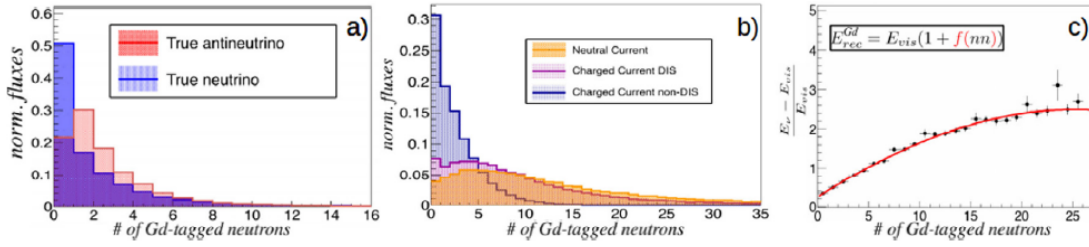


Figure 6.2: MC study of (a) neutron multiplicity production for ν and $\bar{\nu}$, (b) neutral current, charged current and deep and non-deep inelastic scattering, (c) the correction to the visible energy as a function of neutrino multiplicity. Taken from [25].

Proton decay searches benefit from the addition of gadolinium to Super-Kamiokande because the main background to proton decay analyses come from atmospheric neutrino interactions, due to Figure 6.2 showing that atmospheric neutrinos cause at least one neutron to be produced.

6.2 The EGADS project

In 2009, prior to the addition of gadolinium in Super-Kamiokande, the EGADS (Evaluating Gadolinium's Action on Detector Systems) project was used to evaluate how the inclusion of gadolinium sulphate octahydrate would affect water quality and detector components inside Super-Kamiokande and their analyses. It was also used to observe how to reduce the visible neutron background from spallation and neutrons from fission chains from the uranium and thorium impurities in the gadolinium sulphate. EGADS is a cylindrical 200 ton stainless steel tank in a cavern near Super-Kamiokande and has its own water

purification system and gadolinium sulphate octahydrate dissolving system.

Observing the impact the addition of gadolinium sulphate octahydrate had on the water quality and components was especially crucial, and after loading 0.2% gadolinium sulphate into the the EGADS tank in 2013, 240 PMTs were installed into the detector. 224 of these are the 50 cm Super-Kamiokande inner detector PMTs, with 60 of these having the same FRP and acrylic covers as the inner detector PMTs. Much like Super-Kamiokande, the active photocoverage for EGADS is 40%, with the inside walls of the detector also being covered in black polyethylene terephthalate sheets. However, unlike Super-Kamiokande, there is no outer detector in EGADS. Figure 6.3 shows the PMT map for the EGADS detector along with the PMT types. Along with the PMTs which are identical to the ones inside Super-Kamiokande, EGADS also contains PMTs which are used for research and development for use inside Hyper-Kamiokande [25].

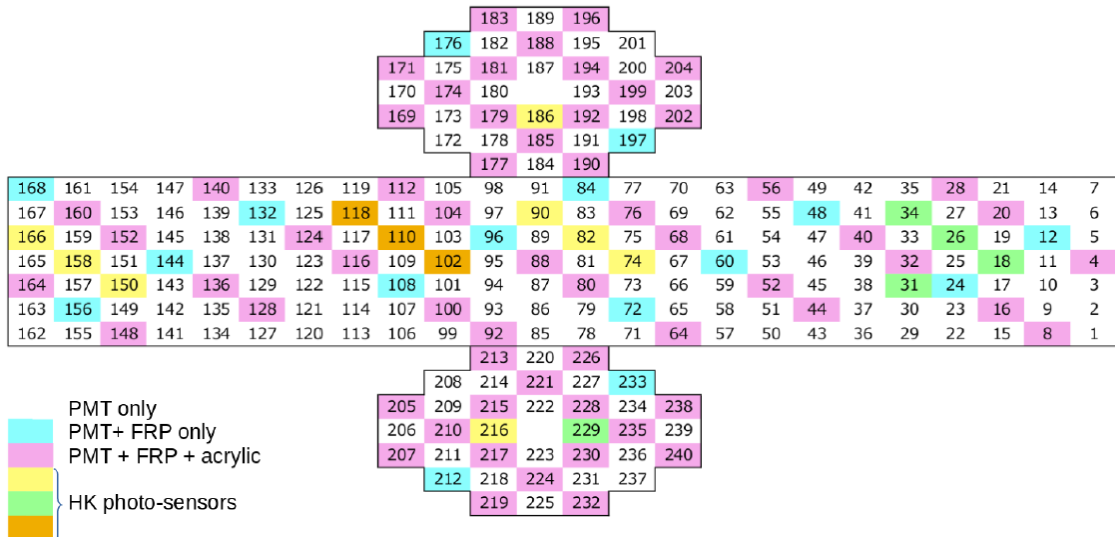


Figure 6.3: Map of unrolled cylindrical EGADS detector with PMT types. Taken from [25].

Measurements regarding neutron tagging were also taken using an Americium/Beryllium (Am/Be) source placed inside EGADS. Using an Am/Be neutron source to observe gadolinium's efficacy with respect to tagging neutrons is feasible because the Am/Be source decays as in Equation 6.2. It produces a prompt 4.4 MeV gamma ray alongside a neutron during its decay process, and as a result the prompt 4.4 MeV signal can serve as a trigger signal, while the following hundreds of microseconds can be used as a timing window within which

to scan for the neutron. Due to its similarity to the neutral current quasielastic events studied in the analysis in this thesis, it can serve as a helpful control sample and is used in the calculation of the detector response uncertainty in Chapter 7.



The delayed neutron capture time from an Am/Be source used in EGADS with the gadolinium sulphate concentration of 0.2% is shown in Figure 6.4. Here, we can see that the neutron capture time from the data is $29 \pm 0.3 \mu\text{s}$ and for the Monte Carlo it is $30 \pm 0.8 \mu\text{s}$.

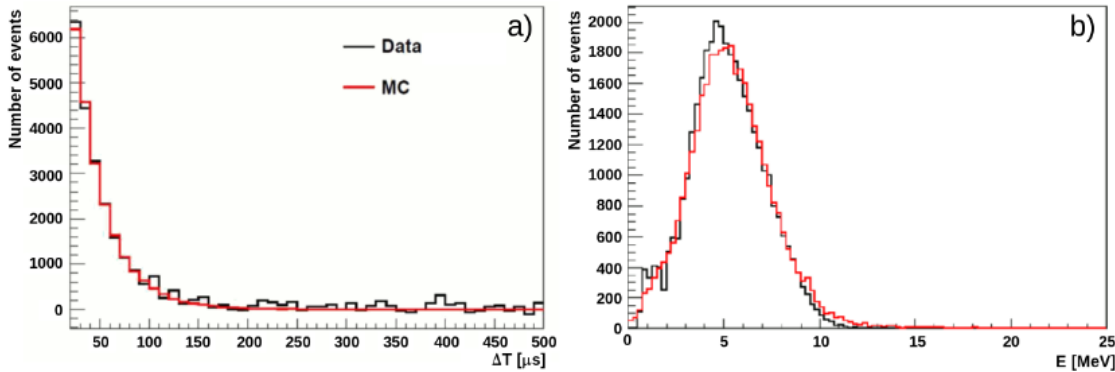


Figure 6.4: a) Delayed neutron capture time from prompt event with Am/Be source. (b) Reconstructed energy from gamma rays after neutron capture.

EGADS water transparency and gadolinium sulphate concentration was monitored daily to ensure similarity to ensure no negative effects to the detector components. Figure 6.5 shows the transparency and concentration from bottom, top and centre sampling ports in EGADS, with the blue band being typical water transparency values for Super-Kamiokande. It shows that the water transparency values remain comparable to Super-Kamiokande values and that there is very little variation from the final target gadolinium sulphate concentration, as there is little variation from the black dashed line.

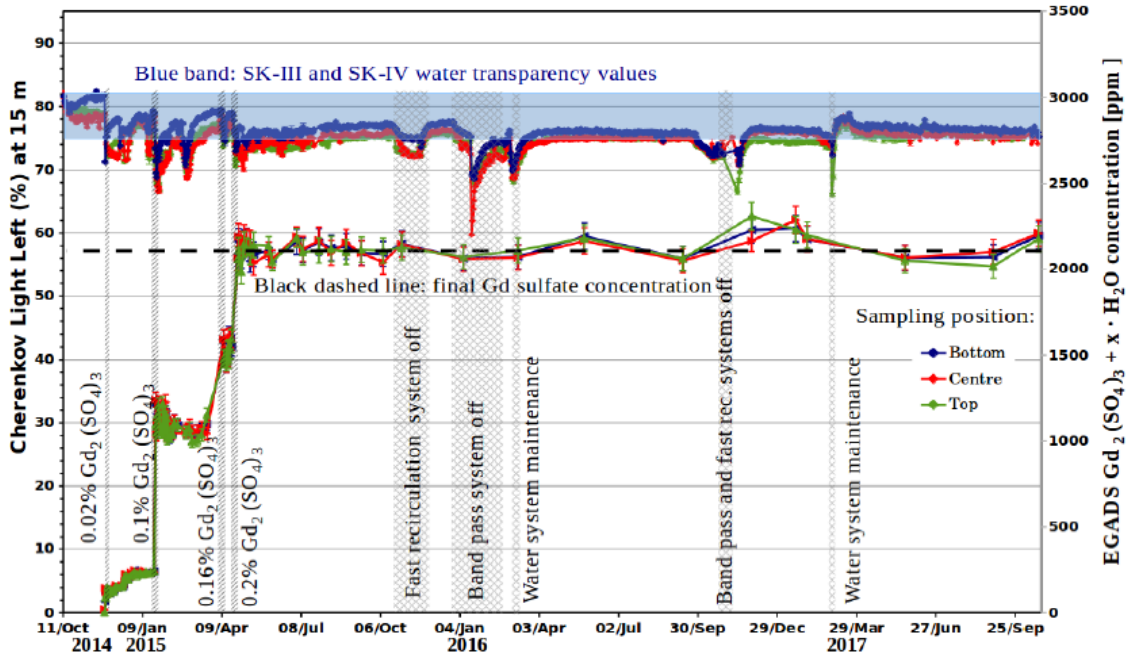


Figure 6.5: The upper lines are Cherenkov light left (%) and the lower three lines represent gadolinium sulphate concentration. The blue, red and green lines represent measurements taken from the bottom, centre and top sampling ports, respectively. Taken from [25]

EGADS also represented the most realistic possible soak test, and after two and a half years of running, EGADS was emptied in November 2017 to check the condition of the inner structure and the photomultiplier tubes. There was no deterioration of any of the components, which was an excellent sign for a detector designed to so closely resemble the conditions for the Super-Kamiokande Gadolinium upgrade.

6.3 Gadolinium loading into Super-Kamiokande

After the success of EGADS, the Super-Kamiokande Gadolinium project was formed in 2015 when the final goal of adding 0.2% gadolinium sulphate octahydrate by mass to the detector. 10% of the target concentration was then loaded into Super-Kamiokande from July 14th to August 17th 2020. The details of the various aspects of the gadolinium loading are mentioned in the next subsections: the SK-Gd water system, the flow of the water in the detector, and the loading of the gadolinium sulphate octahydrate powder.

The SK-Gd water system

The SK-Gd water system was designed to dissolve gadolinium sulphate octahydrate into the detector water, pass it through a “pretreatment” system to remove contaminants from the water, and then to continuously circulate it. Figure 6.6 shows a schematic of the system. The $\text{Gd}_2(\text{SO}_4)_3 \cdot 8\text{H}_2\text{O}$ powder is transported to a weighing hopper which dissolves it into water held in a dissolving tank, which allows for exact amounts of the powder to be dissolved to attain the specific concentration required. The water in Super-Kamiokande is fed into a solvent tank, and then to the dissolving tank, from which it receives the gadolinium sulphate octahydrate from the shear blender. Water from this dissolving tank mixes with the powder, and this combination is sent to the pretreatment system. The design for this treatment system was successfully tested in EGADS and involves treating this solution with ultraviolet light. Positively charged impurities dissolved in the solution (such as radium ions) and negatively charged impurities (such as uranium) are removed using a cation and anion exchange resins respectively. The gadolinium loaded water is next transferred to a UV steriliser to remove bacteria introduced during the dissolving process. This pretreatment process only occurs during gadolinium octahydrate sulphate dissolution, and not during the recirculation process. The recirculation process is similar to the pretreatment process, but with ultrafiltration modules installed in the final stage, and heat exchange units used before the water is returned to the detector, to help maintain exact control over the water temperature.

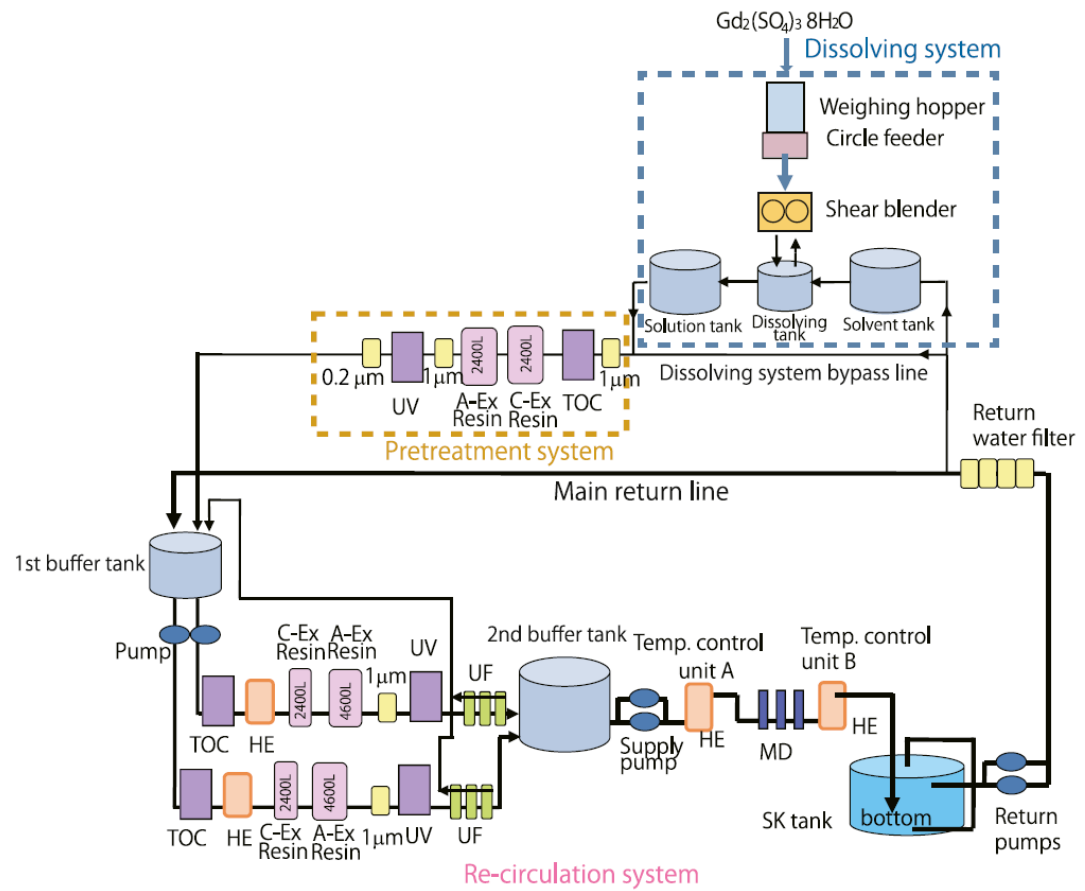


Figure 6.6: Schematic of the SK-Gd water system

Control of water parameters in SK-Gd

Before gadolinium loading occurred, the water temperature in the tank was set at 13.9 °C exactly and was circulated at this temperature for about 45 days. The temperature of the “supply water” (water sent from the water system to the detector tank) was set to a lower temperature (13.55 °C) as Gd-loading began. This gradient in the density between the tank water and supply water meant that spatial configuration of the Gd-loaded water could be observed, by taking the temperature of the water at different locations in the tank. Figure 6.7 shows a schematic of the water piping during Gd dissolving for both the inner and outer detectors.

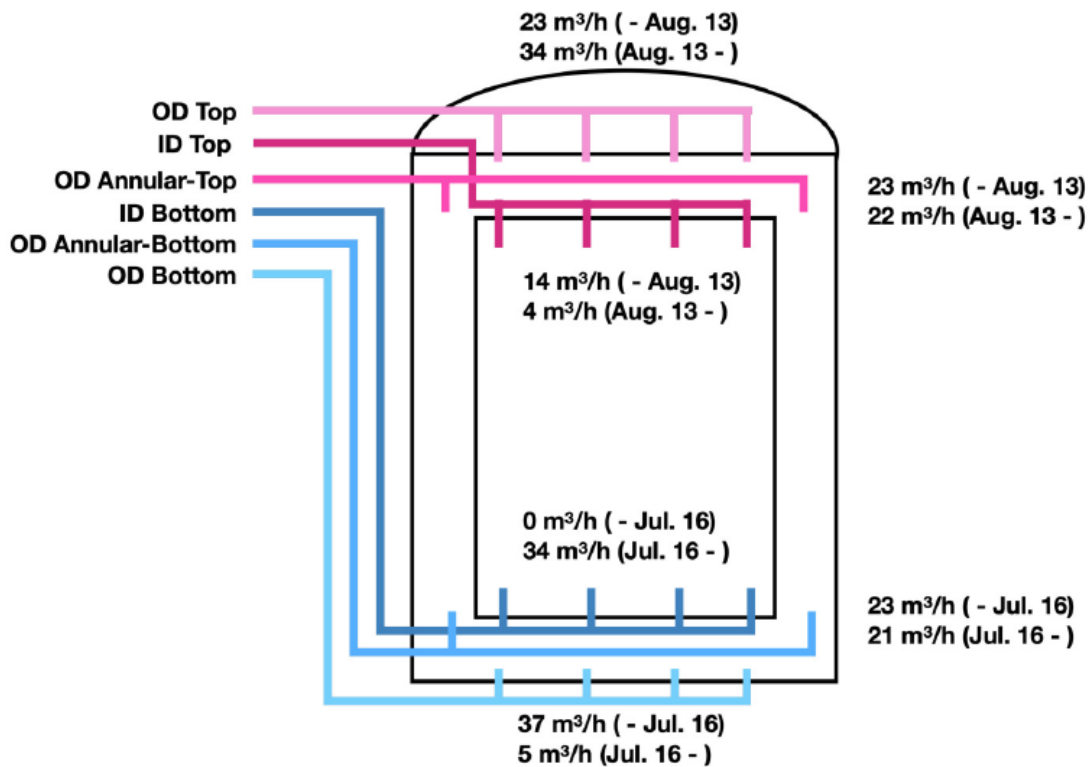


Figure 6.7: Schematic of the SK-Gd water piping for both the ID and OD

Gd-powder specification and loading

The acceptable background rate after the final value for Gd loading (set to be a concentration of 0.1% Gadolinium) was set to be less than double that of the background rate for when Super-Kamioknde ran with pure water. As a result, rigorous standards of cleanliness were set for the $\text{Gd}_2(\text{SO}_4)_3 \cdot 8\text{H}_2\text{O}$ powder, which meant setting maximum allowed levels of radioactive impurities which are shown in Table 6.1.

Chain	Isotope	Criterion [mBq/kg]	Physics target
^{238}U	^{238}U	< 5	SRN
	^{226}Ra	< 0.5	Solar
^{232}Th	^{232}Th	< 0.05	Solar
	^{228}Ra	< 0.05	Solar
^{235}U	^{235}U	< 30	Solar
	$^{227}\text{Ac}/^{227}\text{Th}$	< 30	Solar

Table 6.1: Table of impurities in the gadolinium sulphate octahydrate powder

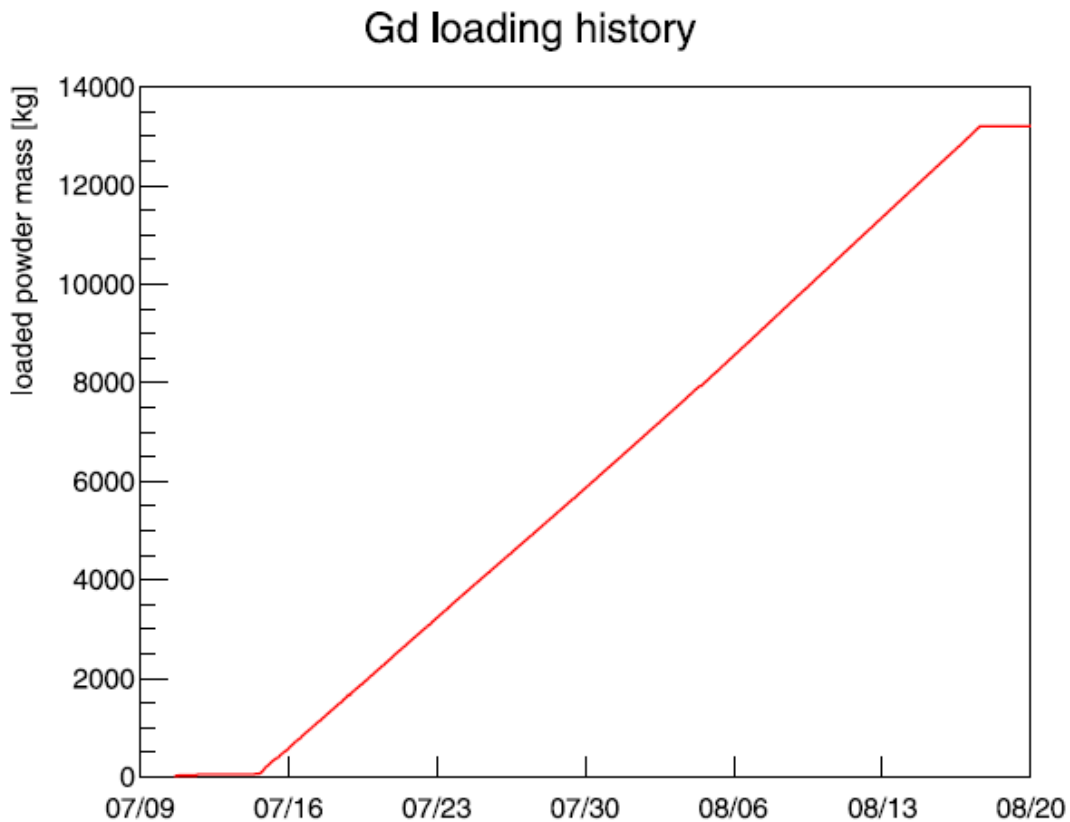


Figure 6.8: Schematic of the SK-Gd water piping for both the ID and OD

To sustain this very small level of impurity, the gadolinium powder batches went under routine screening at three collaboration laboratories at Boulby (UK), Canfranc (Spain), and the Kamioka Observatory.

Figure 6.8 shows the loaded mass of gadolinium powder in Super-Kamiokande at each dissolving cycle. The loaded mass of gadolinium sulphate octahydrate powder increased linearly until the target value of 5426 kg of it dissolved in 44,878,429 kg of water in Super-Kamiokande, resulting in a gadolinium concentration of 0.011% and a gadolinium sulphate ($\text{Gd}_2(\text{SO}_4)_3$) concentration of 0.021%. After the loading of gadolinium sulphate powder into Super-Kamiokande, water transparency and attenuation length were continuously monitored. This had also been conducted in EGADS (see previous section), but due to the flow rate of the water and method by which gadolinium is loaded into the detector being different in Super-Kamiokande, it is important to monitor these attributes in the SK-Gd upgrade as well. Figure 6.9 shows how the attenuation length of the Cherenkov light in SK-Gd varies with time: this attenuation length is measured using cosmic ray through going muons (as explained in Chapter 3). There is a clear decrease in the attenuation length after the loading of $(\text{Gd}_2(\text{SO}_4)_3 \cdot 8\text{H}_2\text{O})$, reaching a minimum of 75 m in August of 2020, and increasing again to its original pre-Gadolinium loading value of 90 m by the beginning of December 2020.

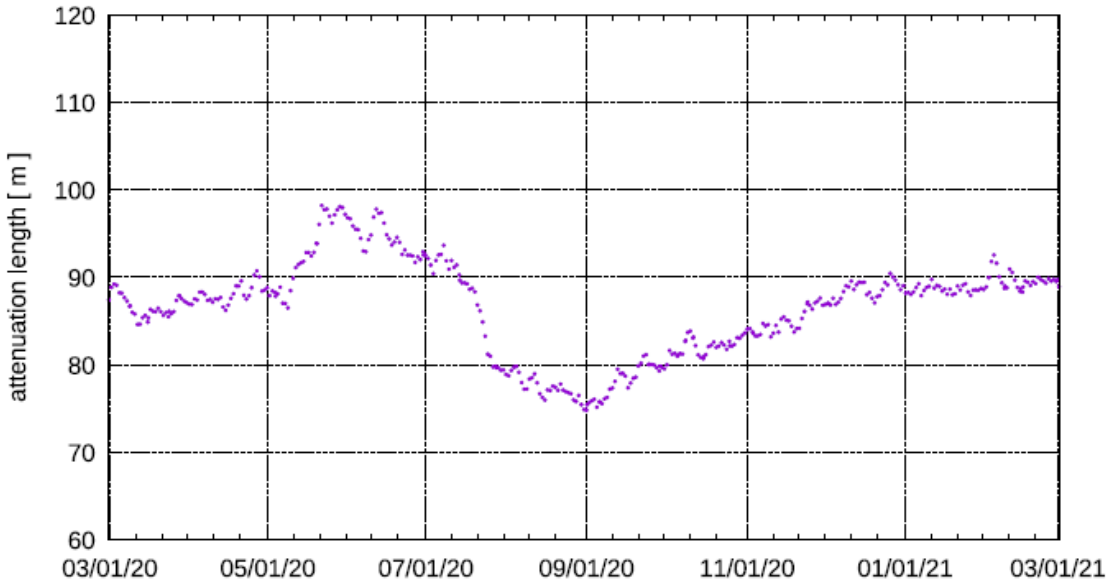


Figure 6.9: The attenuation length of Cherenkov light measured using cosmic ray muons between March of 2020 and March of 2021

There is also great importance in monitoring the concentration of the $\text{Gd}_2(\text{SO}_4)_3 \cdot 8\text{H}_2\text{O}$ in the detector - this can be done using either direct sampling via calibration ports or using the Americium/Beryllium neutron source. The first method involves using a sampling probe (a 40m long flexible plastic tube) which took samples through two ports in the inner detector and the outer detector. This probe was attached to a flow meter, a pump and a conductivity meter which comprised the sampling system. The Super-Kamiokande water conductivity is a good measure of the $\text{Gd}_2(\text{SO}_4)_3 \cdot 8\text{H}_2\text{O}$ concentration because due to the thorough water recirculation systems, all contaminants should have been removed, and all that would be measured would be the amount of the gadolinium and sulphate ions. Figure 6.10 shows the variation of the $\text{Gd}_2(\text{SO}_4)_3 \cdot 8\text{H}_2\text{O}$ concentration in the detector at different depths in the detector during various points in time in the gadolinium loading period. Figure 6.11 shows the latest $\text{Gd}_2(\text{SO}_4)_3 \cdot 8\text{H}_2\text{O}$ concentration measured using an atomic absorption spectrometer (AAS) in both the inner and outer detector. It shows that the $\text{Gd}_2(\text{SO}_4)_3 \cdot 8\text{H}_2\text{O}$ is unvarying with an average value of 271 ± 4 ppm.

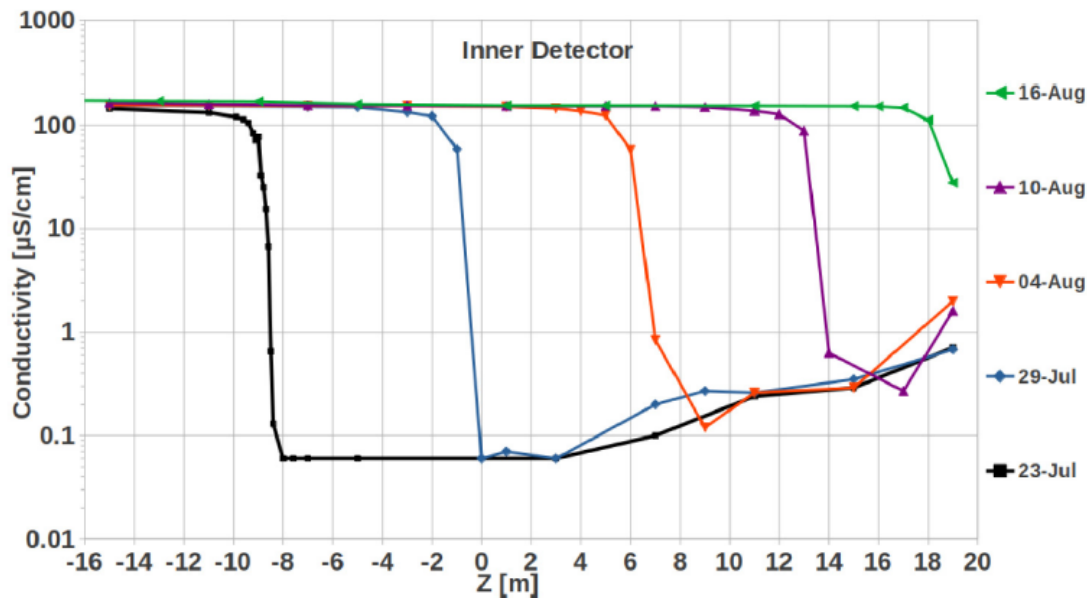


Fig. 8. Conductivity vs. Z position in the ID during Gd loading. Z=+19 m is inside the calibration guide pipe.

Figure 6.10: Conductivity vs. z position during Gd loading inside the inner detector

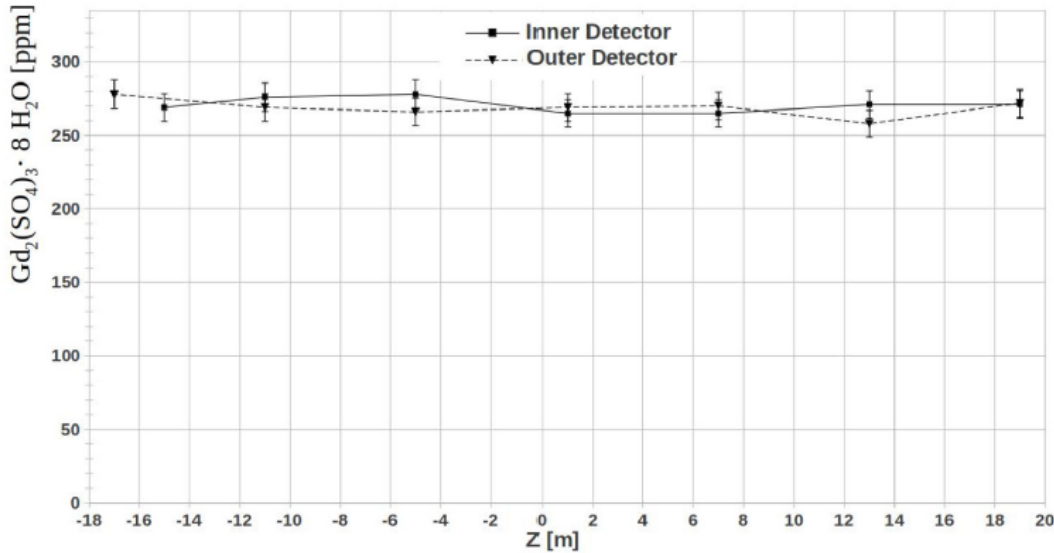


Figure 6.11: Latest gadolinium concentration measurements against z-position in the detector.

The second method of evaluating the $\text{Gd}_2(\text{SO}_4)_3 \cdot 8\text{H}_2\text{O}$ concentration is using an Am/Be source. This source was placed within a crystal cube made of bismuth germanate (BGO) and the gamma ray released by the decay of the source (shown in Equation 6.2) can be detected by the scintillation photons which pass through the BGO cube. The data was taken by placing the Am/Be source into the inner detector of Super-Kamiokande using central calibration port and then monitoring the source at three positions along the Z-axis. One in the middle of the detector ($Z=0$ m) and two at $Z = +12$ and $Z = -12$ m respectively. As mentioned in Section 2, there are specialised triggers used when looking at events, and those used specifically for looking at neutron capture events at Super-Kamiokande are the SHE (super-high-energy) and AFT (after) triggers. The SHE trigger is generated whenever there is a minimum of one photon detected within a 200 ns timing window. 35 μs after the SHE trigger is when all the photons from these neutron capture events were recorded, whereas for the AFT trigger, photons detected within a following 500 μs window were recorded. Neutron captures which happened specifically on Gadolinium were taken from this data by using a 200 ns window within which there were 30 PMTs receiving atleast one photon hit and applying event vertex reconstruction using the method outlined in Section 2. Event reconstruction parameters such as timing and hit pattern goodness (a measure of how symmetrical the Cherenkov cone hit pattern is) were used to select events. The

selected event vertex also had to be within 4 m from the Am/Be source position, the events during the SHE trigger had to be include 800 to 1300 active PMTs within $1.3 \mu\text{s}$, ensuring the selection of a 4.4 MeV gamma ray from the Am/Be source.

Figure 6.12 shows an example of the time distribution of neutron capture event candidates fit with a function. The Am/Be source position here was $Z=0$ m and the $0 \mu\text{s}$ time value on the x-axis is the time at which the scintillation photons produced by the 4.4 MeV gamma ray from its passing through the BGO cube are detected.

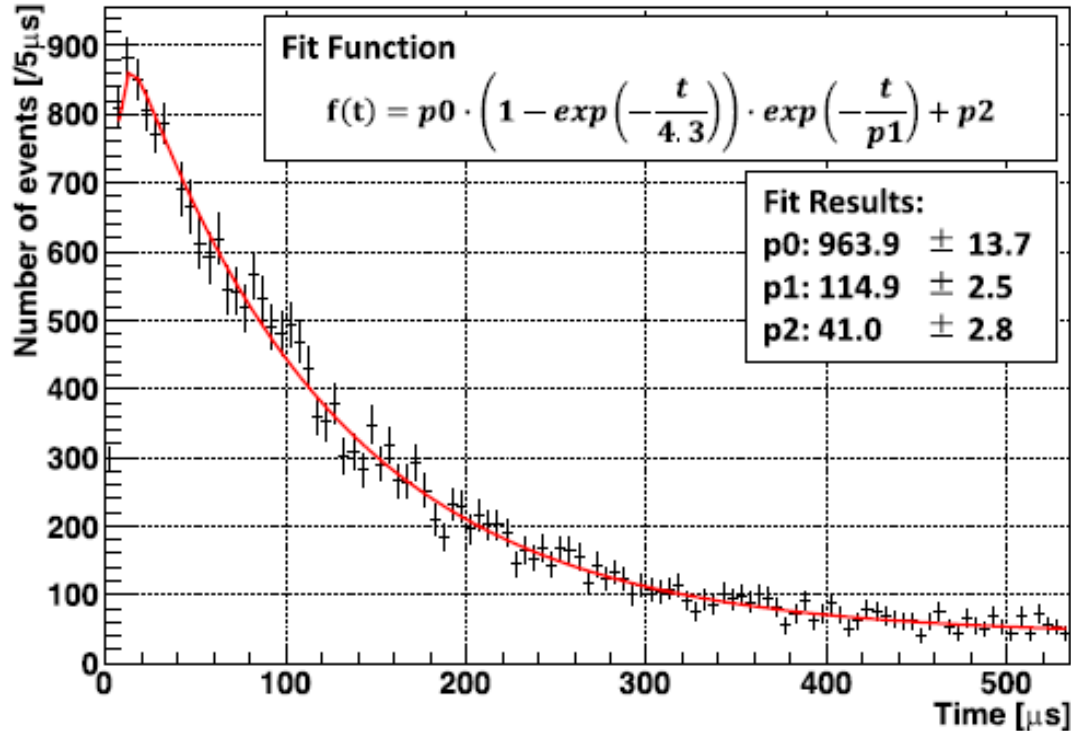


Figure 6.12: Latest gadolinium concentration measurements against z-position in the detector.

To convert the capture time of the neutron to a value for Gd concentration, GEANT4 Monte Carlo simulations were used. Figure 6.13 shows the neutron capture time constant plotted as a function of the concentration of Gd nuclei. The red points are the values from MC simulation and the black line is a polynomial function which is fitted to the red points. The horizontal blue stripe is the mean neutron capture lifetime calculated from Figure 6.12 ($115 \pm 1 \mu\text{s}$) and the vertical blue stripe is the corresponding Gadolinium concentration

value of $111 \pm 2 ppm which is consistent with the Gd concentration value of 0.011 % [6].$

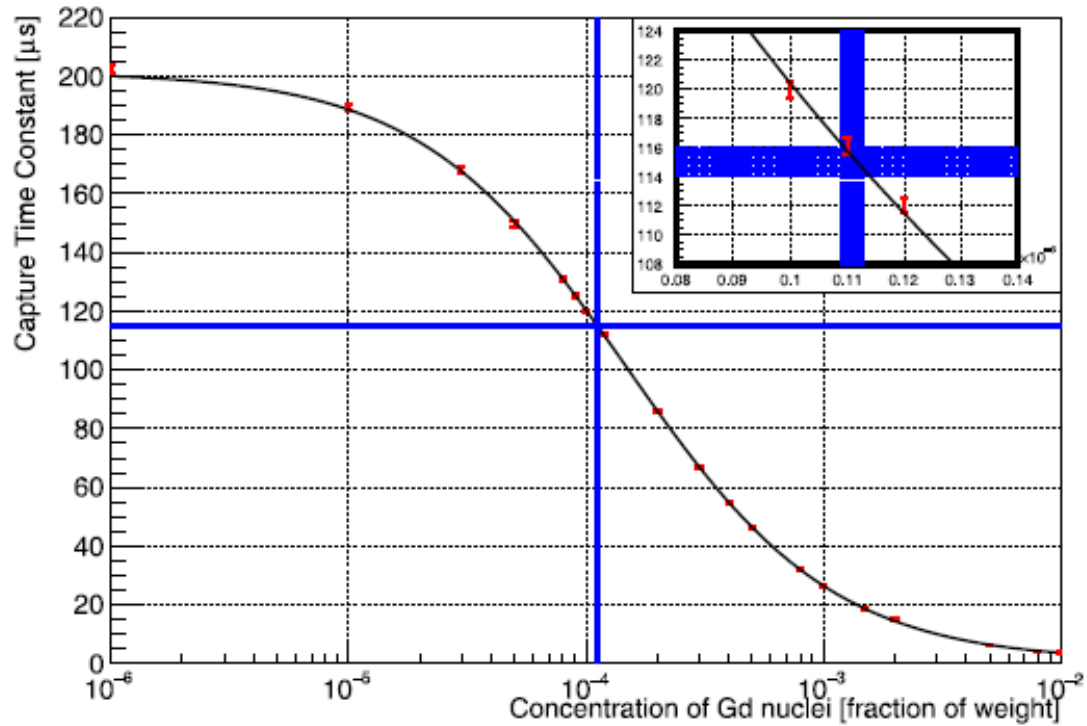


Figure 6.13: Neutron capture time constant (μs) plotted against gadolinium concentration.

Chapter 7

Measurement of Neutral Current Quasielastic Interactions with Super-Kamiokande Gadolinium Upgrade

This chapter is dedicated to the main analysis of this thesis, the motivation for which is to constrain the SRN background by looking at the atmospheric neutral current quasi-elastic (NCQE) interactions of atmospheric neutrinos which form a significant background for this SRN search, as the prompt and delayed signal of the NCQE interaction mimics that of the SRN. Previously the NCQE neutron tag has searched for the 2.2 MeV photon from neutron capture on hydrogen. With the recent addition of 0.026% gadolinium sulphate octahydrate to Super-Kamiokande, this allows for improved neutron detection due to the higher energy gamma cascade signal of neutron capture on gadolinium of 8 MeV. At energies close to the atmospheric peak, the NCQE interaction cross sections can be evaluated using T2K beam neutrinos. This analysis will present the status of the improved neutron tag from SK-Gd, its impact on the measurement of NCQE in T2K and the improvements to the SRN background measurement.

There are many stages to this analysis, which are shown in Figure 7.1, where the “neutron tagging” stage occurs via two methods. Previous NCQE neutron-tagging analyses used a method for neutron tagging which will be referred to as “legacy NTag code”, but

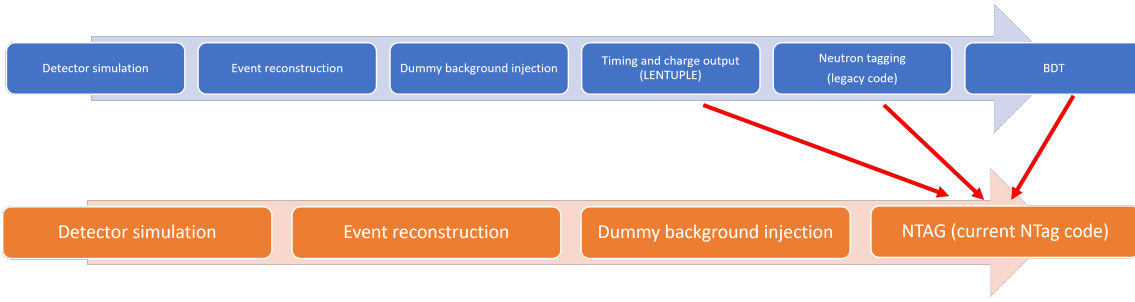


Figure 7.1: Flowchart showing the stages in this analysis for both the analysis which used the legacy Ntag code (blue) and the current NTag code (orange).

in 2020 the Super-K collaboration decided to proceed to use a new, more compact and streamlined version of the neutron tagging code, which combines most of these stages into one piece of software. This will be referred to As “current NTag code”, and this is shown in Figure 7.1 as well. The red arrows in Figure 7.1 show the steps in the analysis procedure using the legacy NTag code which have been assimilated into the new NTag code.

The main differences between the legacy and new NTag code lie in the neutron tagging algorithm stage, especially regarding variables used to classify the tagged neutron candidates which will be discussed in further detail later on. A large part of this analysis was to ensure that the legacy and new NTag code produced the same information regarding the prompt event and also for the Monte Carlo truth information regarding the neutrons.

7.1 Event Simulation

This chapter discusses details about the event simulation, specifically the software used and the way neutrino interactions are simulated in order to produce Monte Carlo. Table 7.1 summarises all the software used in this analysis.

7.1.1 Neutrino flux

The neutrino beam flux used in this analysis is 13a tuning v4.0, taken from the NA61/SHINE fixed target experiment at CERN [35]. The NA61/SHINE experiment provides hadron production measurements for T2K and other long baseline experiments, and measures the yield of charged hadrons from a proton beam fired at a thin graphite target (2 cm long) and a T2K replica graphite target (90 cm long). From this experimental data, Monte Carlo

Name	Version
Flux	13 a tuning v4.0
NEUT	5.3.3
SKDETSIM-SKGd	ANNRI-Gd model
Geant	4.10.05.p01
T2KReWeight	v1r23
GENIE	R2-12-10

Table 7.1: Software versions used in analysis

simulations of the neutrino flux are predicted. The oscillation effect on the neutrino flux needs to be considered after choosing which flux to use, and although the neutrino-oxygen NCQE cross section does not depend on flavour (and therefore neutrino oscillation affects would have no impact on a fully pure NCQE sample) there is a small amount of charged current events which seep into the NCQE sample, and oscillation weights need to be applied to the charged current events in the sample. Monte Carlo reweighting takes care of this issue by assuming that they are all muon neutrino or muon anti-neutrino events, due to the fact that the number of electron neutrino events in FHC mode would be negligible.

7.1.2 Primary interaction

The interaction between the incoming neutrino event and an Oxygen nucleus, and it's consequent de-excitation is modelled by NEUT, which produces a vector of primary particles. Because these are primary particles, they do not take into consideration all the particles produced from the detector response, i.e. the secondary particles produced from the interactions within the medium of the detector, in our case, water doped with gadolinium sulphate octahydrate. The way NEUT treats the interaction between a nucleus and a neutrino for the case of a neutrino interaction with a ^{16}O isotope is shown in Equation 7.1.

$$\sigma(\nu^{16}\text{O}) = \sum_{i=1}^8 \sigma_p(p_i^{(p)}) + \sum_{j=1}^8 \sigma_n(p_j^{(n)}) + \sigma(2p2h) \quad (7.1)$$

Here σ_p and σ_n are the neutrino-proton cross section and the neutrino-neutron cross section respectively, and these cross-sections are dependent on the momenta of the protons and neutrons in the model, and therefore on the choice on nuclear model. The Benhar Spectral Function (SF) is used by NEUT as the nuclear model for NCQE interactions, and

	$(s_{1/2})^{-1}$	$(p_{3/2})^{-1}$	$(p_{1/2})^{-1}$	others
Shell model	0.25	0.5	0.25	0
Spectral Function	0.1055	0.3515	0.158	0.385
This analysis	0.4905	0.3515	0.158	0

Table 7.2: Transition probabilities for different models and states

for CCQE interactions the Smith-Moniz relativistic Fermi Gas (RFG) model is used [10], with 2p2h interactions included for these interactions.

The lowest rung of nucleons in Figure 7.2 is the $s_{1/2}$, with $p_{3/2}$ above this level and $p_{1/2}$ above that. The protons in these rungs have removal energies of 12.1 MeV, 18.4 MeV and 42 MeV respectively, and due to neutron levels being more tightly bound, these have an extra removal of 3.24 MeV compared to their proton counterparts. The shell model is imperfect due to how it allocates the probability of ^{16}O transitioning to the possible nucleon states. In the shell model, probabilities are allocated by counting the number of nucleons in each energy level and assigning probabilities according to how many there are. In Figure 7.2 it can be seen that the $p_{3/2}$ state has double the number of nucleons compared to the $s_{1/2}$ model and therefore double the probability of transition is assigned for the $p_{3/2}$ state, and the probability of transitioning to any other state is assigned to be 0, because in the shell model they don't even exist. The Benhar Spectral Function model however is complex and is tuned using electron-nucleus scattering data. The model used in this analysis is a modified version of the Benhar Spectral Function model, where the case of other transition states is dealt with by merging the "others" state into the $s_{1/2}$ state. Table 7.2 gives the probabilities of transition to different states for different models.

7.1.3 Detector response and interactions in the detector medium

Prior analyses to this used SKDETSIM (Super-Kamiokande Detector Simulator) to simulate the trajectories of particles through the water in Super-Kamiokande and output detector response MC. This analysis uses SKDETSIM-SKGd to propagate the particles, due to the requirement of needing gadolinium sulphate present in the simulation. The particular isotopes of gadolinium used in the simulation are ^{155}Gd and ^{157}Gd due to their excellent thermal neutron capture cross sections. Table 7.3 shows the relative abundance of various gadolinium isotopes inside natural gadolinium and their associated thermal neutron capture cross sections.

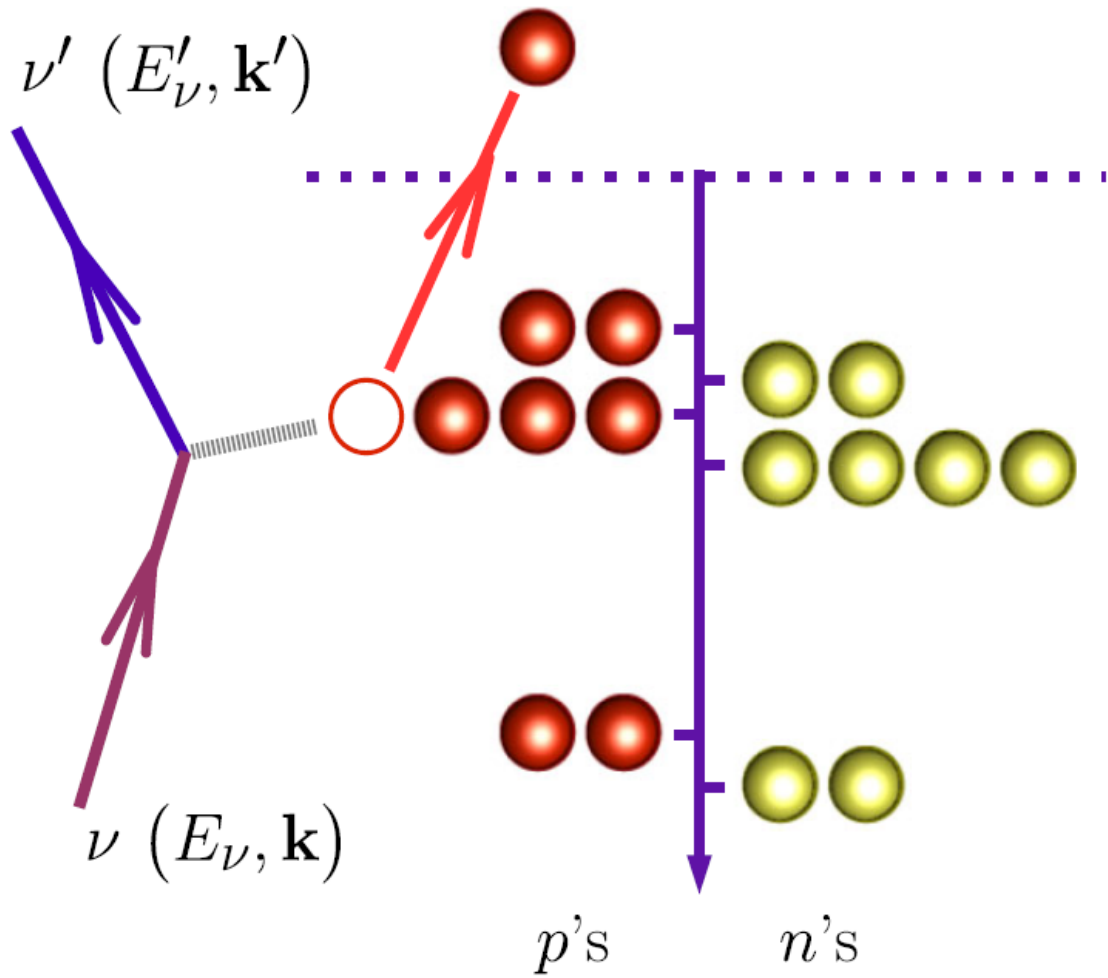
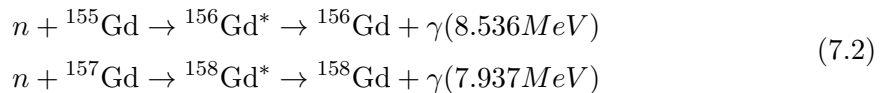


Figure 7.2: Representation of NC neutrino scattering off ^{16}O with protons on the left hand side and neutrons on the right arranged according to the shell model.

Isotope	Abundance [%]	Cross-section [b]
¹⁵² Gd	0.200	735
¹⁵⁴ Gd	2.18	85
¹⁵⁵ Gd	14.80	60900
¹⁵⁶ Gd	20.47	1.8
¹⁵⁷ Gd	15.65	254000
¹⁵⁸ Gd	24.84	2.2
¹⁶⁰ Gd	21.86	1.4

Table 7.3: Abundance and thermal neutron capture cross section of various isotopes of Gadolinium

As can be seen in Table 7.3, not only are ¹⁵⁵Gd and ¹⁵⁷Gd the most abundant isotopes, they also have extremely high neutron capture cross sections compared to the other isotopes. Equation 7.2 shows the neutron capture on both of these isotopes, and the energy of the subsequent gamma rays.



It is important to therefore model the gamma ray emission spectra from both of these isotopes. The model used by SKDETSIM-SKGd is the ANNRI-Gd model. This uses gamma energy spectrum data from the germanium spectrometer at the ANNRI (Accurate Neutron Nucleus Reaction Measurement Instrument) experiment. This experiment uses the incoming pulsed neutron beam from the Japan Spallation Neutron Source (JSNS) at the Material and Life Science Experimental Facility (MLF) of J-PARC. After a 300 kW beam of protons from the JSNS facility hits a target of mercury and produces neutrons, this neutron beam hits an enriched ¹⁵⁵Gd target or a *nat*Gd film. The ANNRI spectrometer is placed 21.5 m away from the neutron beam source, with two cluster detectors on either side of the neutron capture target material, which is 13.4 cm away from each cluster detector. Surrounding the target, there are also 8 co-axial germanium detectors. The schematic for the ANNRI-Gd experiment is shown in Figure 7.3.

By defining how many Germanium crystals were hit and how many neighbouring crystal received gamma ray hits, values of H (hit number) and M (multiplicity) can be assigned in order to classify the events. After selecting for neutron energy and subtracting the background, the events remaining were separated into samples based on their H and M

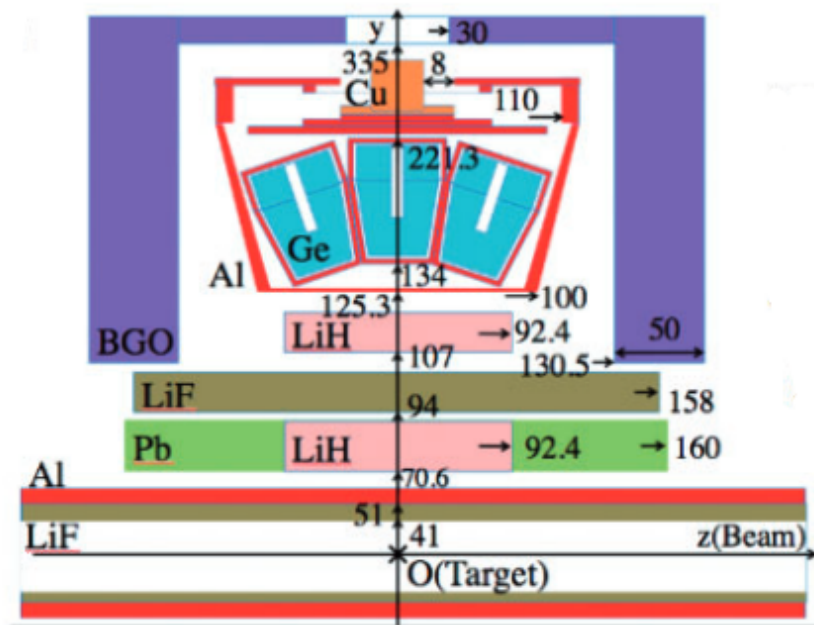


Figure 7.3: Schematic of the ANNRI Ge spectrometer (dimensions in mm). The beam pipe along with one of the Ge cluster detectors (light blue) is shown. The shaded purple area are the anti-coincidence shields made of bismuth-germanium-oxide (BGO) crystals.

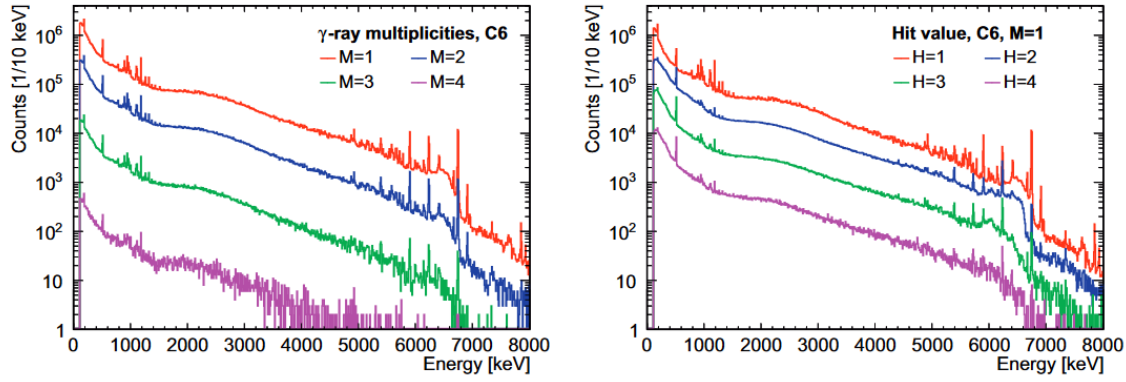


Figure 7.4: Energy spectra for thermal neutron capture on ^{157}Gd energy spectra for different multiplicity values (left) and hit values (right) from one of the germanium crystals in the ANNRI spectrometer.

vales. Figure 7.4 shows the energy spectra for different multiplicity values (left) and hit values (right) from one of the germanium crystals in the ANNRI spectrometer.

One of the key differences between the default Geant4 model for thermal neutron capture on Gadolinium and the ANNRI-Gd model is how it conserves energy: the photon evaporation model conserves only the final sum of energy for the captured event, but performs poorly when modelling the gamma-ray energy on an individual event by event basis. One way the ANNRI-Gd model combats this is by separately describing the continuous and discrete peaks in Figure 7.4, where the discrete peaks are shown as spikes below 1500 keV and above 4500 keV. These come from the different ways in which gadolinium de-excites after thermal neutron capture. The continuous spectrum in the plots in Figure 7.4 show the de-excitation of $^{158}\text{Gd}^*$ in multiple steps, producing multiple low energy gamma rays, which accounts for about 93% of the spectrum. The discrete spikes in the spectra come from a two-step cascade, which produces a high energy gamma ray instead, accounting for the remaining 7% of the spectrum. Figure 7.5 shows the continuous and discrete components of the ANNRI-Gd MC, along with data from the experiment. Figure 7.6 shows ratio plot of data and MC for the GLG4sim model, the default Geant4 photon evaporation model and the ANNRI-Gd model: here it is clear the ANNRI-Gd model fits the data better than the other two models, especially at energies above 3500 keV.

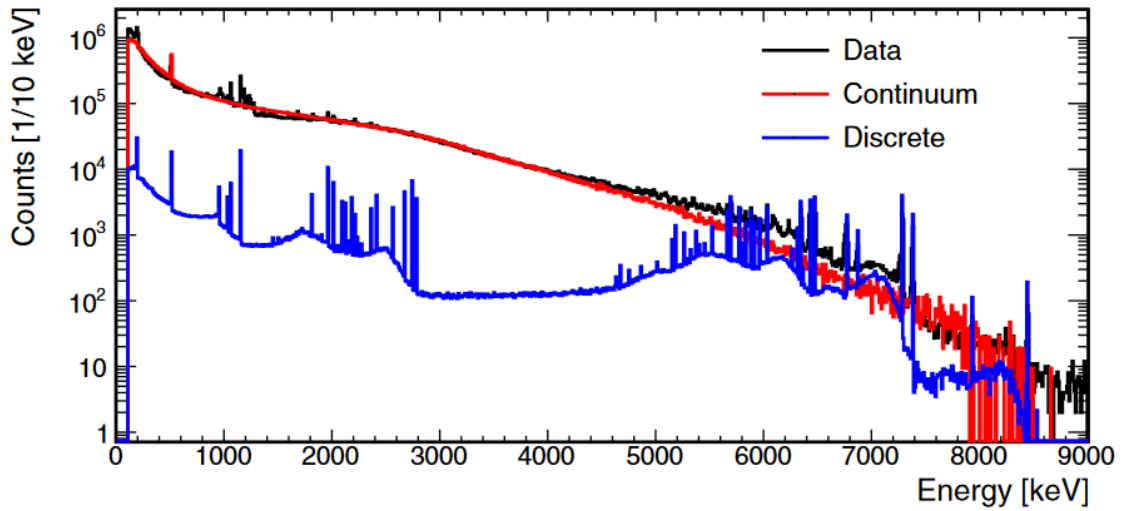


Figure 7.5: Energy spectra for the ANNRI-Gd model broken down into its continuous and discrete components along with data from the ANNRI-Gd experiment.

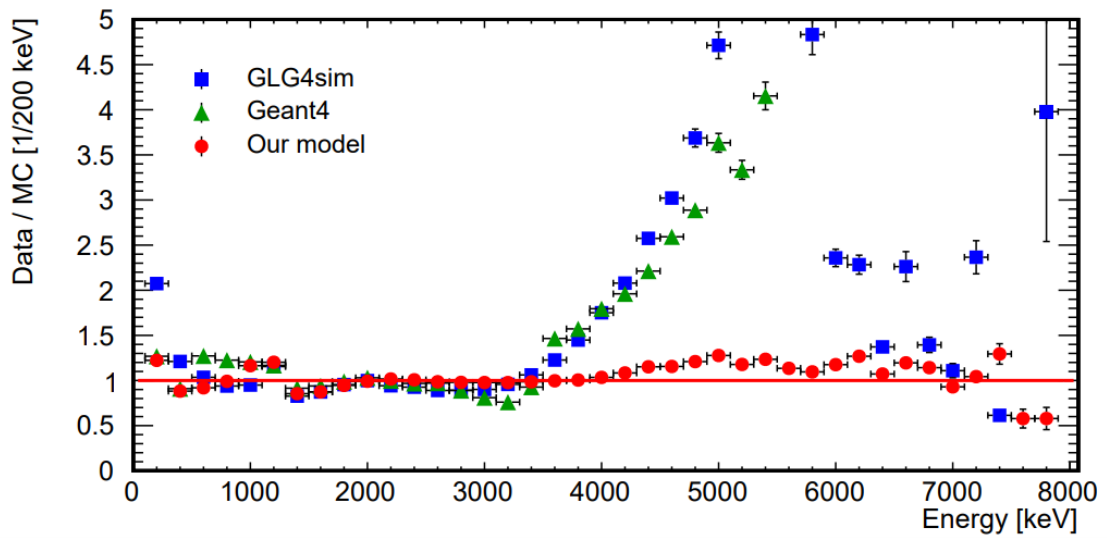


Figure 7.6: Comparison between neutron capture MC models and data.

7.2 Event Reconstruction

7.2.1 Bonsai output reconstruction quantities

Due to this analysis looking specifically at the low energy region, a fitter specific to low energies (called LOWFIT) is used to reconstruct events. Both MC and data neutrino events undergo a reconstruction phase, where the low-energy fitter BONSAI is applied to the event, which is discussed in Chapter 2. This reconstruction is carried out using timing and cable information, however charge information is omitted. The ouput of BONSAI gives information which will be used in the reduction phase of the data and allow for the selection of the NCQE sample. The following quantities comprise the BONSAI output, the first two being helpful spectator variables and the latter five constituting parameters which are used in the reduction phase of the analysis, from which the neutrino NCQE sample is determined.

1. Neutrino vertex direction

This vector points towards the direction which is an average over all the Cherenkov cone axes which are produced, due to there being multiple leptons induced in the interaction.

2. Neutrino vertex position

The reconstructed location of the neutrino interaction event.

3. Reconstructed energy

In line with the standard SK low energy analysis definition, this energy is simply the reconstructed energy with the 0.511 MeV electron mass omitted. The range for Erec in this variable is 3.49 MeV to 29.49 MeV - the estimated kinetic energy under the hypothesis that the event is a singular electron.

4. Dwall

This variable gives the minimum distance of the neutrino vertex position from the closest wall of the Super-Kamiokande detector.

5. Effwall

Thus variable gives the distance between the neutrino vertex position and the closest wall, but moving back from the vertex position along the neutrino vertex direction vector.

6. Vertex direction and goodness coefficient

The coefficient $ovaQ$ (defined in Equation 7.3) describes the quality of the vertex reconstruction. It consists of two parameters g_{vtx}^2 and g_{dir}^2 where the former describes the

goodness of the vertex which is based on PMT hit timings, and increases the sharper an event is in time. The latter is the directional goodness and measures the azimuthal uniformity in the ring pattern produced by the Cherenkov cone, which decreases the more uniform an event is in space. As a result of this, $ovaQ$ increases the more uniform and sharp in time an event is.

$$ova\ Q = g_{vtx}^2 - g_{dir}^2 \quad (7.3)$$

g_{vtx} is calculated using a fit of the PMT timing distribution and using the hit times of the PMT it is defined as in Equation 7.4.

$$g_{vtx} = \frac{\sum_i w_i e^{-\frac{1}{2}(\frac{\Delta t_i}{\sigma})^2}}{\sum_i w_i} \text{ with } w_i = -\frac{1}{2}(\frac{\Delta t_i}{\omega})^2 \quad (7.4)$$

Here $\sum_i w_i$ is the weight given to the i-th hit PMT for the reduction of dark noise, where ω has a value of 60ns. σ has a value of 5ns which is used to test the goodness, and as a result, a sharp timing distribution produces a large vertex goodness. g_{dir} is calculated by looking at how spatially uniform the hit PMTs are around the reconstructed neutrino vertex direction. In order to quantify this uniformity, the Kolmogorov-Smirnov (KS) test is used as in Equation 7.5.

$$g_{dir} = \frac{\max_i \{\angle_{uni}(i) - \angle_{data}(i)\} - \min_i \{\angle_{uni}(i) - \angle_{data}(i)\}}{2\pi} \quad (7.5)$$

where $\angle_{data}(i)$ is the azimuthal angle of i-th hit real PMT included in the number of hits in 50ns. $\angle_{uni}(i) = 2\pi i / N_{50}$ is the azimuthal angle of the i-th virtual PMT hit, but only when uniform distribution of the hits is assumed. As the uniformity of the hit pattern increases, the goodness decreases.

7. Cherenkov angle θ_C

For relativistic electrons in water, the value of the Cherenkov opening angle is $\approx 41^\circ$, due to the relation:

$$\cos \theta_{Cherenkov} = \frac{1}{n\beta} \quad (7.6)$$

where $\beta = v/c \approx 1$ and n is the refractive index of water, 1.33. However due to other particles in the simulation, such as protons or muons, the Cherenkov cone is expected to be narrower, or if multiple leptons are present, the Cherenkov cones will be less distinct

and more spread out, leading to deviations from the 41° value.

7.2.2 Comparison of BONSAI reconstruction output variables between SKDETSIM versions

The BONSAI reconstruction output variables were compared between three versions of SKDETSIM, the version used in the previous NCQE neutron capture on hydrogen only analysis, with no neutron capture on Gd implemented (black), the SKDETSIM-SKGd photon-evaporation model mentioned in the previous section (red), and the SKDETSIM SK-Gd ANNRI-Gd model (green). Figure 7.7 shows the comparison of these models for the output BONSAI variables Erec, dwall, effwall, ovaQ, and θ_C , where the y-axis shows the number of events.

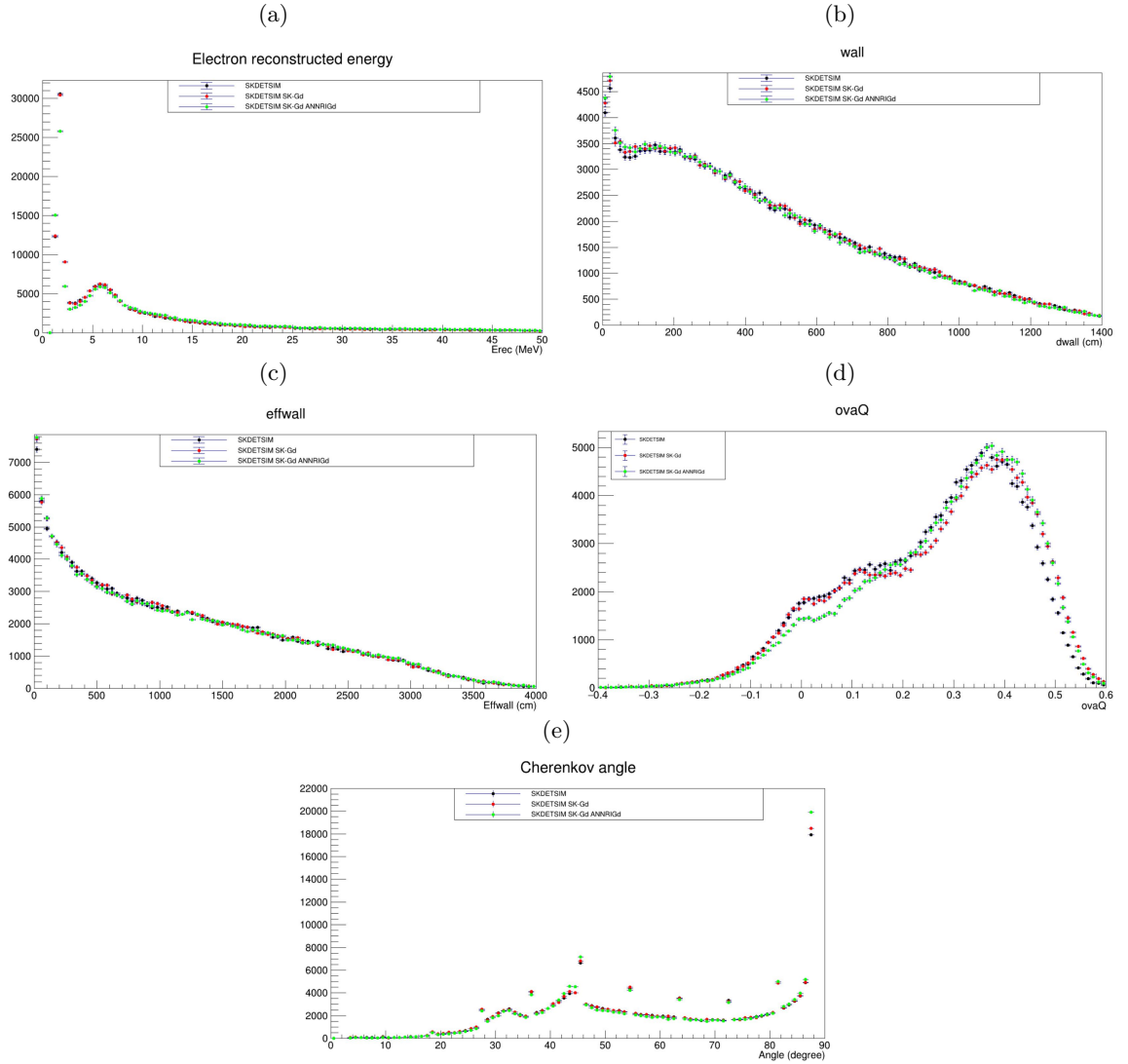
To ensure correct implementation of the ANNRI-Gd model, ensuring the BONSAI output variables were similar between these SKDETSIM versions was important as the Gadolinium model should only effect the neutron capture in the simulation, not the output from event reconstruction of the neutrino interaction vertex. As can be seen in Figure 7.7, this holds true for Erec, dwall, effwall and θ_C , but not for the vertex and goodness coefficient ovaQ, where the ANNRI-Gd model differs for ovaQ between -0.05 and 0.15 compared to the SKDETSIM and SKDETSIM photon-evaporation model. To investigate this difference further, distributions of the vertex goodness and the directional goodness which make up ovaQ (according to Equation 7.3) were also checked, shown in Figure 7.8.

The vertex goodness (gvtx) and directional goodness (gdir) squared comparisons are shown in Figures 7.8 and 7.8. Figure 7.8 shows a slight discrepancy between the SKDETSIM versions, but not enough to warrant further investigation. In addition to checking the previous BONSAI reduction phase quantities, the distance between the true neutrino vertex from the simulation and the neutrino vertex from the BONSAI reconstruction was also checked for the different SKDETSIM versions, shown in Figure 7.9. Table 7.4 shows the value of this distribution which encompasses 1-sigma (68%) of the number of events: this value was very similar for all SKDETSIM versions.

Comparisons of event reconstruction output between NTag versions

To ensure that the NCQE event selection and neutron tagging could be carried out using the new NTag code, comparisons of the output BONSAI reconstruction variables between the two versions were made to ensure the validity of the reconstruction output. Figures

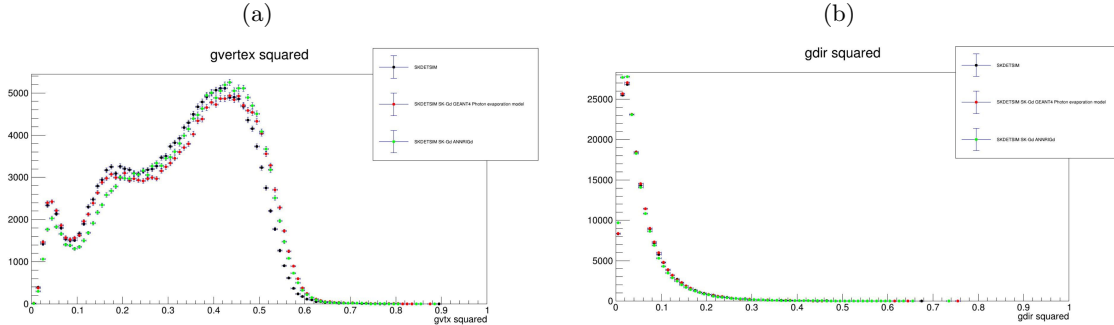
Figure 7.7: Comparisons of BONSAI output variables between SKDETSIM versions



SKDETSIM version	Value (cm)
SKDETSIM-V	113.2
SKDETSIM-SKGd (Photon evaporation model)	109.4
SKDETSIM-SKGd (ANNRI-Gd model)	111.9

Table 7.4: Value of the true neutrino vertex - reconstructed neutrino vertex distribution which encompasses 1-sigma (68%) of the number of events.

Figure 7.8: Comparisons of vertex goodness and directional goodness between SKDETSIM versions



Distance between true and reconstructed vertex

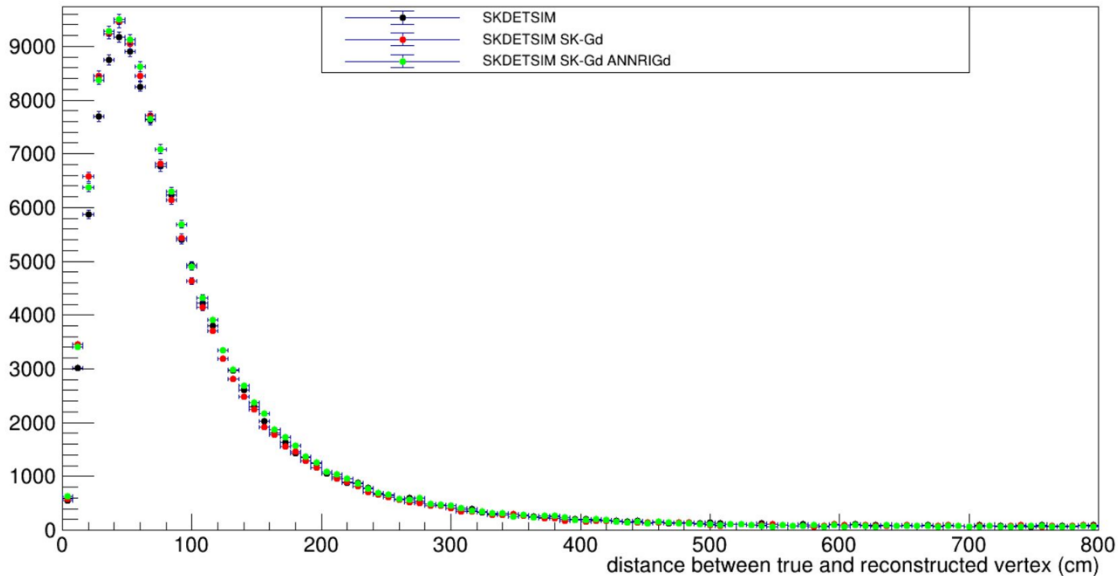


Figure 7.9: Distance between true and reconstructed neutrino vertex for different SKDETSIM versions

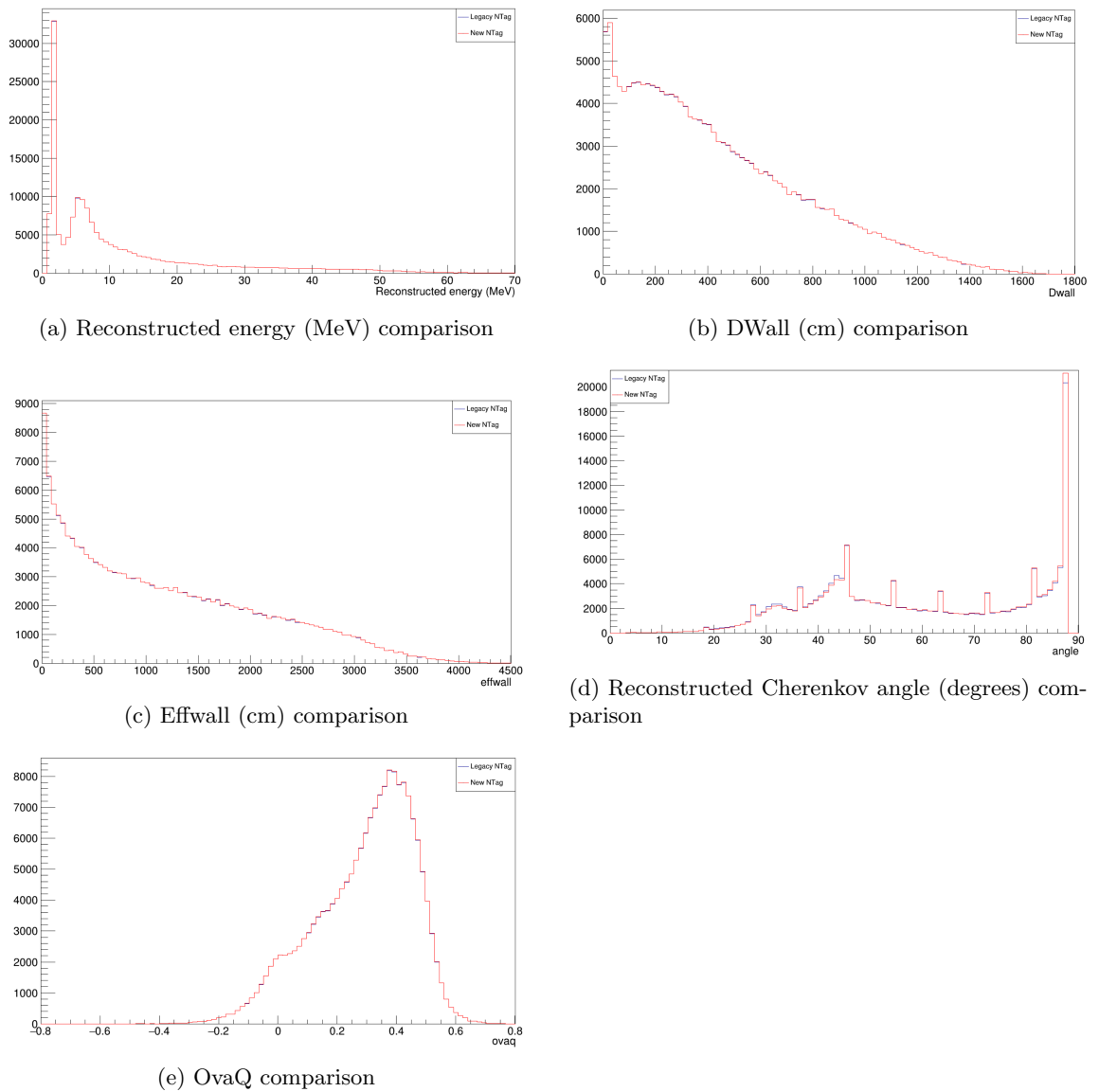


Figure 7.10: Comparison of the output between the two NTag codes showing legacy (black) and new (red) NTag outputs

[7.10a](#), [7.10b](#), [7.10c](#), [7.10d](#), [7.10e](#) show the reconstructed energy, dwall, effwall, Cherenkov angle and ovaQ parameters respectively, with the legacy NTag output in black and the new NTag output in red.

7.2.3 NCQE event selection

Prior to applying the neutron tagging algorithm which searches for neutron candidates, events which satisfy the neutral current quasi-elastic criteria need to be selected. This selection only involves the neutrino vertex information, no information about the neutron candidates is used in the NCQE selection process.

The following cuts are applied to the Monte Carlo, in order to select the NCQE events. These include a visible energy cut, a fiducial volume cut, a low energy background cut, and a cut to exclude charged current interaction events (CCQE).

Visible energy cut

The energy window for this analysis is set to the 3.49-29.49 MeV range, where the lower value of this range (3.49 MeV) is due to the detection threshold of Super-Kamiokande. In order to limit the background of the Michel electron from charged-current interactions involving muon neutrinos and muon anti-neutrinos, the upper energy window limit is set to 29.49 MeV - above this value the Michel electron background would increase, reducing the NCQE contribution.

Fiducial Volume (FV) cut

Due to radioactive impurities inside the detector material, specifically the wall of the inner detector, there is a cut involving the distance from the detector wall to the prompt interaction vertex. Events where the distance between the prompt interaction vertex and the detector wall is less than 200 cm are removed. There is a similar cut also used where events where the distance between the prompt interaction vertex and the distance to the inner detector wall in the neutrino vertex vector direction is less than 200 cm is removed. This is a standard cut applied in all Super-Kamiokande analyses in order to avoid backgrounds, and when you have events where the energy region is below 6 MeV even more stringent cuts are required to further reduce background from the inner detector wall, described in the next Subsection.

Low energy background cut

The variables dwall, effwall and ovaQ are used to tune cuts in the energy region below 6 MeV. There are five energy regions with a width of 0.5 MeV used between the lower end

of the visible energy cut region (3.49 MeV) and 5.99 MeV where the cuts on the dwall, effwall and ovaQ variables are optimised. Cuts are applied on the dwall, effwall and ovaQ variables and an event is only accepted if the values of dwall, effwall and ovaQ are only accepted if their values are greater than the threshold cut values. In each 0.5 MeV energy interval, these threshold values are optimised based on the T2K run period due to the beam power and detector conditions being different from run to run, especially since the Gadolinium loading occurred in the detector. Equation 7.7 shows how the figure-of-merit (FOM) value is to be maximised for the optimisation of each cut.

$$\text{FOM} = \frac{N_{\text{sig}}}{\sqrt{N_{\text{sig}} + N_{\text{bkg}}}} \quad \left(N_{\text{bkg}} = N_{\text{bkg}}^{\text{MC}} + N_{\text{bkg}}^{\text{beam-unrelated}} \right) \quad (7.7)$$

Here N_{sig} is the number of NCQE neutrino events in the FHC Monte Carlo sample and N_{bkg} is the summation of the background events, and the FOM is calculated separately in the five energy intervals, and the optimised cut value is taken as the one which maximises the FOM. Then the optimised cut values in each energy interval are fitted with a linear function dependent on the visible energy variables (Erec). Equation 7.10 gives the relation of Erec to the optimised cut values for dwall, effwall and ovaQ.

$$\text{dwall}^{\text{CUT}} = p_0^{\text{dwall}} + p_1^{\text{dwall}} \times E_{\text{rec}} \quad (7.8)$$

$$\text{effwall}^{\text{CUT}} = p_0^{\text{effwall}} + p_1^{\text{effwall}} \times E_{\text{rec}} \quad (7.9)$$

$$\text{ova Q}^{\text{CUT}} = p_0^{\text{ovaQ}} + p_1^{\text{ovaQ}} \times E_{\text{rec}} \quad (7.10)$$

The scan regions and intervals for the dwall, effwall and ovaQ parameters for Equation 7.10 are given in [2].

7.2.4 Charged current event (CC) interaction cut

In order to reduce the number of charged-current events which may be mistakenly included in the NCQE selection, a cut regarding the reconstructed Cherenkov angle of the prompt event is also utilised alongside the low energy background cut, where the accepted Cherenkov angle of a prompt event (θ_C) should be greater than the threshold cut value θ_C^{CUT} where the cut value is determined by the linear equation dependent on Erec as shown in Equation 7.11.

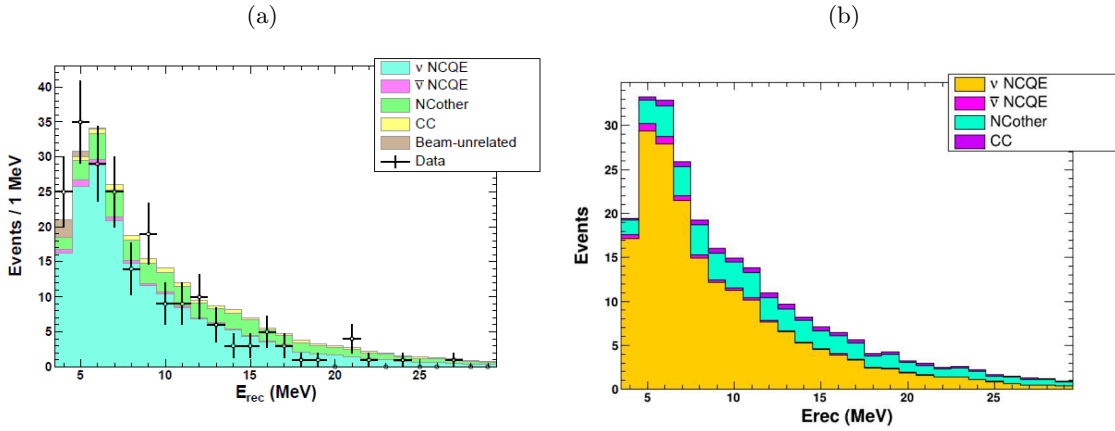
$$\theta_C^{CUT} = p_0^{\theta_C} + p_1^{\theta_C} \times E_{\text{rec}} \quad (7.11)$$

Just like for the low energy background cut values, the values of the optimised parameters in Equation 7.11 are given in [2].

7.2.5 Prompt event NCQE reduction cut plots

Before applying the NTag algorithm, either legacy or new, plots were produced of the number of neutrino events and their dependence the reduction cut variables mentioned previously. These are shown in Figures 7.11, 7.12, 7.13, 7.14, 7.15. Each figure shows the corresponding plot for the previous NCQE analysis carried out with neutron tagging on Hydrogen on the left, with the plot from this analysis on the right.

Figure 7.11: Comparisons of stacked histograms for the Erec variable between NCQE neutron tag on H analysis (left) and this analysis (right)



7.2.6 Background injection

Low energy backgrounds play a big role in this analysis because of the captures on neutrons including neutron capture on Hydrogen producing a 2.2 MeV energy signal. The two main sources of background in this analysis come from environmental radioactivity and PMT dark noise. The signal hits are mixed in with the dark noise hits and stem from the PMTs themselves, with no dependence on individual PMTs meaning that the distribution of dark noise in the detector is expected to be uniform. A Poisson distribution represents

Figure 7.12: Comparisons of stacked histograms for the Dwall variable between NCQE neutron tag on H analysis (left) and this analysis (right)

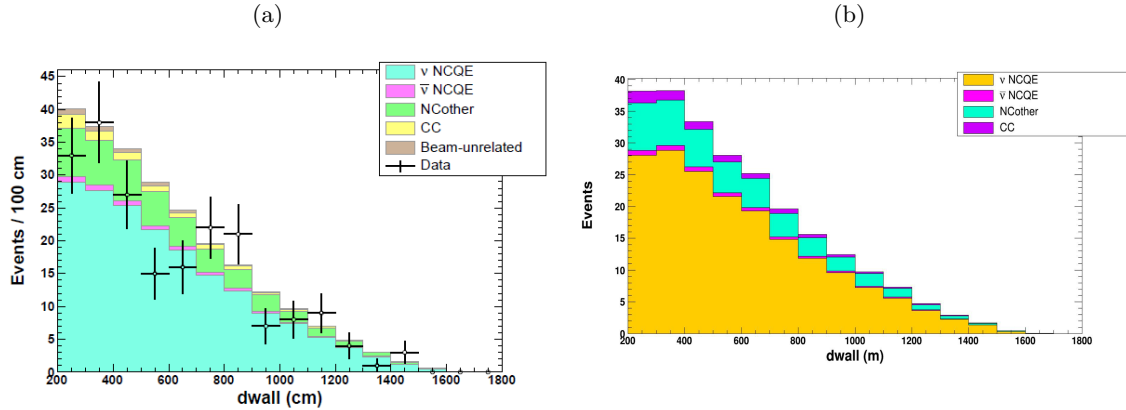


Figure 7.13: Comparisons of stacked histograms for the Effwall variable between NCQE neutron tag on H analysis (left) and this analysis (right)

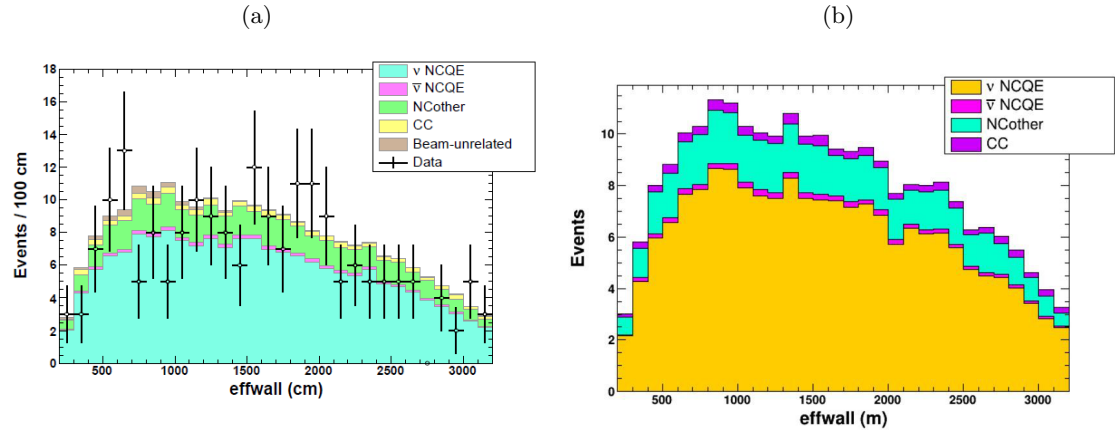


Figure 7.14: Comparisons of stacked histograms for the ovaQ variable between NCQE neutron tag on H analysis (left) and this analysis (right)

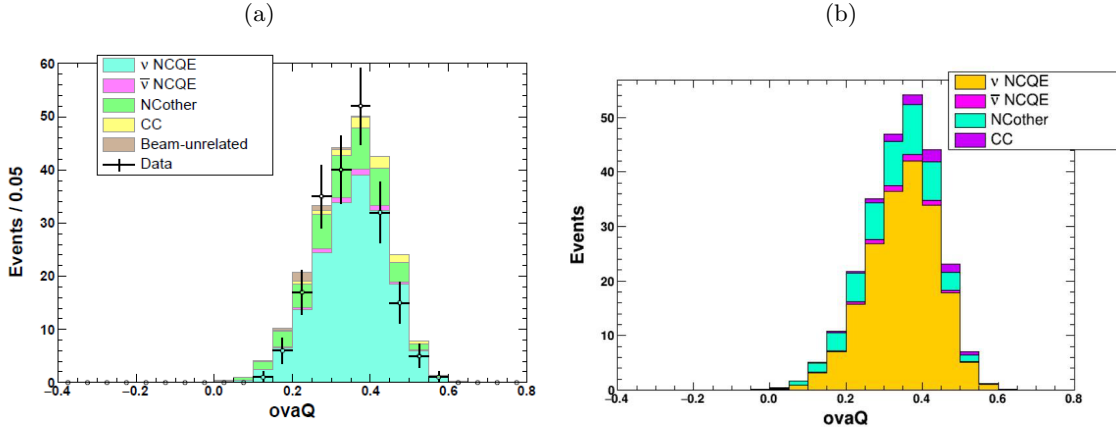
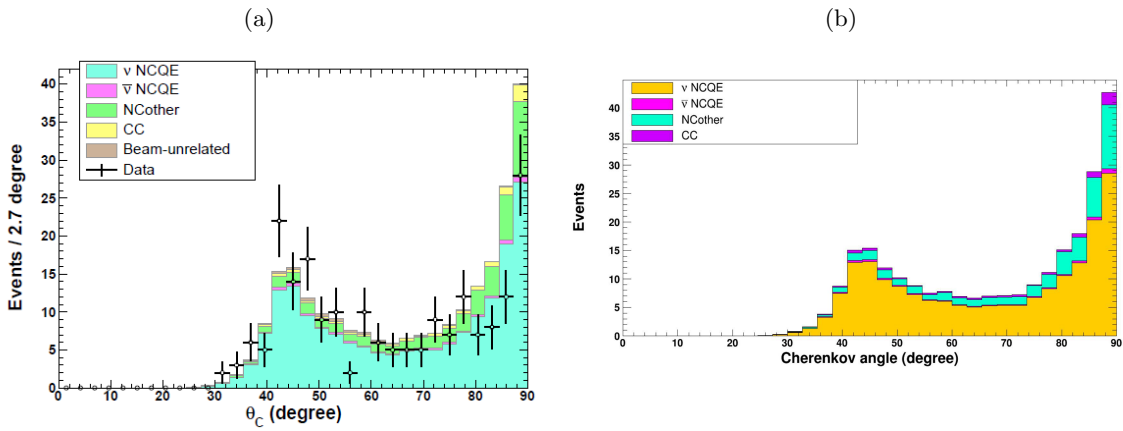


Figure 7.15: Comparisons of stacked histograms for the θ_C variable between NCQE neutron tag on H analysis (left) and this analysis (right)



the dark noise for the PMTs in the detector, and therefore the mean value of dark noise hits $\langle \#DN \rangle$ in a time window of T nanoseconds for the total number of inner detector PMTs, N_{ID} , where the dark noise rate of one PMT averaged over an entire inner detector is $\langle \text{dark} \rangle$ is given in Equation 7.12.

$$\begin{aligned}\langle \#DN \rangle &= \langle \text{dark} \rangle \times T \times N_{ID} \\ &= 10.0 \frac{\text{kHz}}{\text{PMT}} \times 14\text{nsec} \times 11,146\text{PMT} = 1.56\end{aligned}\quad (7.12)$$

The previous NCQE analysis with solely neutron capture occurring on Hydrogen used a $T = 10$ nsec timing window for the neutron capture search (the criteria for which will be detailed in the next section) and a $\langle \text{dark} \rangle$ rate of 5.0 kHz per PMT. However since the addition of gadolinium sulphate octahydrate in the detector medium, the dark rate per PMT has doubled and to accommodate for neutron captures occurring on the gadolinium the neutron capture hit search window has been increased to 14 nsec.

The dark noise hits from natural radioactivity comes from unstable isotopes from the detector material, PMT covers, the Tyvek lining the tank and the rock from the cavern which Super-Kamiokande resides in. These decaying unstable isotopes can produce enough hits to produce a signal that looks like a neutron capture on Hydrogen, meaning that these hits from natural radioactivity could also get mixed in with the hits in the 14 nsec neutron search timing window. Simulating this combination of dark noise and radioactivity in the tagged neutron candidate search window is not trivial, and therefore it is far easier to inject actual background data into the neutron search window. This background data is collected in the form of “dummy spills” which are events which are taken during periods where the T2K beam is switched off, i.e. events in between T2K runs. The neutron tagging window in this analysis starts at 18 microseconds after the reconstructed time of the prompt neutrino interaction, and therefore for each event dummy spill data is injected after 18 microseconds, while before this time the background hits are just simulated in SKDETSIM, with a certain dark rate value. Figure 7.16 shows a schematic of how and when in the analysis dark rate is simulated and injected.

The reason for the neutron tagging algorithm starting at 18 μs is in order to take into account the afterpulsing of PMTs, which occurs between 12 μs and 18 μs and creates a slight increase in the hit rate, shown in Figure 7.17, taken from []. The falling exponential to the left of the after-pulsing peak is caused by decay electrons.

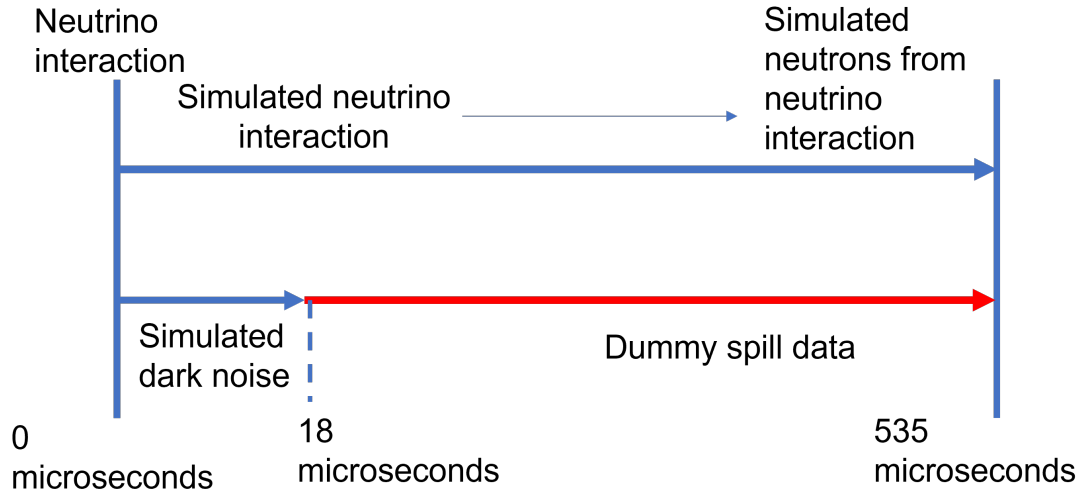


Figure 7.16: Schematic of how dark noise is simulated in this analysis.

7.3 NTag algorithm

As mentioned previously, two neutron tagging algorithms were used in this analysis, the legacy NTag code, used in previous NCQE analyses and modified to work with a version of SKDETSIM which has Gadolinium included and new NTag code which uses a slightly different neutron tagging algorithm specifically with regards to the primary and secondary selection criteria which will be discussed in later subsections.

7.3.1 True neutron tagging information

Prior to defining the primary and secondary selection criteria for each neutron tagging algorithm, it is important to produce some distributions of basic variables regarding the neutron capture that occur in the simulation, such as neutron capture time, position and number. Figure 7.18a, 7.18b show the distribution for the number of neutron captures and the true capture time of the neutrons for both the legacy (green) and new (red) NTag code.

In order to classify the neutron captures on hydrogen and gadolinium separately, the energy of the gammas produced from the neutron capture were used, along with the number of gammas produced from the neutron capture. If the energy of the gamma produced is 2.22 MeV and only one gamma ray was produced from the neutron capture, the neutron

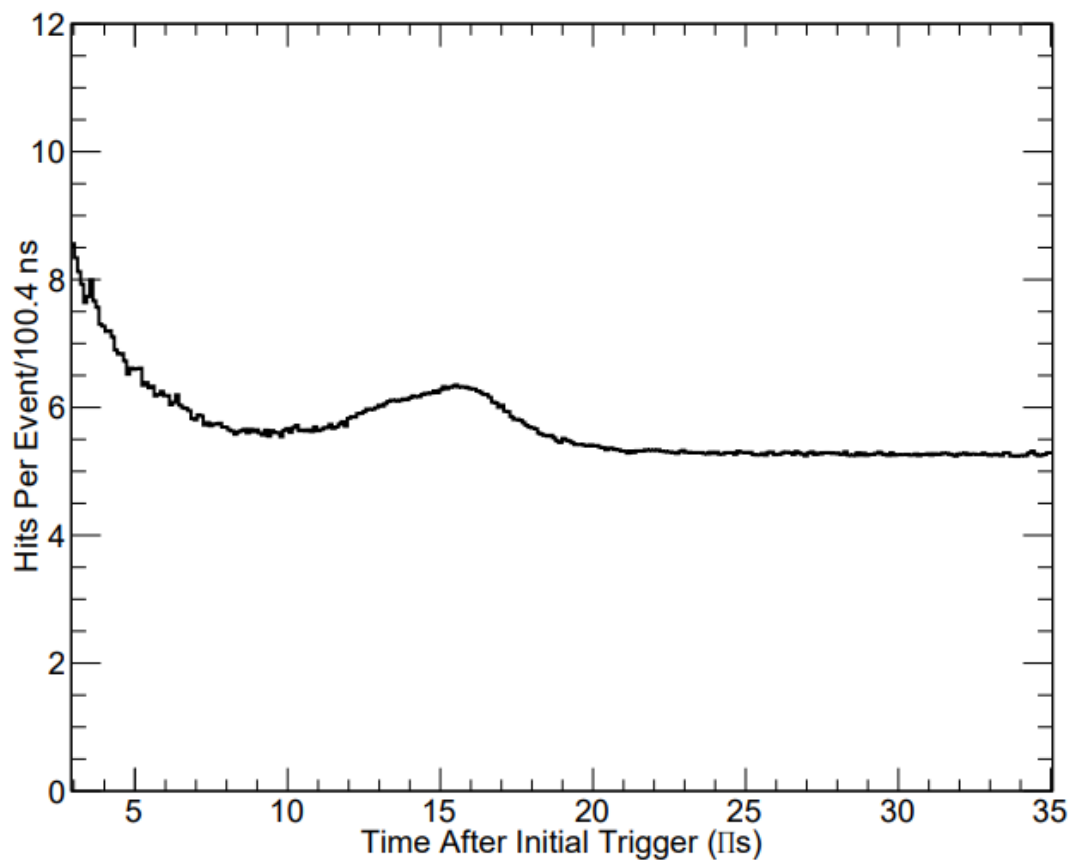
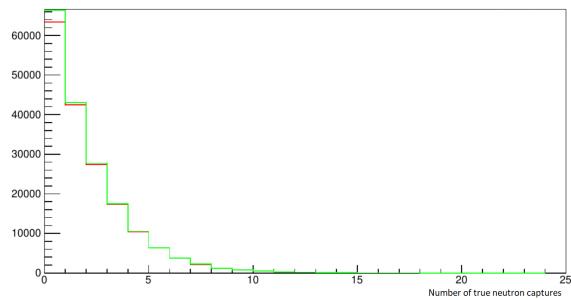
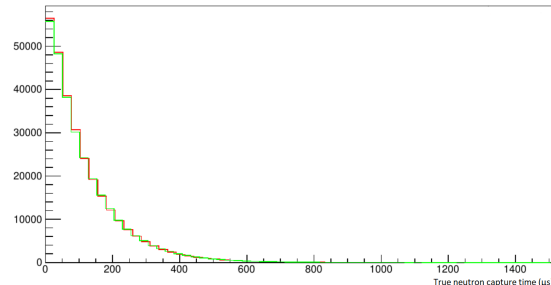


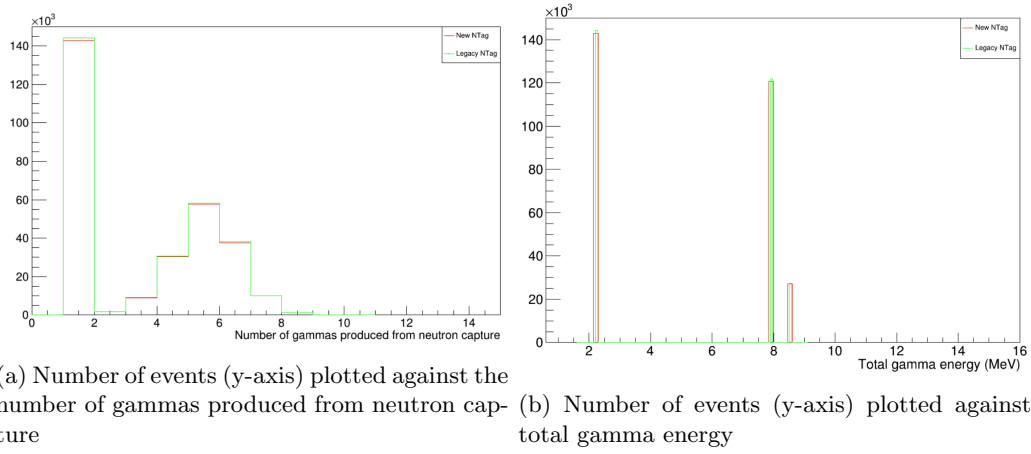
Figure 7.17: PMT hit rates per event from the average of events during SK-IV. The after-pulsing peak can clearly be seen in the 12 to 18 μ s region, after which the hit rate is flat for the remainder of the hit window.



(a) Number of events (y-axis) plotted against number of true neutron captures



(b) Number of events (y-axis) plotted against time of all neutron captures in microseconds

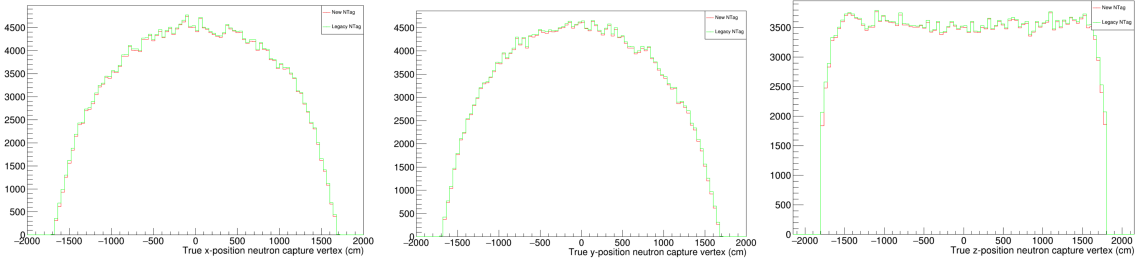


capture was classified as a capture on Hydrogen. If there are a number of gammas produced in quick succession, the group of gammas is classified as a cascade, and if the energy of the gamma cascade is 8.5 MeV in total it is classified as a neutron capture on ^{155}Gd and if the energy of the gamma cascade is 7.9 MeV, it is classified as a neutron capture on ^{157}Gd . Distributions of the number of gammas produced from neutron capture in the simulation, and also the energy of these gammas were plotted, shown for both the legacy (green) and new (red) NTag code, shown in Figures 7.19a and 7.19b respectively.

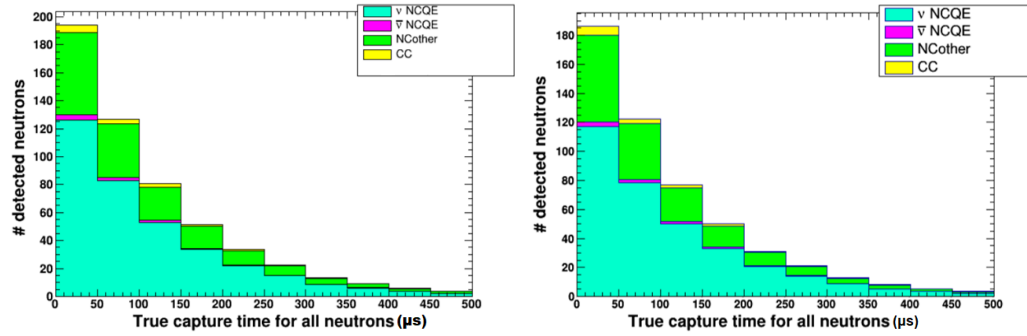
Figure 7.19a shows that both NTag algorithms have the same number of gammas produced by neutron capture on hydrogen (shown by the peak at 2.22 MeV), and the same number of gammas for the gamma cascade produced by neutron capture on the ^{155}Gd and ^{157}Gd isotopes of Gadolinium, where the modal number of gammas in the cascade for both NTag code is five. In addition to checking the number and energy of the gammas, and the number and time of true neutron captures, the neutron capture positions for the x,y and z directions were also plotted for Figures 7.20a, 7.20b and 7.20c.

Truth information reduction cut plots

After ensuring that the truth neutron tagging information was the same between the legacy and new NTag versions, the next step was to produce plots with the NCQE reduction cut criteria in order to see the distribution of neutrons for certain variables which satisfy the NCQE criteria. By rewriting aspects of the new NTag code to incorporate the BONSAI variables needed for the NCQE selection, the same reduction cut criteria could be applied to the new NTag code as it was to the new NTag code. Figures 7.21a and 7.21b show



(a) True neutron capture x-position (b) True neutron capture y-position (c) True neutron capture z-position
(cm) (cm) (cm)



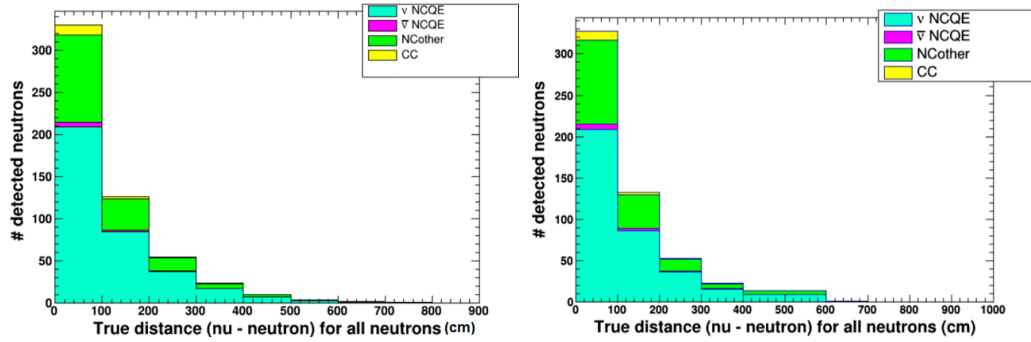
(a) Number of true neutrons detected plotted against true neutron capture time for the legacy NTag
(b) Number of true neutrons detected plotted against true neutron capture time for the new NTag

the number of true neutrons plotted against true neutron capture time for the legacy and new NTag respectively, while Figures 7.22a and 7.22b show the number of true neutrons plotted against the distance between the true neutron and neutrino capture vertices for the legacy and new NTag respectively.

With the level of gadolinium sulphate octahydrate in the simulation, the number of neutron captures on hydrogen and gadolinium should be about half and half. This is confirmed in the plots where the neutron captures in Figures 7.22b and 7.21b are separated into captures on hydrogen and gadolinium, shown in Figures 7.23a, 7.23b, 7.24a, 7.24b.

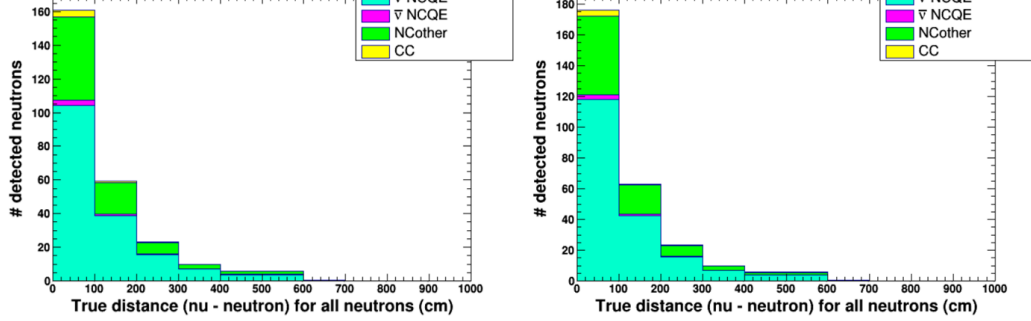
7.3.2 Primary selection criteria

The primary selection criteria are where the differences between the legacy and NTag algorithm come in. What remains constant for both neutron tagging algorithms is firstly, starting the neutron tagging search at 18 μs and secondly, the use of calculation of the time of flight corrected PMT hit times as the input into the neutron tagging search window.



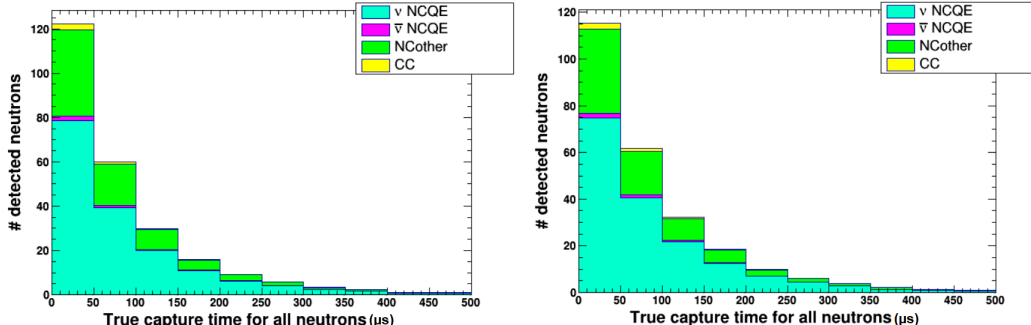
(a) Number of true neutrons detected plotted against the distance between the neutrino and neutron capture vertices for the legacy NTag

(b) Number of true neutrons detected plotted against the distance between the neutrino and neutron capture vertices for the new NTag



(a) Number of true neutrons detected plotted against the distance between the neutrino and neutron capture vertices for the new NTag, for captures on hydrogen

(b) Number of true neutrons detected plotted against the distance between the neutrino and neutron capture vertices for the new NTag, for captures on gadolinium



(a) Number of true neutrons detected plotted against true neutron capture time for the new NTag, for captures on hydrogen

(b) Number of true neutrons detected plotted against true neutron capture time for the new NTag, for captures on gadolinium

Criterion	Legacy	New
First	$7 \leq N10px \leq 50$	$7 \leq NHits \leq 400$
Second	$N200px \leq 100$	$N200px \leq 1000$
Third	$\Delta t_0 \geq 20\text{nsec}$	$\Delta t_0 \geq 200\text{nsec}$

Table 7.5: NTag selection criteria for legacy and new NTag

The reason for calculating the residual time of flight for the gamma hits is because the electrons produced from the Compton scattering of gamma rays produced by the neutron capture on hydrogen and gadolinium appear as a point-like source of Cherenkov radiation. Due to the differing optical path lengths that these photons have, there is a difference in photon hit time. The difference in Cherenkov photon travel length before they hit different PMTs after the gamma rays from neutron capture Compton scatter off an electron needs to be taken into account via a time-of-flight (TOF) correction. Equation 7.13 gives the equation for the residual hit times t_i^{res} , where t_i is the hit time of the PMTs in the neutron search window and TOF_i is given by Equation 7.14, where PMT_i is the position vector of the hit PMT and VTX_ν is the position vector of the reconstructed neutrino vertex and c_{wt} is the speed of light in the medium. The reason VTX_ν is used instead of the Compton scattering vertex is because this vertex is unknown.

$$t_i^{\text{res}} = t_i - TOF_i \quad i \in \{ \text{Hit PMTs} \} \quad (7.13)$$

$$TOF_i = \frac{\left\| \overrightarrow{PMT_i} - \overrightarrow{VTX_\nu} \right\|}{c_{wt}} \quad (7.14)$$

Before the neutron candidate is passed to the secondary selection, other cuts are used to reject candidates which are not neutrons from NCQE interactions. Table 7.5 shows the difference between the legacy and new primary selection criteria. The legacy NTag algorithm primary criteria used a 10 nsec sliding window in which hits are searched for a neutron candidate, where the first selection criteria involved making sure the number of hits in the 10 nsec ($N10px$) timing window should not exceed 50, and second criteria is that the surrounding window of 200 nsec should not contain more than 100 hits. The third criterion was that in order to avoid double-counting the same 2.2 MeV gamma from neutron capture on hydrogen, each consecutive neutron candidate must be more than 20 nanoseconds apart.

7.3.3 Secondary selection criteria

When the neutron vertex is found by this method, 14 variables which describe different aspects of the neutron candidate are calculated. For each of the neutron candidates the vector of these variables are computed and fed into the neural network and this produces an output value which is between 0 and 1. These variables relate to different features regarding categorising hits from neutron capture on Gd or H, including the number of the hits from neutron capture, the isotropy of these hits, the Cherenkov angles of these hits and the position of the neutron vertex in the detector when capture occurs. A description of these variables are given as follows:

N10nvx

This is the number of hits in the 10ns sliding window of the neutron candidate

N300S

Excluding the number of hits in the 10ns sliding window (N10nvx), this is the number of hits in the extended window of 300ns.

NcS

This variable is defined as:

$$NcS = N10nvx - Nclushit \quad (7.15)$$

Where $Nclushit$ is the number of clusterised hits: if hit i and j are hits on PMTs, then for hit i and hit j the hit vector \hat{r}_i can be written as:

$$\hat{r}_i = \frac{\overrightarrow{PMT_i} - \overrightarrow{VTX_n}}{\left\| \overrightarrow{PMT_i} - \overrightarrow{VTX_n} \right\|} \quad (7.16)$$

where the angle at the point of the neutron capture vertex between \hat{r}_i and \hat{r}_j of the PMT hits is defined as:

$$\theta_{ij} = \arccos(\hat{p}_i \cdot \hat{p}_j) \quad (7.17)$$

where the hits are defined as clustered if θ_{ij} is less than 14

llrca

This variable is the log likelihood ratio calculated using triplets of hits from N10nvx that

make up a rudimentary Cherenkov cone, from which the opening angle θ is calculated. Two PDFs (θ_{Ci}) and (θ_{Cj}) are calculated from each θ_{Ci} where p_s and p_b are the probability density functions of θ_C depending on whether the hits come from a true neutron capture on Gd or H or a false neutron capture which makes up the background. The log likelihood ratio variable is computed using Equation 7.18.

$$llrca = \sum_{i \in \{triplets\}} \log \left(\frac{f_B(\theta_{Ci})}{f_S(\theta_{Ci})} \right) \quad (7.18)$$

beta-n

These variables (where n = 1,2,3,4,5) are defined using Legendre polynomials, shown in Equation 7.19, which gives the isotropy of the Cherenkov hits.

$$\text{beta} - n = \frac{2}{N10nvx(N10nvx - 1)} \sum_{i \neq j} \text{Legendre}_n(\cos \theta_{ij}) \quad (7.19)$$

where Legendre_n gives the Legendre polynomial of order n and θ_{ij} is the angle between hit PMTs relative to the neutron capture vertex.

ndwall

This parameter, similar to dwall, gives the shortest distance of the neutron capture vertex from the wall of the Super-Kamiokande tank.

ntowall

This variable (similar to effwall), gives the distance of the neutron capture vertex from the wall, however, unlike ndwall it gives the direction of the neutron capture specifically along the direction of the centre of the hits. The direction (\vec{R}) is given by:

$$\vec{\text{dir}} = \sum_{i=1}^{N10nvx} \hat{p}_i \quad (7.20)$$

Chapter 8

Systematic and statistical uncertainty calculations

8.1 Systematic uncertainty calculation methodology

The systematic uncertainties for this analysis are calculated using the probability distribution functions of each quantity appearing in the formula for the mean neutron multiplicity, which is given by:

$$M = \frac{\#n_{\text{det}} - R \times \#\nu_{\text{det}}}{T} \frac{1}{\#\nu_{\text{det}}} \quad (8.1)$$

By random sampling the probability distribution functions for each of the terms in Equation (8.1) one can calculate the multiplicity probability distribution functions for both the statistical uncertainty and the systematic uncertainty. The statistical uncertainty for the value for the multiplicity is related to the variation in the number of detected neutrons, while the systematic uncertainty is related to the variation on the tagging efficiency and the background rate. The total search time for the tagged neutrons is dependent on the number of "windows" in which the neutron is searched for in, and therefore the term for the number of detected neutrinos. Because any variation on the number of neutrinos which are detected is unrelated to the value for the mean neutron multiplicity, calculating a probability mass function for the number of neutrinos is unnecessary.

A Poissonian distribution is used to model the distribution for the number of detected neutrons, due to its value being approximated by counting the positives in the timing

window that the neutron tagging search is carried out in. The mean value of this Poisson distribution is the number of detected neutrons $\langle \#n_{\text{detected}} \rangle$.

$$PMF(\#n_{\text{detected}}) = \frac{1}{(\#n_{\text{detected}})!} \langle \#n_{\text{detected}} \rangle^{\#n_{\text{detected}}} e^{-\langle \#n_{\text{detected}} \rangle} \quad (8.2)$$

Regarding the background rate, this is estimated from dummy spill data. The background rate error is associated with the statistical variation of the Monte Carlo size that the background rate is associated with, and secondly the change of the background rate value during the SK-V period. The statistical variation of the MC is modelled using a Poisson, but the statistics are high enough so that it appears Gaussian, while the uncertainty relating to time variation is characterised by its own probability distribution function. In contrast, the tagging efficiency is model dependent and has systematic uncertainties relating to this. The two ways in which the systematic error are estimated are either using MC re-weighting or MC regeneration.

For the MC-reweighting approach, weights are applied to a quantity and the tagging efficiency of the re-weighted MC is extracted. The general methodology is to have the input of a model (given by a set of parameters) and to vary them one by one and then calculate the reweighted tagging efficiencies - the set of relative discrepancies δ_i are computed from this set of reweighted tagging efficiencies T_i and the nominal tagging efficiency T_{nom} using Equation (8.3).

$$\delta_i = \frac{T_i - T_{\text{nom}}}{T_{\text{nom}}} \quad i \in \{ \text{parameters} \} \quad (8.3)$$

These relative discrepancies δ_i are used to calculate the one individual discrepancy $\delta_{\text{reweighted}}$ that would describe the final deviation from the nominal tagging efficiency T_{nom} due to the systematic error. The parameter $\delta_{\text{reweighted}}$ describes the model which has been produced through 1σ variations of these parameters, therefore the final probability distribution function which describes the deviation from the nominal MC has a Gaussian distribution with the standard deviation being equal to $\delta_{\text{reweighted}}$.

The other method to estimate the systematic error on the tagging efficiency is the method of Monte Carlo regeneration. This is carried out by varying a parameter then regenerating the whole Monte Carlo and then extracting the tagging efficiency - therefore unlike with

MC re-weighting there is no set of discrepancies δ_i but instead two single discrepancies δ_{min} and δ_{max} . The resulting probability distribution which describes the deviation from the nominal Monte Carlo is a Gaussian which has the mean and standard deviation relating to the discrepancies shown in Equation (8.4).

$$\begin{cases} \mu = \frac{\delta_{\max} + \delta_{\min}}{2} \\ \sigma = \frac{\delta_{\max} - \delta_{\min}}{2} \end{cases} \quad (8.4)$$

8.2 Neutrino beam flux uncertainty

The uncertainty on neutrino beam fluxes can be evaluated by looking at the dependence of the tagging efficiency on the flux variations. The beam fluxes for the four flavour modes ($\nu_e \bar{\nu}_e \nu_\mu \bar{\nu}_\mu$) have the fractional uncertainties given for each mode, FHC and RHC. The binned uncertainties are shown in Figure 8.1.

Each individual bin for the flux is increased/decreased by its error, the Monte Carlo re-weighting method is then used to extract the tagging efficiency for each flux bin, and Equation (8.5) is used to calculate the fractional uncertainty.

$$\delta_i(\pm\sigma) = \frac{T_i(\pm\sigma) - T_{\text{nom}}}{T_{\text{nom}}} \quad i \in \{ \text{each flux bin} \} \quad (8.5)$$

Figure 8.2 shows the fractional errors calculated from the reweighted Monte Carlo, with the red bars showing the -1σ variation and the blue bars showing the $+1\sigma$ variation. Table ?? contains the value for the total uncertainty resulting from the neutrino beam flux, which was calculated using Equation (8.6), where the maximum value between the increased and decreased discrepancy is taken and summed over to produce the final neutrino flux beam uncertainty.

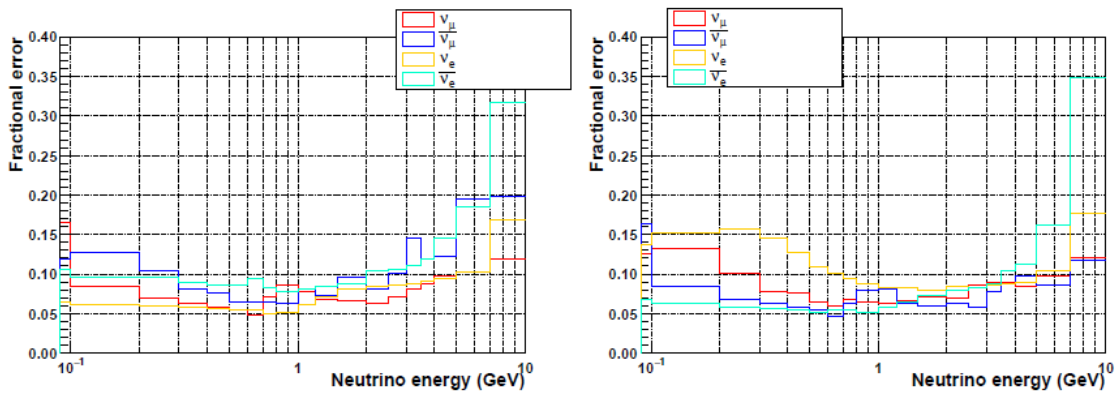


Figure 8.1: Fractional uncertainties of beam fluxes.

$$\delta_{\nu \text{ flux}} = \sum_{i \in \{\text{bins}\}} \max [|\delta_i(+\sigma)|, |\delta_i(-\sigma)|] \quad (8.6)$$

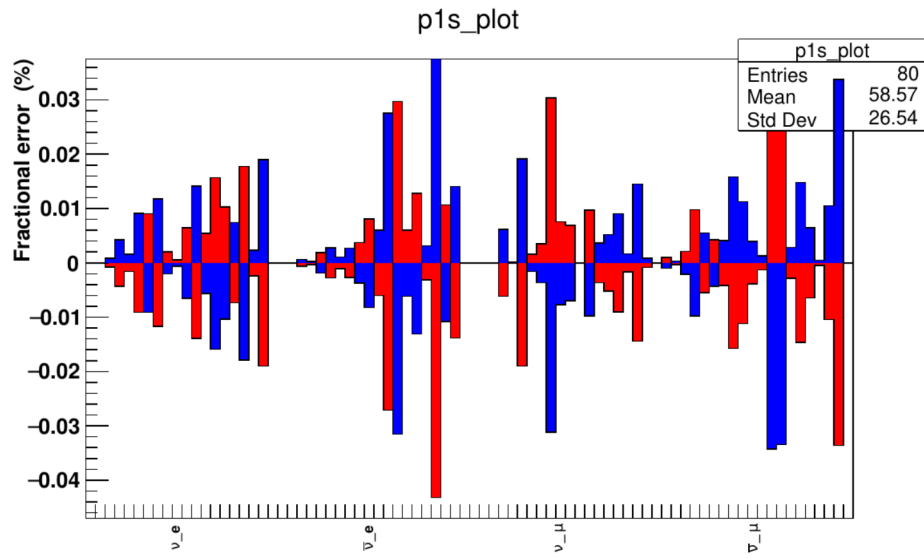


Figure 8.2: Tagging efficiency fractional uncertainties caused by neutrino beam flux discrepancies. From left to right the sections in this plot are comprised of the beam fluxes elements of $(\nu_e \bar{\nu}_e \nu_\mu \bar{\nu}_\mu)$ respectively.

8.3 Neutrino cross section uncertainty

A group of default neutrino cross section values are used to make up the nominal Monte Carlo from which the tagging efficiency is calculated. The values of the parameters that determine the cross sections are shown in Table 8.1. Each of the parameter values relate to a specific interaction type and are either a normalisation parameter or a parameter which shows a kinematic dependence.

For charged current quasi-elastic interactions, the uncertainty is described by the Fermi momentum of the oxygen nucleus, (p_F^O), the binding energy of the oxygen nucleus, (E_B^O) and the axial mass M_A^{CCQE} . The axial mass for CCQE interactions relates to the axial form factor which along with vector form factors is proportional to the cross section of the interactions. For neutrino interactions where two nucleons produce two holes (2p2h), an overall normalisation parameter takes the uncertainty of these interactions into account. For CC and $NC1\pi$ interactions, the uncertainty is described by the isospin background, the axial form factor C_{A5}^{RES} which just like for CCQE interactions relates to the axial mass M_A^{RES} . For neutral current and charged current interactions (both elastic and inelastic) there are normalisation parameters and energy dependent parameters to take the uncertainty into account. Finally, for charged current interactions with electron neutrinos, the braking radiation from the lepton in the final state is also considered when calculating the uncertainty and is treated using a normalisation parameter.

The Monte Carlo re-weighting method is used to reweight the nominal Monte Carlo on an event by event basis with each parameter value being increased and decreased by its uncertainty, and for each reweighted Monte Carlo the equivalent tagging efficiency value is extracted. Equation (8.7) shows how the fractional discrepancies are extracted from the nominal and reweighted tagging efficiency values.

$$\delta_i(\pm\sigma) = \frac{T_i(\pm\sigma) - T_{\text{nom}}}{T_{\text{nom}}} \quad i \in \{ \text{parameters} \} \quad (8.7)$$

Figure 8.3 shows the reweighted Monte Carlo fractional uncertainty plotted for the FHC sample. Since this sample contains a lot of NCother interactions, the uncertainty for this interaction type is greater than for the others.

Parameter	Interaction	Type	Value
p_F^O	CCQE	^{16}O Fermi momentum	$225 \pm 31\text{MeV}/c$
E_B^O	CCQE	^{16}O binding energy	$27 \pm 9\text{MeV}$
M_A^{CCQE}	CCQE	Axial mass	$1.2 \pm 0.41\text{GeV}/c^2$
$2p2h$	2p2 h	Normalization par.	1.0 ± 1.0
C_{A5}^{RES}	CC and NC1 π	Axial form factor	1.01 ± 0.12
M_A^{RES}	CC and NC1 π	Axial mass	$0.95 \pm 0.15\text{GeV}/c^2$
BG_A^{RES}	CC and NC1 π	I = 1/2 continuum background	1.3 ± 0.2
CC other	CC other	E-dependent par.	0.0 ± 0.4
CC elastic	CC elastic	Normalization par.	1.0 ± 0.3
NC other	NC other	E-dependent par.	1.0 ± 0.3
NC elastic	NC elastic	Normalization par.	1.0 ± 0.3
FSe ⁻ -Bremsstrahlung	CC ν_e	Normalization par.	1.00 ± 0.03

Table 8.1: Neutrino cross section parameters

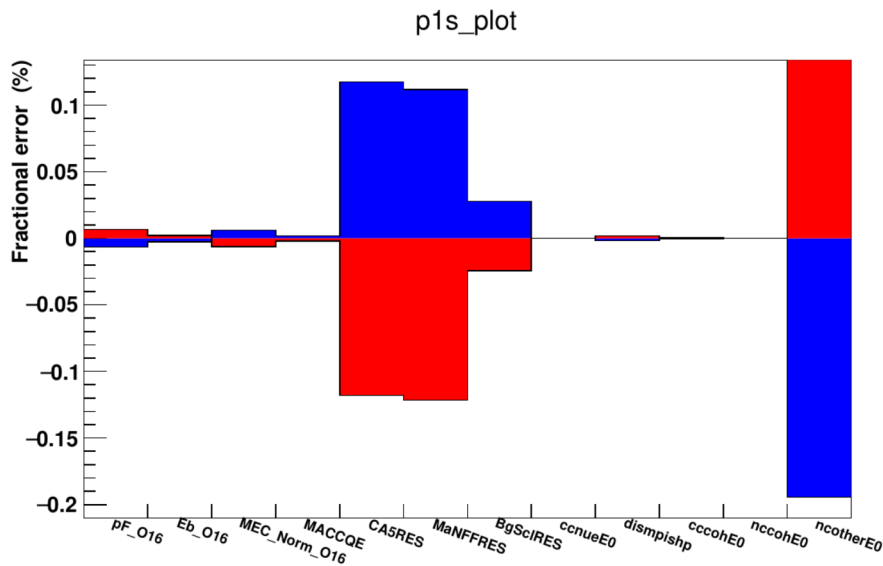


Figure 8.3: Tagging efficiency uncertainty caused by the cross-section parameters variations for the FHC mode

8.4 Pion final state interaction (FSI) and secondary interaction (SI) uncertainties

Even though this is an analysis concerned with neutral current quasi elastic interactions, pion events are a significant contribution to the background, and as a result it is important to examine the pion interaction uncertainties both for final state interactions and secondary interactions as their trajectories span the detector.

The neutrino-nucleus interaction simulator used in this analysis (NEUT) handles pion final state interactions and secondary interactions using a cascade model. This cascade model contains parameters which will have uncertainties on them and these will be transferred to a possible change in the tagging efficiency.

Depending on the momentum of the pions, different interaction types occur in the model. For pions with a momentum less than 500 MeV, the interactions in place are absorption (ABS), quasi-elastic scattering (QE) and charge exchange (CX).

Absorption occurs when the incident pion is absorbed by the nucleus and no pions remain in the final state. Quasi-elastic (QE) scattering occurs when there is only one pion observed in the final state and it has the same charge as the incident beam. Charge exchange occurs when the charged pion interacts wtht he nucleus and a single π_0 can be seen in the final state.

For pions with a momentum of greater than 500 MeV, a different set of interactions are used. Inelastic interactions (INEL) can now produce hadrons and replace absorption processes, but quasi-elastic scattering (QE) and charge exchange (CX) will still occur. The final state interaction parameters and the pion momentum range they are used in can be seen in Table 8.2. Each parameter scales the relevant very small probability of the charged pion interaction at every stage of the intra-nuclear cascade, aside from the parameter for charge exchange which scales only the fraction of low momentum QE scattering.

Parameter	Description	Momentum Region (MeV/c)
f_{ABS}	Absorption	< 500
f_{QE}	Quasi-elastic scatter	< 500
f_{CX}	Single charge exchange	< 500
$f_{\text{QE}H}$	Quasi-elastic scatter	> 500
$f_{\text{CX}H}$	Single charge exchange	> 500
f_{INEL}	Hadron (N + n π) production	> 500

Table 8.2: Table showing the pion final state interaction parameters in NEUT and the pion momentum range they are used in

A set of parameter variations which determine a surface in parameter space have been estimated by pion scattering experiments, the values for which are shown in Table 8.3. The 1σ surface has been explored using the nominal Monte Carlo re-weighting method and the analogous tagging efficiency uncertainty is shown in Equation 8.8, and the uncertainty stemming from the models shown in Table 8.3 is shown in Figure 8.4

$$\delta_i = \frac{T_i - T_{\text{nom}}}{T_{\text{nom}}} \quad i \in \text{parameter vector} \quad (8.8)$$

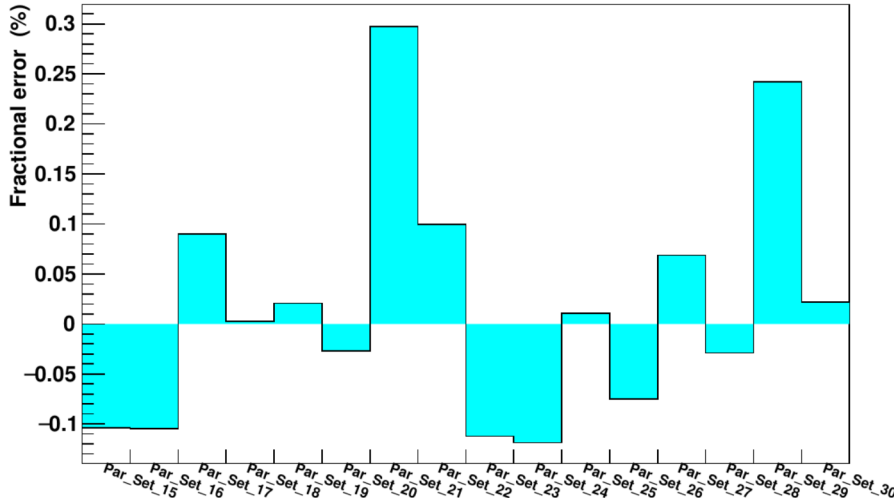


Figure 8.4: Tagging efficiency fractional uncertainty caused by the variation in the FSI/SI model parameters for the FHC mode.

Set	ABS	QE	CX	INEL	QEH	CXH
Nominal	1.1	1.0	1.0	1.0	1.8	1.8
Hadron production Up	0.7	0.6	0.5	1.5	1.1	2.3
	0.7	0.6	1.6	1.5	1.1	2.3
	1.6	0.7	0.4	1.5	1.1	2.3
	1.6	0.7	1.6	1.5	1.1	2.3
	0.6	1.4	0.6	1.5	1.1	2.3
	0.7	1.3	1.6	1.5	1.1	2.3
	1.5	1.5	0.4	1.5	1.1	2.3
	1.6	1.6	1.6	1.5	1.1	2.3
	0.7	0.6	0.5	0.5	2.3	1.3
	0.7	0.6	1.6	0.5	2.3	1.3
Hadron production Down	1.6	0.7	0.4	0.5	2.3	1.3
	1.6	0.7	1.6	0.5	2.3	1.3
	0.6	1.4	0.6	0.5	2.3	1.3
	0.7	1.3	1.6	0.5	2.3	1.3
	1.5	1.5	0.4	0.5	2.3	1.3
	1.6	1.6	1.6	0.5	2.3	1.3
	0.7	0.6	0.5	0.5	2.3	1.3
	0.7	0.6	1.6	0.5	2.3	1.3
	1.6	0.7	0.4	0.5	2.3	1.3
	1.6	0.7	1.6	0.5	2.3	1.3

Table 8.3: Pion FSI/SI model parameter nominal value and variations grouped according to inelastic hadron production value

8.5 Nucleon final state interactions

Uncertainties regarding the nucleon final state interactions can change the number of nucleons knocked out of ^{16}O , therefore how the tagging efficiency is changed due to the variation in nucleon final state interactions needs to be investigated. This uncertainty is extracted using GENIE, a Monte Carlo event generator which contains the INTRANUKE (hA) intranuclear transport model. The uncertainties in the total scattering probability for hadrons inside the target nuclei (x_{mfp}^N) and the uncertainties in the likelihood of each hadron rescattering method: (elastic (x_{el}^N), inelastic (x_{inel}^N), charge exchange (x_{cex}^N), pion production (x_π^N) and absorption (x_{abs}^N)) are taken into account. The fractional uncertainties for these modes for pions is shown in Table 8.4.

Abbreviation	Description of uncertainty	Fractional uncertainty
x_{mfp}^N	Nucleon mean free path (total rescattering probability)	$\pm 20\%$
x_{cex}^N	Nucleon charge exchange probability	$\pm 50\%$
x_{el}^N	Nucleon elastic reaction probability	$\pm 30\%$
x_{inel}^N	Nucleon inelastic reaction probability	$\pm 40\%$
x_{abs}^N	Nucleon absorption probability	$\pm 20\%$
x_π^N	Nucleon π -production probability	$\pm 20\%$

Table 8.4: Nucleon final state interaction parameters of the hA model executed inside GENIE.

A nominal GENIE Monte Carlo sample is generated (different from the previously used NEUT Monte Carlo) and this shifted using the re-weighting method to a varied GENIE Monte Carlo by individually increasing and decreasing the parameters in Table 8.4 by its error. For each shifted Monte Carlo produced, the fractional uncertainty can be written as in Equation 8.9.

$$\delta_i(\pm\sigma) = \frac{T_i(\pm\sigma) - T_{\text{nom}}}{T_{\text{nom}}} \quad i \in \{ \text{parameters} \} \quad (8.9)$$

The tagging efficiency fractional uncertainties are displayed in Figure 8.5, showing which parameter from Table 8.4 each uncertainty has arisen from.

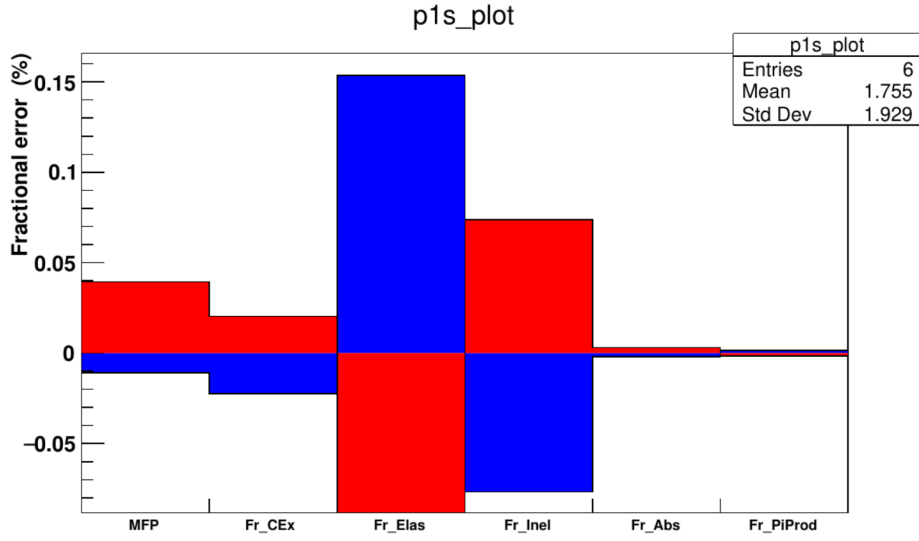


Figure 8.5: Tagging efficiency fractional uncertainties caused by the nucleon final state interaction model parameter variation for the FHC mode

8.6 Muon and pion capture on Oxygen-16

Neutrons are produced from negative muon capture on ^{16}O as shown in Equation 8.10.



Direct neutrons are produced from pion capture on ^{16}O , but also a number of evaporation neutrons that leave the nucleus. For the capture of muons and pions on ^{16}O , the energy spectra of the neutrons produced have been measured: for muons the spectra can range up to 15 MeV, while in the case of pions the spectra can reach up to 100 MeV.

Geant4 simulates the capture processes for muons and pions, but there are alternate models that can be used: for example, the Chiral Invariant Phase Space (CHIPS) model for muon captures (based on non perturbative QCD) and two different routines for pion capture, one which is based on CHIPS and one based on intra-nuclear cascade.

Because any change in the model can alter the energy spectra of the neutrons, these alternative functions can be used to estimate the fractional uncertainties for the tagging efficiency. This is done by using the MC regeneration method, where the nominal Monte Carlo is regenerated by replacing the default Geant4 routines with the alternative models.

For the alterantive muon capture model and the two alternative pion capture models, the fractional discrepancies are shown in Equation 8.11.

$$\begin{aligned}\delta_{muonCHIPS} &= \frac{T_{muonCHIPS} - T_{nom}}{T_{nom}} \\ \delta_{pionCHIPS} &= \frac{T_{pionCHIPS} - T_{nom}}{T_{nom}} \\ \delta_{pionBert} &= \frac{T_{pionBert} - T_{nom}}{T_{nom}}\end{aligned}\tag{8.11}$$

Figure 8.6 shows the fractional uncertainties caused by muon and pion capture on oxygen for each model.

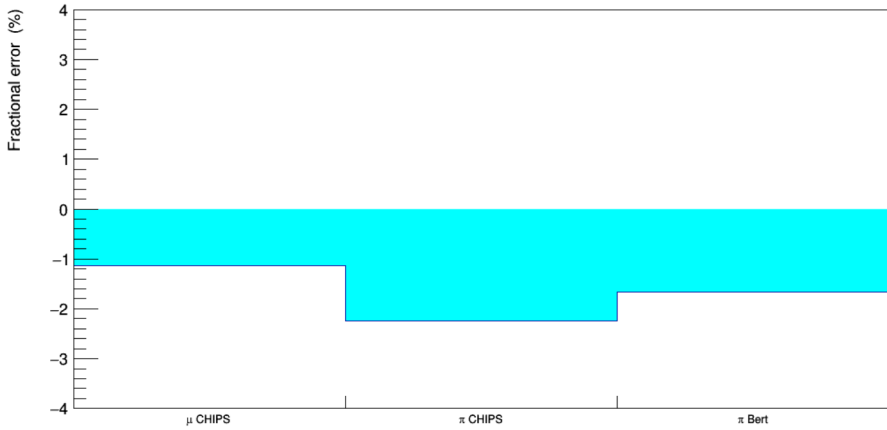


Figure 8.6: Fractional uncertainties in the tagging efficiency caused by muon and pion capture on the muon capture CHIPS model, pion capture CHIPS model and the pion capture Bertini model.

8.7 Nucleon SI

Uncertainties in how Nucleon SI interactions are modelled can affect the tagging efficiency, due to how these uncertainties can affect the final number of nucleons present in the simulation and how far they travel in the detector medium. There are two Monte Carlo code systems used in order to determine how nucleons travel in the simulation, MICAP and HETC. These come as part of GCALOR, used to determine the energy and direction of incident hadrons, leptons and photons. MICAP (Monte-carlo-Ionization-Chamber-Analysis-Program), which simulates interactions based on calculated cross section and angular distributions for secondary particles, and is called for neutrons with a kinetic energy below

20 MeV. HETC on the other hand, is the High-Energy-Transport-Code, and is responsible for transporting charged hadrons above 20 MeV (up to an energy of 10 GeV) through the detector medium.

8.7.1 MICAP uncertainty calculation

A library of cross-section data called ENDF (Evaluated Nuclear Data Files) are used by MICAP to determine what processes the neutrons go through in the detector medium, and their respective cross sections. There are two versions of libraries which are used in evaluating the uncertainty in the tagging efficiency, version B release V (released in 1978) and version B release VIII, released in 2018. There is very little difference between the total neutron on hydrogen cross sections between the two versions of the code, however, in the energy range of 0.1 MeV to 20 MeV, there are differences of up to 40% in the cross-sections of neutron on oxygen cross sections. Both an elastic and inelastic part comprise the total cross-section of a nucleus, and these can effect the way neutrons travel in the simulated detector medium and also the way secondary particles from these interactions are distributed. The way these inelastic processes are simulated depend on the nuclei involved: hydrogen nuclei capture the neutrons in the range (10^{-11} , 10^{-7}) MeV, while neutron captures on oxygen mainly happen in the 4 MeV to 20 MeV energy region. To calculate the way uncertainties arise from the way MICAP simulates neutron captures, the ENDF-V library is replaced by ENDF-VIII, and the tagging efficiency using this library (T_{VIII}) is evaluated from regenerated MC. Equation ?? shows the fractional uncertainty δ_{MICAP} regarding MICAP.

$$\delta_{mcp} = \frac{T_{VIII} - T_{nom}}{T_{nom}} \quad (8.12)$$

8.7.2 HETC uncertainty calculation

Due to there being no experimental data for cross-section calculations on nucleon-oxygen scattering in the energy range at which T2K functions, experimental data of proton-carbon scattering is used to assign error on the cross sections. In the proton-carbon scattering analysis, NEUT was used to evaluate the theoretical cross sections of carbon, and this uses cross sections calculated using the Bertini model, which is also used in HETC. The comparison of these calculated cross sections to other theoretical calculations as well as to data, showed that the total cross sections calculated by Bertini need to varied by $\pm 30\%$

in order to be consistent with them. As a result of this, the Monte Carlo is regenerated twice where the free nucleon-nucleon cross sections are scaled by $\pm 30\%$. Equation 8.13 shows the fractional uncertainty $\delta_{HETC}(\pm)$, related to the corresponding tagging efficiencies ($T_{HETC}(\pm)$).

$$\delta_{HETC}(\pm) = \frac{T_{HETC}(\pm) - T_{nom}}{T_{nom}} \quad (8.13)$$

Chapter 9

Conclusion

Bibliography

- [1] K. Abe, N. Abgrall, Y. Ajima, H. Aihara, J. Albert, C. Andreopoulos, B. Andrieu, M. Anerella, S. Aoki, O. Araoka, J. Argyriades, A. Ariga, T. Ariga, S. Assylbekov, D. Autiero, A. Badertscher, M. Barbi, G. Barker, G. Barr, M. Bass, M. Batkiewicz, F. Bay, S. Bentham, V. Berardi, B. Berger, I. Bertram, M. Besnier, J. Beucher, D. Beznosko, S. Bhadra, F. Blaszczyk, J. Blocki, A. Blondel, C. Bojochko, J. Bouchez, S. Boyd, A. Bravar, C. Bronner, D. Brook-Roberge, N. Buchanan, H. Budd, D. Calvet, S. Cartwright, A. Carver, R. Castillo, M. Catanesi, A. Cazes, A. Cervera, C. Chavez, S. Choi, G. Christodoulou, J. Coleman, G. Collazuol, W. Coleman, K. Connolly, A. Curioni, A. Dabrowska, I. Danko, R. Das, G. Davies, S. Davis, M. Day, G. D. Rosa, J. de André, P. de Perio, T. Dealtry, A. Delbart, C. Densham, F. D. Lodovico, S. D. Luise, P. D. Tran, J. Dobson, U. Dore, O. Drapier, F. Dufour, J. Dumarchez, S. Dytman, M. Dziewiecki, M. Dziomba, S. Emery, A. Ereditato, J. Escallier, L. Escudero, L. Esposito, M. Fechner, A. Ferrero, A. Finch, E. Frank, Y. Fujii, Y. Fukuda, V. Galymov, G. Ganetis, F. Gannaway, A. Gaudin, A. Gendotti, M. George, S. Giffin, C. Giganti, K. Gilje, A. Ghosh, T. Golan, M. Goldhaber, J. Gomez-Cadenas, S. Gomi, M. Gonin, N. Grant, A. Grant, P. Gumplinger, P. Guzowski, A. Haesler, M. Haigh, K. Hamano, C. Hansen, D. Hansen, T. Hara, P. Harrison, B. Hartfiel, M. Hartz, T. Haruyama, T. Hasegawa, N. Hastings, A. Hatzikoutelis, K. Hayashi, Y. Hayato, C. Hearty, R. Helmer, R. Henderson, N. Higashi, J. Hignight, A. Hillairet, E. Hirose, J. Holeczek, S. Horikawa, A. Hyndman, A. Ichikawa, K. Ieki, M. Ieva, M. Iida, M. Ikeda, J. Ilic, J. Imber, T. Ishida, C. Ishihara, T. Ishii, S. Ives, M. Iwasaki, K. Iyogi, A. Izmaylov, B. Jamieson, R. Johnson, K. Joo, G. Jover-Manas, C. Jung, H. Kaji, T. Kajita, H. Kakuno, J. Kameda, K. Kaneyuki, D. Karlen, K. Kasami, I. Kato, H. Kawamuko, E. Kearns, M. Khabibullin, F. Khanam, A. Khotjantsev, D. Kielczewska, T. Kikawa, J. Kim, J. Kim, S. Kim, N. Kimura, B. Kirby, J. Kisiel,

P. Kitching, T. Kobayashi, G. Kogan, S. Koike, A. Konaka, L. Kormos, A. Korzenev, K. Koseki, Y. Koshio, Y. Kouzuma, K. Kowalik, V. Kravtsov, I. Kreslo, W. Kropp, H. Kubo, J. Kubota, Y. Kudenko, N. Kulkarni, Y. Kurimoto, R. Kurjata, T. Kutter, J. Lagoda, K. Laihem, M. Laveder, K. Lee, P. Le, J. Levy, C. Licciardi, I. Lim, T. Lindner, R. Litchfield, M. Litos, A. Longhin, G. Lopez, P. Loverre, L. Ludovici, T. Lux, M. Macaire, K. Mahn, Y. Makida, M. Malek, S. Manly, A. Marchionni, A. Marino, A. Marone, J. Marteau, J. Martin, T. Maruyama, T. Maryon, J. Marzec, P. Masliah, E. Mathie, C. Matsumura, K. Matsuoka, V. Matveev, K. Mavrokordis, E. Mazzucato, N. McCauley, K. McFarland, C. McGrew, T. McLachlan, M. Messina, W. Metcalf, C. Metelko, M. Mezzetto, P. Mijakowski, C. Miller, A. Minamino, O. Mineev, S. Mine, A. Missert, G. Mituka, M. Miura, K. Mizouchi, L. Monfregola, F. Moreau, B. Morgan, S. Moriyama, A. Muir, A. Murakami, J. Muratore, M. Murdoch, S. Murphy, J. Mysslik, N. Nagai, T. Nakadaira, M. Nakahata, T. Nakai, K. Nakajima, T. Nakamoto, K. Nakamura, S. Nakayama, T. Nakaya, D. Naples, M. Navin, B. Nelson, T. Nicholls, C. Nielsen, K. Nishikawa, H. Nishino, K. Nitta, T. Nobuhara, J. Nowak, Y. Obayashi, T. Ogitsu, H. Ohhata, T. Okamura, K. Okumura, T. Okusawa, S. Oser, M. Otani, R. Owen, Y. Oyama, T. Ozaki, M. Pac, V. Palladino, V. Paolone, P. Paul, D. Payne, G. Pearce, J. Perkin, V. Pettinacci, F. Pierre, E. Poplawska, B. Popov, M. Posiadala, J.-M. Poutissou, R. Poutissou, P. Przewlocki, W. Qian, J. Raaf, E. Radicioni, P. Ratoff, T. Raufer, M. Ravonel, M. Raymond, F. Retiere, A. Robert, P. Rodrigues, E. Rondio, J. Roney, B. Rossi, S. Roth, A. Rubbia, D. Ruterbories, S. Sabouri, R. Sacco, K. Sakashita, F. Sánchez, A. Sarrat, K. Sasaki, K. Scholberg, J. Schwehr, M. Scott, D. Scully, Y. Seiya, T. Sekiguchi, H. Sekiya, M. Shibata, Y. Shimizu, M. Shiozawa, S. Short, M. Siyad, R. Smith, M. Smy, J. Sobczyk, H. Sobel, M. Sorel, A. Stahl, P. Stamoulis, J. Steinmann, B. Still, J. Stone, M. Stodulski, C. Strabel, R. Sulej, A. Suzuki, K. Suzuki, S. Suzuki, S. Suzuki, Y. Suzuki, Y. Suzuki, J. Swierblewski, T. Szeglowski, M. Szeptycka, R. Tacik, M. Tada, M. Taguchi, S. Takahashi, A. Takeda, Y. Takenaga, Y. Takeuchi, K. Tanaka, H. Tanaka, M. Tanaka, M. Tanaka, N. Tanimoto, K. Tashiro, I. Taylor, A. Terashima, D. Terhorst, R. Terri, L. Thompson, A. Thorley, W. Toki, S. Tobayama, T. Tomaru, Y. Totsuka, C. Touramanis, T. Tsukamoto, M. Tzanov, Y. Uchida, K. Ueno, A. Vacheret, M. Vagins, G. Vasseur, T. Wachala, J. Walding, A. Waldron, C. Walter, P. Wanderer, J. Wang, M. Ward, G. Ward, D. Wark, M. Wascko, A. Weber, R. Wendell, N. West, L. Whitehead, G. Wikström, R. Wilkes, M. Wilking, Z. Williamson, J. Wilson, R. Wilson, T. Wongji-

rad, S. Yamada, Y. Yamada, A. Yamamoto, K. Yamamoto, Y. Yamanoi, H. Yamaoka, T. Yamauchi, C. Yanagisawa, T. Yano, S. Yen, N. Yershov, M. Yokoyama, T. Yuan, A. Zalewska, J. Zalipska, L. Zambelli, K. Zaremba, M. Ziembicki, E. Zimmerman, M. Zito et al. Measurements of the t2k neutrino beam properties using the INGRID on-axis near detector. *Nuclear Instruments and Methods in Physics Research Section A: Accelerators, Spectrometers, Detectors and Associated Equipment*, 694:211–223, dec 2012.

- [2] K. Abe, R. Akutsu, A. Ali, C. Alt, C. Andreopoulos, L. Anthony, M. Antonova, S. Aoki, A. Ariga, Y. Ashida, E. Atkin, Y. Awataguchi, S. Ban, M. Barbi, G. Barker, G. Barr, C. Barry, M. Batkiewicz-Kwasniak, A. Beloshapkin, F. Bench, V. Berardi, S. Berkman, L. Berns, S. Bhadra, S. Bienstock, A. Blondel, S. Bolognesi, B. Bourguille, S. Boyd, D. Brailsford, A. Bravar, D. B. Berguño, C. Bronner, A. Bubak, M. B. Avanzini, J. Calcutt, T. Campbell, S. Cao, S. Cartwright, M. Catanesi, A. Cervera, A. Chappell, C. Checchia, D. Cherdack, N. Chikuma, G. Christodoulou, J. Coleman, G. Collazuol, L. Cook, D. Coplowe, A. Cudd, A. Dabrowska, G. D. Rosa, T. Dealtry, P. Denner, S. Dennis, C. Densham, F. D. Lodovico, N. Dokania, S. Dolan, O. Drapier, J. Dumarchez, P. Dunne, L. Eklund, S. Emery-Schrenk, A. Ereditato, P. Fernandez, T. Feusels, A. Finch, G. Fiorentini, G. Fiorillo, C. Francois, M. Friend, Y. Fujii, R. Fujita, D. Fukuda, R. Fukuda, Y. Fukuda, K. Gameil, C. Giganti, T. Golan, M. Gonin, A. Gorin, M. Guigue, D. Hadley, J. Haigh, P. Hamacher-Baumann, M. Hartz, T. Hasegawa, N. Hastings, T. Hayashino, Y. Hayato, A. Hiramoto, M. Hogan, J. Holeczek, N. H. Van, F. Iacob, A. Ichikawa, M. Ikeda, T. Ishida, T. Ishii, M. Ishitsuka, K. Iwamoto, A. Izmaylov, B. Jamieson, S. Jenkins, C. Jesús-Valls, M. Jiang, S. Johnson, P. Jonsson, C. Jung, M. Kabirnezhad, A. Kaboth, T. Kajita, H. Kakuno, J. Kameda, D. Karlen, S. Kasetti, Y. Kataoka, T. Katori, Y. Kato, E. Kearns, M. Khabibullin, A. Khotjantsev, T. Kikawa, H. Kim, J. Kim, S. King, J. Kisiel, A. Knight, A. Knox, T. Kobayashi, L. Koch, T. Koga, A. Konaka, L. Kormos, Y. Koshio, K. Kowalik, H. Kubo, Y. Kudenko, N. Kukita, S. Kurabayashi, R. Kurjata, T. Kutter, M. Kuze, L. Labarga, J. Lagoda, M. Lamoureux, M. Laveder, M. Lawe, M. Licciardi, T. Lindner, R. Litchfield, S. Liu, X. Li, A. Longhin, L. Ludovici, X. Lu, T. Lux, L. Machado, L. Magaletti, K. Mahn, M. Malek, S. Manly, L. Maret, A. Marino, J. Martin, T. Maruyama, T. Matsubara, K. Matsushita, V. Matveev, K. Mavrokordidis, E. Mazzucato, M. McCarthy, N. McCauley, K. McFarland, C. McGrew, A. Mefodiev,

C. Metelko, M. Mezzetto, A. Minamino, O. Mineev, S. Mine, M. Miura, L. M. Bueno, S. Moriyama, J. Morrison, T. Mueller, L. Munteanu, S. Murphy, Y. Nagai, T. Nakadaira, M. Nakahata, Y. Nakajima, A. Nakamura, K. Nakamura, K. Nakamura, S. Nakayama, T. Nakaya, K. Nakayoshi, C. Nantais, T. Ngoc, K. Niewczas, K. Nishikawa, Y. Nishimura, T. Nonnenmacher, F. Nova, P. Novella, J. Nowak, J. Nugent, H. O’Keeffe, L. O’Sullivan, T. Odagawa, K. Okumura, T. Okusawa, S. Oser, R. Owen, Y. Oyama, V. Palladino, J. Palomino, V. Paolone, W. Parker, P. Paudyal, M. Pavin, D. Payne, G. Penn, L. Pickering, C. Pidcott, E. P. Guerra, C. Pistillo, B. Popov, K. Porwit, M. Posiadala-Zezula, A. Pritchard, B. Quilain, T. Radermacher, E. Radicioni, B. Radics, P. Ratoff, E. Reinherz-Aronis, C. Riccio, E. Rondio, S. Roth, A. Rubbia, A. Ruggeri, A. Rychter, K. Sakashita, F. Sánchez, C. Schloesser, K. Scholberg, J. Schwehr, M. Scott, Y. Seiya, T. Sekiguchi, H. Sekiya, D. Sgalaberna, R. Shah, A. Shaikhiev, F. Shaker, A. Shaykina, M. Shiozawa, W. Shorrock, A. Shvartsman, A. Smirnov, M. Smy, J. Sobczyk, H. Sobel, F. Soler, Y. Sonoda, J. Steinmann, S. Suvorov, A. Suzuki, S. Suzuki, Y. Suzuki, A. Sztuc, M. Tada, M. Tajima, A. Takeda, Y. Takeuchi, H. Tanaka, H. Tanaka, S. Tanaka, L. Thompson, W. Toki, C. Touramanis, K. Tsui, T. Tsukamoto, M. Tzanov, Y. Uchida, W. Uno, M. Vagins, S. Valder, Z. Vallari, D. Vargas, G. Vasseur, C. Vilela, W. Vinning, T. Vladislavljevic, V. Volkov, T. Wachala, J. Walker, J. Walsh, Y. Wang, D. Wark, M. Wascko, A. Weber, R. Wendell, M. Wilking, C. Wilkinson, J. Wilson, R. Wilson, K. Wood, C. Wret, Y. Yamada, K. Yamamoto, C. Yanagisawa, G. Yang, T. Yano, K. Yasutome, S. Yen, N. Yershov, M. Yokoyama, T. Yoshida, M. Yu, A. Zalewska, J. Zalipska, K. Zaremba, G. Zarnecki, M. Ziembicki, E. Zimmerman, M. Zito, S. Zsoldos et al. Measurement of neutrino and antineutrino neutral-current quasielasticlike interactions on oxygen by detecting nuclear deexcitation gamma-rays. *Physical Review D*, 100(11), dec 2019.

- [3] K. e. a. Abe. The T2K Experiment. *Nuclear Instruments and Methods in Physics Research Section A: Accelerators, Spectrometers, Detectors and Associated Equipment*, 659(1):106–135, Dec. 2011. arXiv: 1106.1238.
- [4] K. e. a. Abe. The T2K Neutrino Flux Prediction. *Physical Review D*, 87(1):012001, Jan. 2013. arXiv: 1211.0469.
- [5] K. e. a. Abe. Calibration of the Super-Kamiokande Detector. *Nuclear Instruments and Methods in Physics Research Section A: Accelerators, Spectrometers, Detectors*

and Associated Equipment, 737:253–272, Feb. 2014. arXiv: 1307.0162.

- [6] K. e. a. Abe. First gadolinium loading to Super-Kamiokande. *Nuclear Instruments and Methods in Physics Research Section A: Accelerators, Spectrometers, Detectors and Associated Equipment*, page 166248, Dec. 2021.
- [7] M. Aker, K. Altenmüller, M. Arenz, M. Babutzka, J. Barrett, S. Bauer, M. Beck, A. Beglarian, J. Behrens, T. Bergmann, U. Besserer, K. Blaum, F. Block, S. Bobien, K. Bokeloh, J. Bonn, B. Bornschein, L. Bornschein, H. Bouquet, T. Brunst, T. Caldwell, L. L. Cascio, S. Chilingaryan, W. Choi, T. Corona, K. Debowski, M. Deffert, M. Descher, P. Doe, O. Dragoun, G. Drexlin, J. Dunmore, S. Dyba, F. Edzards, L. Eisenblätter, K. Eitel, E. Ellinger, R. Engel, S. Enomoto, M. Erhard, D. Eversheim, M. Fedkevych, A. Felden, S. Fischer, B. Flatt, J. Formaggio, F. Fränkle, G. Franklin, H. Frankrone, F. Friedel, D. Fuchs, A. Fulst, D. Furse, K. Gauda, H. Gemmeke, W. Gil, F. Glück, S. Görhardt, S. Groh, S. Grohmann, R. Grössle, R. Gumbsheimer, M. H. Minh, M. Hackenjos, V. Hannen, F. Harms, J. Hartmann, N. Haußmann, F. Heizmann, K. Helbing, S. Hickford, D. Hilk, B. Hillen, D. Hillesheimer, D. Hinz, T. Höhn, B. Holzapfel, S. Holzmann, T. Houdy, M. Howe, A. Huber, T. James, A. Jansen, A. Kaboth, C. Karl, O. Kazachenko, J. Kellerer, N. Kernert, L. Kippenbrock, M. Kleesiek, M. Klein, C. Köhler, L. Köllenberger, A. Kopmann, M. Korzeczek, A. Kosmider, A. Kovalík, B. Krasch, M. Kraus, H. Krause, L. Kuckert, B. Kuffner, N. Kunka, T. Lasserre, T. Le, O. Lebeda, M. Leber, B. Lehnert, J. Letnev, F. Leven, S. Lichter, V. Lobashev, A. Lokhov, M. Machatschek, E. Malcherek, K. Müller, M. Mark, A. Marsteller, E. Martin, C. Melzer, A. Menshikov, S. Mertens, L. Minter, S. Mirz, B. Montreal, P. M. Guzmán, K. Müller, U. Naumann, W. Ndeke, H. Neumann, S. Niemes, M. Noe, N. Oblath, H.-W. Ortjohann, A. Osipowicz, B. Ostrick, E. Otten, D. Parno, D. Phillips, P. Plischke, A. Pollithy, A. Poon, J. Pouryamout, M. Prall, F. Priester, M. Röllig, C. Röttele, P.-O. Ranitzsch, O. Rest, R. Rinderspacher, R. Robertson, C. Rodenbeck, P. Rohr, C. Roll, S. Rupp, M. Ryšavý, R. Sack, A. Saenz, P. Schäfer, L. Schimpf, K. Schlösser, M. Schlösser, L. Schlüter, H. Schön, K. Schönung, M. Schrank, B. Schulz, J. Schwarz, H. Seitz-Moskaliuk, W. Seller, V. Sibille, D. Siegmann, A. Skasyrskaya, M. Slezák, A. Špalek, F. Spanier, M. Steidl, N. Steinbrink, M. Sturm, M. Suesser, M. Sun, D. Tcherniakhovski, H. Telle, T. Thümmler, L. Thorne, N. Titov, I. Tkachev, N. Trost, K. Urban, D. Vénos, K. Valerius, B. VanDevender, R. Vianden, A. V. Hernández, B. Wall, S. Wüstling, M. Weber, C. Weinheimer,

- C. Weiss, S. Welte, J. Wendel, K. Wierman, J. Wilkerson, J. Wolf, W. Xu, Y.-R. Yen, M. Zacher, S. Zadorozhny, M. Zbořil et al. Improved upper limit on the neutrino mass from a direct kinematic method by KATRIN. *Physical Review Letters*, 123(22), nov 2019.
- [8] S. Ando and K. Sato. Relic neutrino background from cosmological supernovae. *New Journal of Physics*, 6:170–170, Nov. 2004. arXiv: astro-ph/0410061.
 - [9] J. N. Bahcall. Solar models: An historical overview. *Nuclear Physics B - Proceedings Supplements*, 118:77–86, apr 2003.
 - [10] O. Benhar, N. Farina, H. Nakamura, M. Sakuda et al. Electron- and neutrino-nucleus scattering in the impulse approximation regime. *Physical Review D*, 72(5):053005, Sept. 2005.
 - [11] H. A. Bethe. Supernova mechanisms. *Reviews of Modern Physics*, 62(4):801–866, Oct. 1990.
 - [12] G. E. P. Box and M. E. Muller. A Note on the Generation of Random Normal Deviates. *The Annals of Mathematical Statistics*, 29(2):610 – 611, 1958.
 - [13] L. M. Brown. The idea of the neutrino. *Physics Today*, 31(9):23–28, Sept. 1978. Publisher: American Institute of Physics.
 - [14] S. Chakraborty, P. Bhattacharjee et al. Observing supernova neutrino light curve in future dark matter detectors. *Physical Review D*, 89(1):013011, Jan. 2014.
 - [15] B. T. Cleveland, T. Daily, J. Raymond Davis, J. R. Distel, K. Lande, C. K. Lee, P. S. Wildenhain et al. Measurement of the solar electron neutrino flux with the homestake chlorine detector. *The Astrophysical Journal*, 496(1):505–526, mar 1998.
 - [16] J. Cowan, C. L., F. Reines, F. B. Harrison, H. W. Kruse et al. Detection of the Free Neutrino: A Confirmation. *Science*, 124(3212):103–104, July 1956.
 - [17] G. Danby, J.-M. Gaillard, K. Goulian, L. M. Lederman, N. Mistry, M. Schwartz et al. Observation of high-energy neutrino reactions and the existence of two kinds of neutrinos. *Phys. Rev. Lett.*, 9:36–44, Jul 1962.

- [18] G. Danby, J.-M. Gaillard, K. Goulianos, L. M. Lederman, N. Mistry, M. Schwartz et al. Observation of high-energy neutrino reactions and the existence of two kinds of neutrinos. *Phys. Rev. Lett.*, 9:36–44, Jul 1962.
- [19] P. Fernández. Status of GADZOOKS!: Neutron Tagging in Super-Kamiokande. *Nuclear and Particle Physics Proceedings*, 273-275:353–360, Apr. 2016.
- [20] S. Fukuda and Y. e. a. Fukuda. The Super-Kamiokande detector. *Nuclear Instruments and Methods in Physics Research Section A: Accelerators, Spectrometers, Detectors and Associated Equipment*, 501(2-3):418–462, Apr. 2003.
- [21] K. Hirata and T. e. a. Kajita. Observation of a neutrino burst from the supernova SN1987A. *Physical Review Letters*, 58(14):1490–1493, Apr. 1987.
- [22] K. S. Hirata and others. Observation in the Kamiokande-II Detector of the Neutrino Burst from Supernova SN 1987a. *Phys. Rev. D*, 38:448–458, 1988.
- [23] Z. Maki, M. Nakagawa et al. Remarks on the Unified Model of Elementary Particles. *Progress of Theoretical Physics*, 28(5):870–880, 11 1962.
- [24] G. Marsaglia and T. A. Bray. A convenient method for generating normal variables. *SIAM Review*, 6(3):260–264, 1964.
- [25] L. Marti and M. e. a. Ikeda. Evaluation of gadolinium’s action on water Cherenkov detector systems with EGADS. *Nuclear Instruments and Methods in Physics Research Section A: Accelerators, Spectrometers, Detectors and Associated Equipment*, 959:163549, Apr. 2020.
- [26] S. L. Meo, C. Massimi et al. Measurement of the neutron capture cross section for ^{155}Gd and ^{157}Gd for Nuclear Technology. page 8.
- [27] B. Moffat, R. Ford, F. Duncan, K. Graham, A. Hallin, C. Hearns, J. Maneira, P. Skensved et al. Optical calibration hardware for the sudbury neutrino observatory. *Nuclear Instruments and Methods in Physics Research Section A: Accelerators, Spectrometers, Detectors and Associated Equipment*, 554(1-3):255–265, dec 2005.
- [28] H. Nagakura and K. Hotokezaka. Non-thermal neutrinos created by shock acceleration in successful and failed core-collapse supernova. *Monthly Notices of the Royal Astronomical Society*, 502(1):89–107, Jan. 2021. arXiv: 2010.15136.

- [29] L. Nanni. Fermi theory of beta decay: A first attempt at electroweak unification. *Advanced Studies in Theoretical Physics*, 13:281, 07 2019.
- [30] H. Nishino, K. Awai, Y. Hayato, S. Nakayama, K. Okumura, M. Shiozawa, A. Takeda, K. Ishikawa, A. Minegishi et al. High-speed charge-to-time converter ASIC for the Super-Kamiokande detector. *Nuclear Instruments and Methods in Physics Research Section A: Accelerators, Spectrometers, Detectors and Associated Equipment*, 610(3):710–717, Nov. 2009. arXiv: 0911.0986.
- [31] B. Pontecorvo. Mesonium and anti-mesonium. *Sov. Phys. JETP*, 6:429, 1957.
- [32] R. M. Pope and E. S. Fry. Absorption spectrum (380–700 nm) of pure water. ii. integrating cavity measurements. *Appl. Opt.*, 36(33):8710–8723, Nov 1997.
- [33] Y. Suzuki. The Super-Kamiokande experiment. *The European Physical Journal C*, 79(4):298, Apr. 2019.
- [34] K. Ueno. Analysis of nuclear de-excitation gamma-rays induced by neutrino-nucleon neutral-current interactions at SK using the T2K RUN-I/II data. page 87.
- [35] T. Vladisljevic. Constraining the T2K Neutrino Flux Prediction with 2009 NA61/SHINE Replica-Target Data. June 2018. arXiv:1804.00272 [hep-ex, physics:physics].

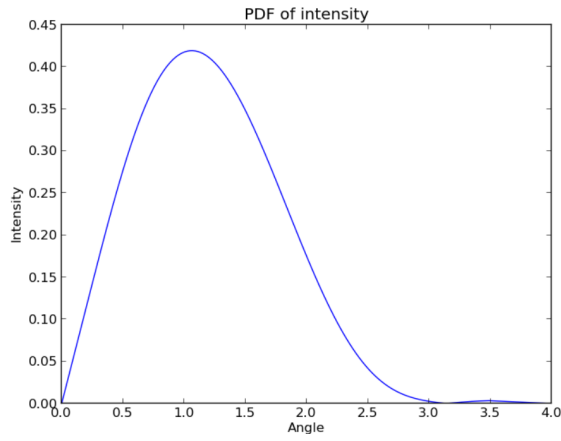
Appendix A

Appendix A

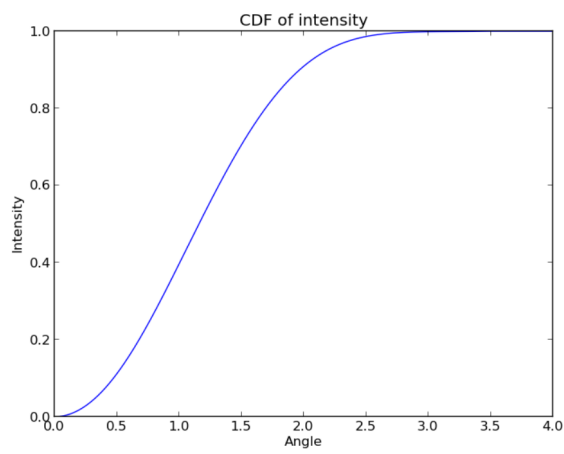
Figure A.1 shows the complete PDFs and CDFs for the B1 - B5 collimator data taken from the test stand at Warwick and Figure A.2 shows the complete PDFs and CDFs for the B1 - B5 diffusers. Figure A.3 show the inverse CDF fits for the collimator, and Figure A.4 shows the inverse CDF fits for the diffuser.

Figure A.1: PDFs and corresponding CDFs for the B1 - B5 collimators

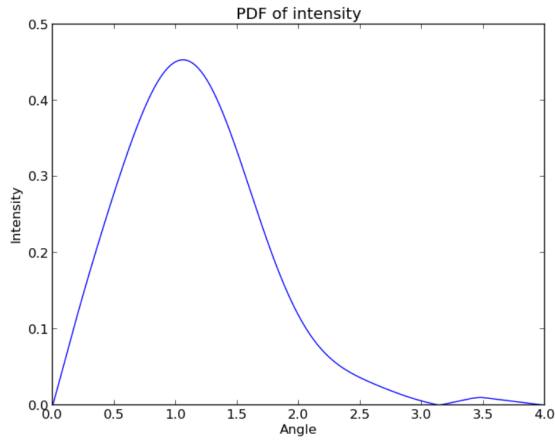
(a) B1 collimator PDF



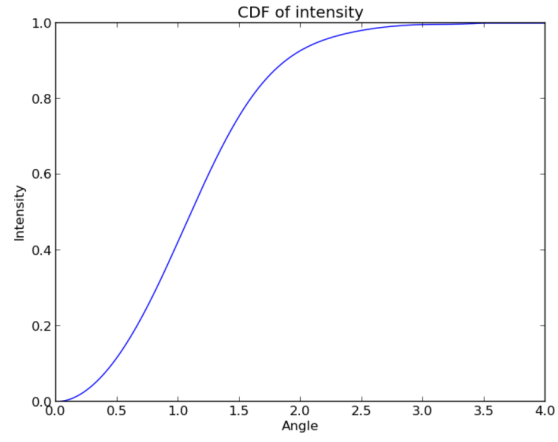
(b) B1 collimator CDF



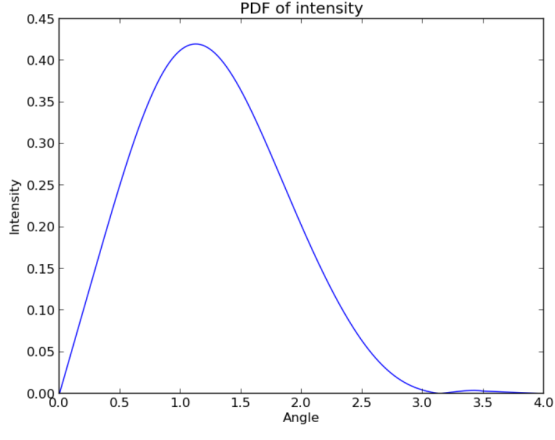
(c) B2 collimator PDF



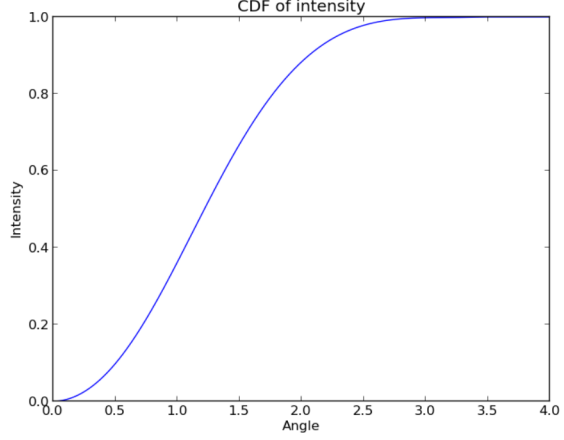
(d) B2 collimator CDF

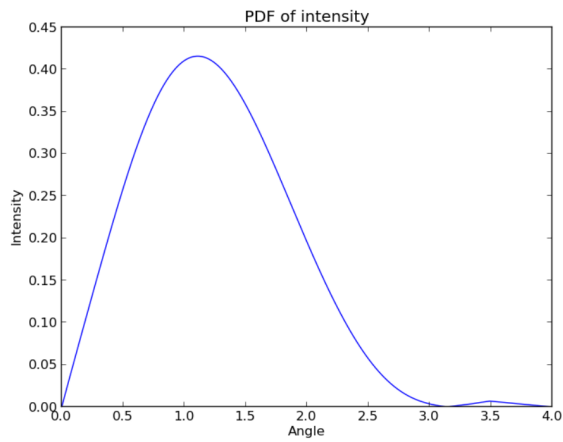


(e) B3 collimator PDF

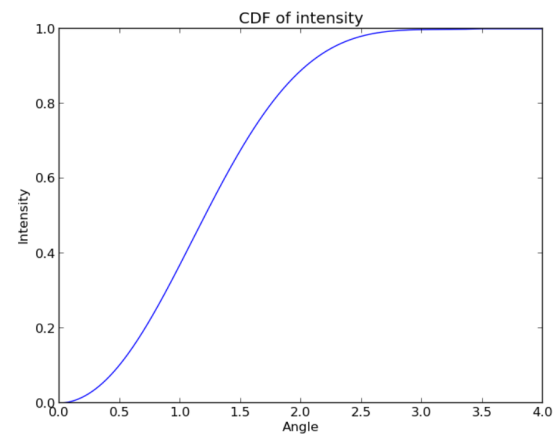


(f) B3 collimator CDF

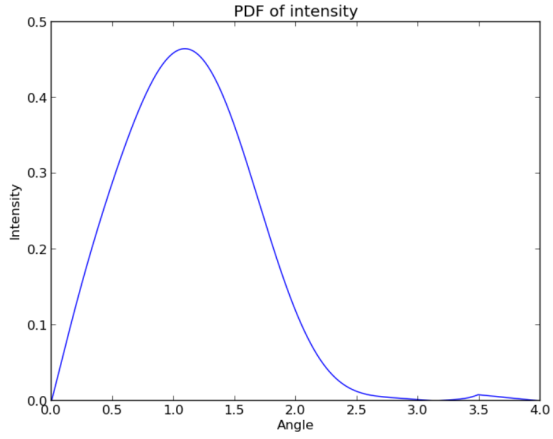




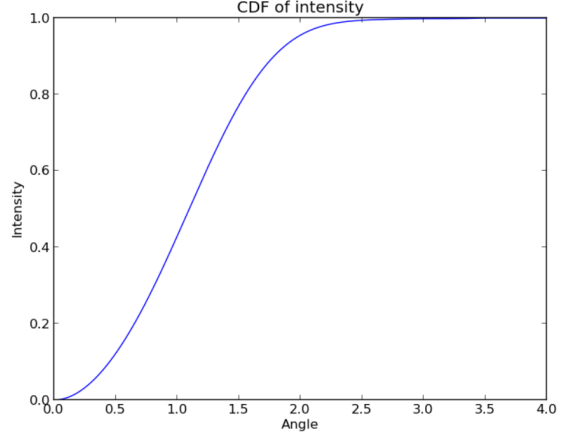
(g) B4 collimator PDF



(h) B4 collimator CDF



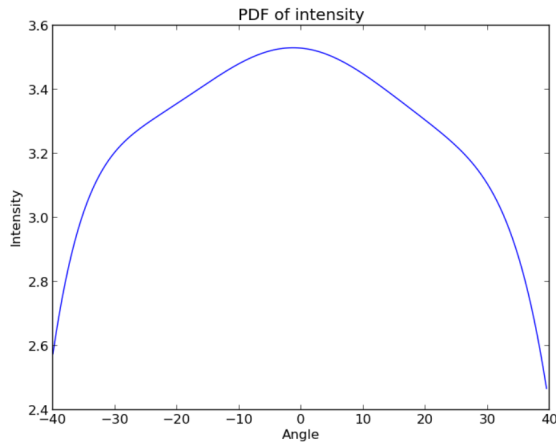
(i) B5 collimator PDF



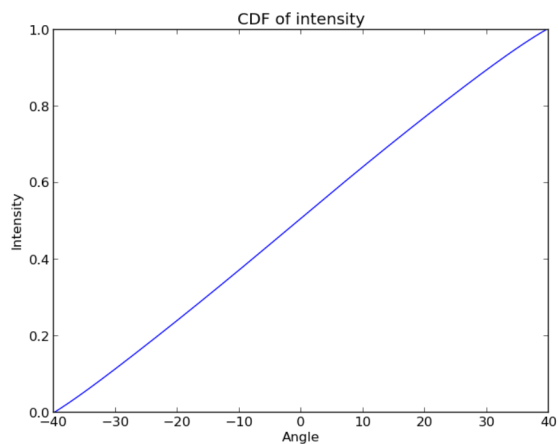
(j) B5 collimator CDF

Figure A.2: PDFs and corresponding CDFs for the B1 - B5 diffusers

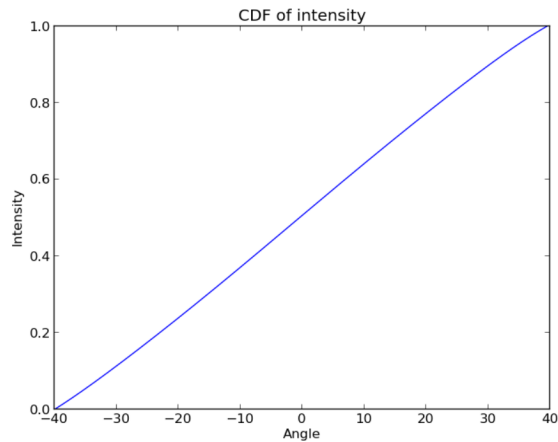
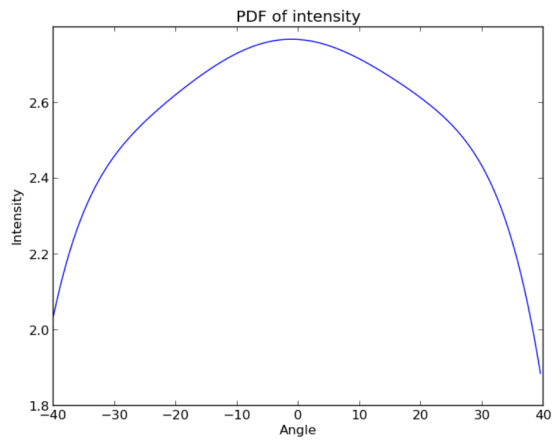
(a) B1 diffuser PDF



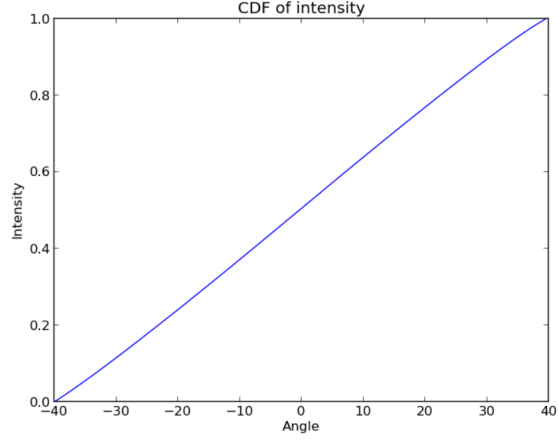
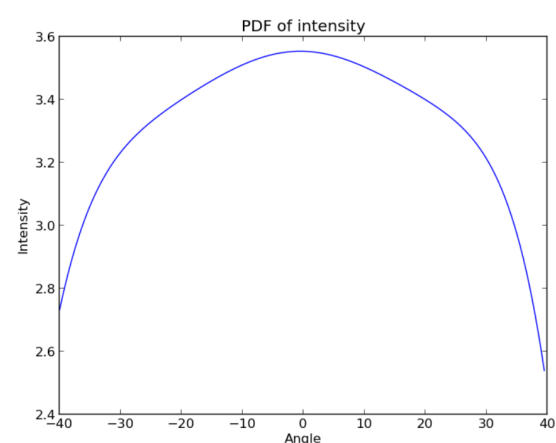
(b) B1 diffuser CDF

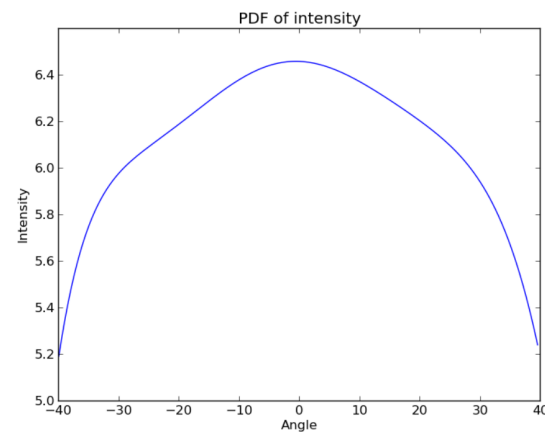


(c) B2 diffuser PDF

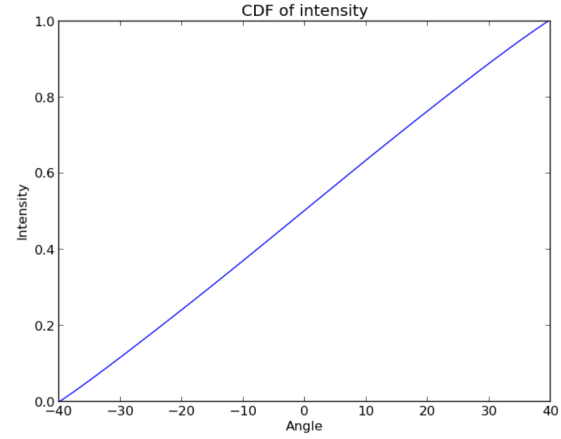


(e) B3 diffuser PDF

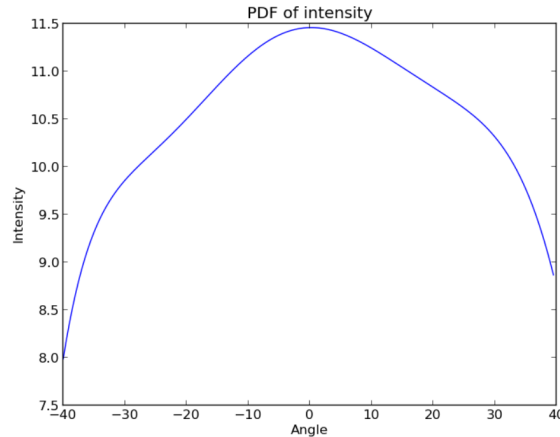




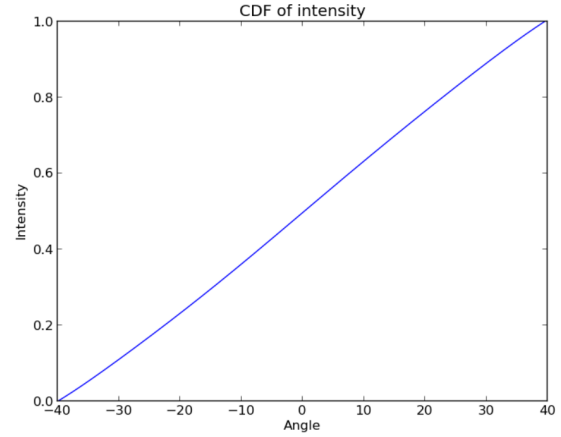
(g) B4 diffuser PDF



(h) B4 diffuser CDF



(i) B5 diffuser PDF



(j) B5 diffuser CDF

Figure A.3: CDF and inverse CDF fits for the B1 - B5 collimator PDFs

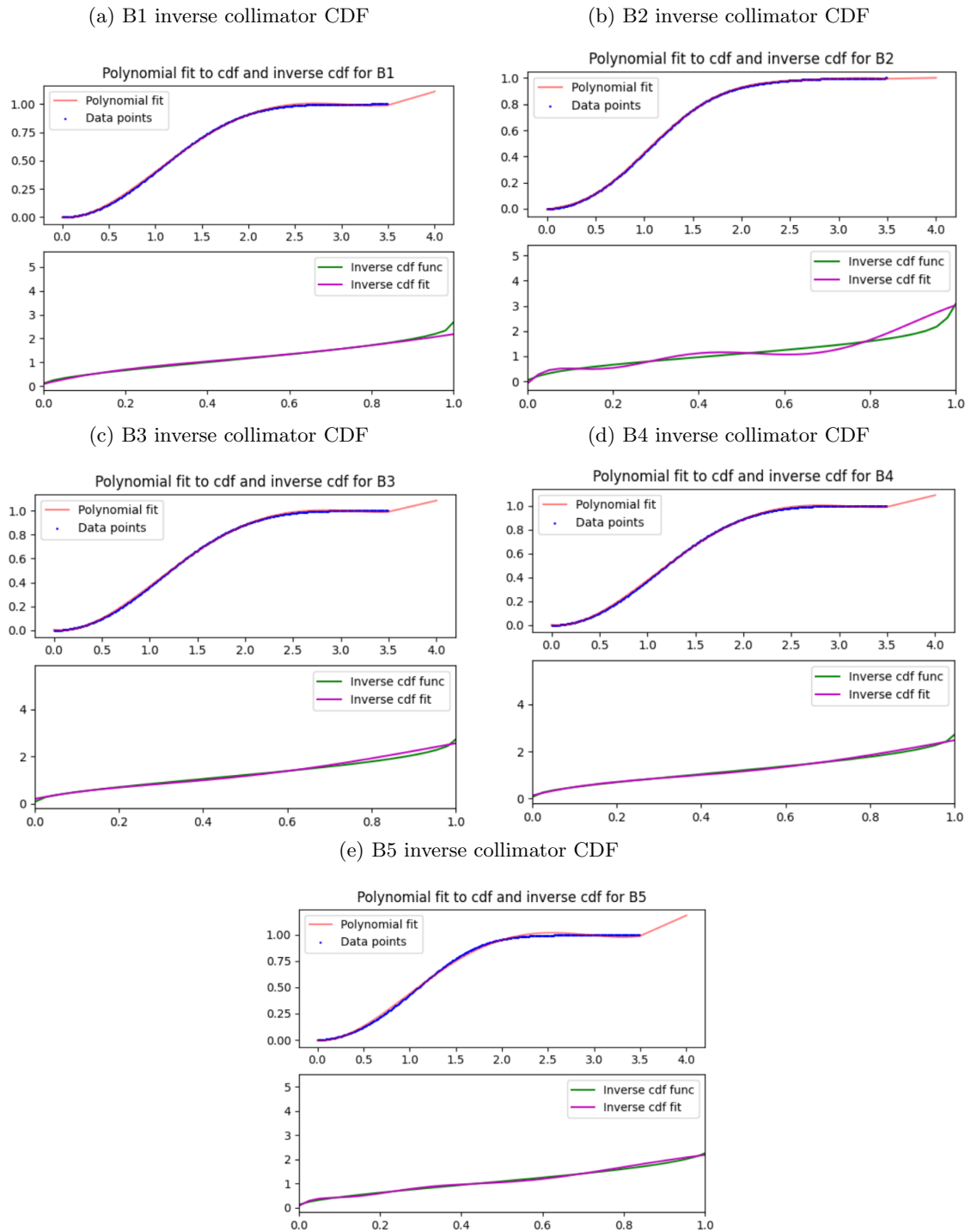


Figure A.4: CDF and inverse CDF fits for the B1 - B5 diffuser PDFs

